ABSTRACT

JESSEE, MATTHEW ANDERSON. Cross-Section Adjustment Techniques for BWR Adaptive Simulation. (Under the direction of Paul J. Turinsky and Hany S. Abdel-Khalik).

Computational capability has been developed to adjust multi-group neutron cross-sections to improve the fidelity of boiling water reactor (BWR) modeling and simulation. The method involves propagating multi-group neutron cross-section uncertainties through BWR computational models to evaluate uncertainties in key core attributes such as core k-effective, nodal power distributions, thermal margins, and in-core detector readings. Uncertainty-based inverse theory methods are then employed to adjust multi-group cross-sections to minimize the disagreement between BWR modeling predictions and measured plant data. For this work, measured plant data were virtually simulated in the form of perturbed 3-D nodal power distributions with discrepancies with predictions of the same order of magnitude as expected from plant data. Using the simulated plant data, multi-group cross-section adjustment reduces the error in core k-effective to less than 0.2% and the RMS error in nodal power to 4% (i.e. – the noise level of the in-core instrumentation). To ensure that the adapted BWR model predictions are robust, Tikhonov regularization is utilized to control the magnitude of the cross-section adjustment. In contrast to few-group cross-section adjustment, which was the focus of previous research on BWR adaptive simulation, multi-group cross-section adjustment allows for future fuel cycle design optimization to include the determination of optimal fresh fuel assembly designs using the adjusted multi-group cross-sections.

The major focus of this work is to efficiently propagate multi-group neutron cross-section uncertainty through BWR lattice physics calculations. Basic neutron cross-section

uncertainties are provided in the form of multi-group cross-section covariance matrices. For energy groups in the resolved resonance energy range, the cross-section uncertainties are computed using an infinitely-dilute approximation of the neutron flux. In order to accurately account for spatial and energy resonance self-shielding effects, the multi-group cross-section covariance matrix has been reformulated to include the uncertainty in resonance correction factors, or self-shielding factors, which are used to calculate the self-shielded multi-group cross-sections used in the lattice physics neutron transport model. This is shown to change the U-238 capture cross-section uncertainty contribution to Beginning-of-Life (BOL) lattice k-infinity by 14% (i.e. - 0.291% relative standard deviation in k-infinity (self-shielded) compared to 0.255% (infinitely-dilute)).

Using the reformulated multi-group cross-section covariance matrix, Efficient Subspace Methods (ESM) are used to propagate multi-group cross-section uncertainty through the lattice physics calculation. ESM algorithms have been developed by H.S. Abdel-Khalik and P.J. Turinsky to calculate low-rank approximations to large, dense sensitivity and covariance matrices used in data adjustment and uncertainty propagation applications. Using ESM, the singular value spectrum of the multi-group cross-section covariance matrix reveals an effective rank of the order of $10^3$. Using this singular value decomposition of the multi-group cross-section covariance matrix reduces the number of lattice physics calculations per lattice from ~$10^7$ to ~$10^3$. In addition, a BOL sensitivity analysis using generalized perturbation theory at the lattice physics level is shown to further reduce the rank by a factor of 5.

Cross-Section Adjustment Techniques for BWR Adaptive Simulation

by
Matthew Anderson Jessee

A dissertation submitted to the Graduate Faculty of
North Carolina State University
in partial fulfillment of the
requirements of the Degree of
Doctor of Philosophy

Nuclear Engineering

Raleigh, North Carolina

2008

APPROVED BY:

| | |
|---|---|
| _____ | _____ |
| Dr. Moody T. Chu | Dr. Dmitriy Y. Anistratov |
| _____ | _____ |
| Dr. Hany S. Abdel-Khalik<br>Co-Chair of Advisory Committee | Dr. Paul J. Turinsky<br>Co-Chair of Advisory Committee |

# DEDICATION

*To Mom, Dad, and Hannah*

# BIOGRAPHY

Matthew Anderson Jessee was born in Kingsport, Tennessee on May 30, 1981 to Michael and Charlene Jessee. He received his elementary and secondary education in Kingsport, graduating from Sullivan South High School in 1999.

Upon graduation from high school, he enrolled in the College of Engineering at the University of Tennessee-Knoxville in the fall of 1999 with the aid of the Herbert S. Walters Scholarship for academic performance in high school. After starting the nuclear engineering curriculum in his sophomore year, he developed a strong interest in reactor physics due to his coursework and summer internships at Tennessee Valley Authority in Chattanooga, Tennessee and at Bettis Laboratories in West Mifflin, Pennsylvania. After his graduation from UT-K with a B. S. in Nuclear Engineering in 2003, he enrolled at North Carolina State University in the Nuclear Engineering Department as a graduate student under the direction of Dr. Paul Turinsky. His Master's project was funded by Global Nuclear Fuels in Wilmington, North Carolina where he worked in the summer and fall of 2004 with Dr. David Kropaczek on boiling water reactor fuel assembly design optimization. After a critical conversation with Dr. Turinsky during his second year at NC State, he decided to work on BWR adaptive simulation for his doctoral research with the financial support of the Naval Nuclear Propulsion Graduate Fellowship Program. After completing his PhD research in May of 2008, Matthew plans to pursue a career in reactor physics research at Oak Ridge National Laboratory.

# ACKNOWLEDGEMENTS

In this short space, I have many people to thank for their technical and personal support. First, I would like to thank Dr. Paul Turinsky and Dr. Hany Abdel-Khalik for being my advisors. To Dr. Turinsky, your educational and technical guidance for the last five years has been invaluable. To Dr. Abdel-Khalik, it has been a pleasure to work with you and to continue your Ph.D research.

I would like to thank the Naval Nuclear Propulsion Fellowship Program for funding my research and providing me with invaluable work experience and the opportunities to present my research at national conferences.

I would also like to thank my mentors, Dr. Carl Yehnert of Bettis Laboratories and Dr. David J. Kropaczek of Studsvik Scandpower, for their significant role in my professional and educational development. To my friends at NC State—Ross, Matt, Loren, Will, Jon Clark, and all other members of Dr. Turinsky's Think Tank—thank you for your help and encouragement.

Last but not least, this project could not have been completed without the guiding hand of my Lord Jesus Christ who has continuously sustained me throughout this stage of my life. I've dedicated this dissertation to my wife Hannah for her love and unwavering support, and to Mom and Dad for their continuous prayers and for always believing in me.

TABLE OF CONTENTS

# LIST OF TABLES

# LIST OF FIGURES

# NOMENCLATURE

| | |
|---|---|
| ACS | Adaptive Core Simulation |
| APRM | Average Power Range Monitor |
| BOC | Beginning-of-Cycle |
| BOL | Beginning-of-Life |
| BP | Burnable Poison |
| BWR | Boiling Water Reactor |
| CRP | Control Rod Program |
| EOC | End-of-Cycle |
| EOL | End-of-Life |
| ESM | Efficient Subspace Methods |
| EVD | Eigenvalue Decomposition |
| GPT | Generalized Perturbation Theory |
| GWD/MTU | Gigawatt-day per metric-tonne-U |
| LOCA | Loss-of-Cooling accident |
| LP | Loading Pattern |
| LPRM | Local Power Range Monitor |
| MOL | Middle-of-Life |
| MOC | Middle-of-Cycle |
| RM | Reich-Moore |
| SVD | Singular Value Decomposition |
| TIP | Traversing Incore Probe |

# 1. Introduction

## 1.1. Importance of BWR Modeling and Simulation

High-fidelity computational modeling and simulation plays a critical role in the design, licensing, and operation of a nuclear power plant. For Boiling Water Reactors (BWRs), core simulators aid in determining the fuel assembly loading pattern (LP) and control rod program (CRP) over the planned operating horizon of the plant. Likewise, lattice physics codes are used to determine fuel rod loading and the mechanical design of BWR fuel assemblies. In addition to these design-based models, safety analysis codes simulate accident scenarios, such as Loss-of-Cooling-Accidents (LOCA), to set key design limits as part of the plant licensing procedure. Finally, on-line core simulators monitor reactor operation and provide support for the successful control and protection of the power plant. The fidelity of these four computational models impacts the reactor economy through the introduction of design margins (i.e. – distance to design limits) for the fuel assembly and core design. Large model prediction uncertainties increase design margins, which in turn, increases fuel cycle costs and limits the plant's power rating. On the other hand, decreasing model prediction uncertainties acts to decrease design margins, which beneficially impacts the reactor economy through reducing fuel cycle and/or operating cost or the initial capital investment for a new nuclear power plant.

Understanding the key sources of BWR model prediction uncertainty is important in deciding where additional efforts should be undertaken to reduce these uncertainties. The three major sources of BWR model prediction uncertainty can be classified as input data,

modeling, and computational uncertainty. Input data uncertainties include uncertainties in basic input data (e.g. - nuclear data) and uncertainties in semi-empirical model parameters (e.g. – drift flux parameters in two-phase flow models). For both basic input data and model parameters, uncertainties are typically due to experimental measurement inaccuracies. In addition to input data uncertainties, modeling uncertainties exist due to either limiting computing resources to model the problem at the fundamental level, or the lack of knowledge of certain physical phenomena (e.g. – semi-empirical modeling). For example, 3-D few-group nodal diffusion methods are used in design-based core simulators as compared to a detailed 3-D multi-group transport model. Finally, computational uncertainties arise from the use of numerical methods to solve the governing system of equations of the computational model. These uncertainties include the effects from floating-point arithmetic error, truncation error, and residual errors associated with matrix-iterative methods employed by BWR computational models.

## 1.2. Motivation for Research

In the effort to quantify BWR model prediction uncertainty due to input data uncertainty, Abdel-Khalik and Turinsky show in [1] that uncertainties in neutron cross-sections (i.e. – nuclear data characterizing the probabilities of interaction between a neutron and the nucleus of an atom) significantly contribute to model prediction uncertainties for a BWR core loaded with low-enriched uranium fuel. Furthermore, they propose that BWR model prediction uncertainty can be reduced by using collected BWR plant data, referred to as core observables, to adjust neutron cross-sections based on their prior uncertainties. Using

the adjusted neutron cross-sections in subsequent simulation improves the prediction of core attributes (i.e. – computed metrics such as thermal limits that are not directly measured, but inferred from the values of the core observables). Increasing the fidelity in core attributes predictions is used to a) change the current operating strategy to increase fuel utilization, operating flexibility, or plant power rating, b) increase design freedom for future fuel cycle strategies, c) enhance future BWR plant design, and d) indicate where future experimental efforts should be focused to decrease core attributes uncertainties. This concept of Adaptive Core Simulation (ACS) is the continued focus of this work.

ACS is classified as a discrete inverse problem commonly referred to as a parameter estimation problem or data adjustment problem. These types of problems are closely related to the field of sensitivity and uncertainty analysis. Before the objectives of this work are presented, a summary of previous work on ACS is given. Following the outline of research objectives, previous applications of data adjustment in reactor physics are reviewed along with relevant inverse theory methods and methods of sensitivity and uncertainty analysis. First, an outline of BWR reactor physics design calculations is provided to facilitate the discussion of previous work.

## 1.3. Overview of BWR Design Calculations

The flow diagram in Figure 1-1 shows the sequence of calculations for BWR reactor design. In this diagram, basic neutron cross-section data is provided in Evaluated Nuclear Data Files (ENDF) [3]-[4] in the form of point-wise (i.e. - continuous energy) cross-sections and resonance parameters used to characterize the sharp energy variation of the cross-section

in the resolved resonance energy range and unresolved resonance energy range. This data is processed by a cross-section preparation code (e.g. – AMPX [5] or NJOY [6]) into multi-group cross-section libraries suitable for lattice physics calculations. The energy detail of the multi-group cross-section library depends on the resonance treatment of the lattice physics code, but is typically ~$10^2$ energy groups. The lattice physics code uses the multi-group cross-section library to model the time-dependent neutron transport over a 2-D radial slice of a BWR fuel assembly (i.e. - lattice). In the lattice physics calculation, self-shielded multi-group cross-sections are generated for each fuel pin in the fuel assembly based on the fuel pin geometry, the moderator density, and number densities of key resonance-absorbing isotopes. Using the self-shielded multi-group cross-sections, the 2-D multi-group neutron flux distribution is calculated over the fuel lattice. The neutron flux distribution is then used to calculate fission and absorption rates in each fuel pin which are in turn used in a fuel pin depletion model. This series of calculations is repeated over a series of time steps (i.e. - burnup steps) to model the time-dependent neutron transport and nuclide transmutation in a BWR lattice. At each time step, the 2-D multi-group neutron flux is used to generate lattice-averaged few-group cross-sections and in-core detector responses for the core simulator. For BWRs, the few-group cross-section library is functionalized in terms of burnup, moderator void fraction history, fuel color, and branch condition.

The core simulator uses the few-group cross-sections to calculate key core attributes and core observables such as Local Power Range Monitor (LPRM) and Traversing Incore Probe (TIP) detector readings. Core simulators contain three to four tightly-coupled physics models: 1) 3-D few-group coarse mesh neutron diffusion model, 2) two-phase flow heat

transfer model, 3) nuclide depletion model, and possibly 4) semi-empirical fuel performance model. At each time step, the 3-D few-group neutron flux distribution is determined over the entire BWR core. This neutron flux distribution is then used to calculate 3-D power distributions, thermal margins, and other core metrics used by core designers and plant operators to describe reactor performance.

Over the last thirty years, the BWR calculation sequence has reached a stage of maturity in sophistication and applicability with advancements in computing power and resources. This sequence of calculations is not expected to change in the near-term future for advanced BWR reactor designs. Although modeling improvements and refinements are continuous, the fidelity of these models should benefit by using adaptive techniques to reduce input data uncertainty.

## 1.4. Previous Work on Adaptive Core Simulation

In the dissertation by Abdel-Khalik [1], the major focus was on the development of Efficient Subspace Methods (ESM); algorithms that determine low-rank approximations to large, dense matrix operators. For BWR ACS, the sensitivity matrix that maps changes in few-group cross-sections to changes in core observables is large (i.e. – $10^6$ by $10^5$) and ill-conditioned. ESM was used to determine an accurate low-rank approximation to the sensitivity matrix using only $10^2$ core simulations. In each simulation, the few-group cross-sections were stochastically perturbed based on a Gaussian probability distribution. The core observable sensitivity profiles along these sampled directions were then used as a basis for few-group cross-section adjustment. In the Master's Thesis of Abdel-Khalik [2], it was

observed that small changes in core observables lead to large changes in the adjusted few-group cross-sections. This ill-posed nature is common among data adjustment problems and generally leads to the use of regularization techniques for robust data adjustment. In [2], Abdel-Khalik introduces the use of Tikhonov regularization [7] to recast the problem into a well-posed one. The Tikhonov regularization parameter is determined experimentally by "trial and error" based on the characteristic L-curve for discrete inverse problems [8]. The few-group cross-section covariance matrix used to constrain the few-group cross-section adjustment was quantified by propagating the multi-group cross-section covariance matrix through the lattice physics calculation.

In the paper by the author, Turinsky, and Abdel-Khalik [9], the few-group cross-section covariance matrix was reevaluated using a refined lattice physics model and a new multi-group cross-section covariance matrix that contained uncertainties to key isotopes such as gadolinium and zirconium that were not provided in the original work. ESM was used to quantify uncertainty in core attributes while minimizing the number of lattice physics calculations and core simulations to $10^3$ and $10^2$, respectively. Few-group cross-section uncertainties were calculated for only one lattice case—that is, a set of burnup dependent few-group cross-sections for a given fuel color and thermal hydraulic condition. The few-group cross-sections uncertainties for other lattice cases were assumed to be fully correlated to the evaluated lattice case.

In the Master's thesis of Briggs [10], few-group cross-sections were adjusted based on assumed measured observables from multiple fuel cycles. This multi-cycle plant adaption used the ESM approach in [1], and accounted for the change in Beginning-of-Cycle (BOC)

burnt-fuel isotope concentrations due to the few-group cross-section adjustment. The sensitivities of core observables with respect to few-group cross-sections from previous fuel cycles were utilized in the plant adaption rather than just a single reload cycle.

## 1.5. Scope of Research

For this work, it is the author's goal to develop the capability to adjust multi-group cross-sections used in the lattice physics calculation for BWR ACS rather than few-group cross-sections used in the core simulator calculation. In the ideal case, the cross-section adjustment is performed at the ENDF level so that a wide range of "experiments" are included (e.g. – criticality experimental benchmarks, and plant data from other reactor types). However, this approach is impractical due to the vast amount of evaluated nuclear data and varying degree of cross-section representations. Multi-group cross-section libraries are generally prepared with the end-application in mind, such as light water reactor multi-group cross-section libraries or fast reactor cross-section libraries. Therefore, multi-group cross-section adjustment still allows for plant data from numerous BWR plants to be utilized to increase the robustness of the adaption.

Multi-group cross-section adjustment also impacts fuel assembly design for future fuel cycles. Using plant data from the current fuel cycle (and possibly from previous fuel cycles and/or other BWRs), the multi-group cross-sections are adjusted and their uncertainty decreased. Using the adjusted multi-group cross-sections and their decreased uncertainties, the fuel rod loading of future fuel assemblies and core LP and CRP are now optimized so that predicted core attributes are known with less uncertainty. In the previous work, only the few-

group cross-sections were adjusted. This restricted the scope of future fuel cycle optimization to the core level rather than the fuel assembly level, or more specifically the lattice level. In other words, the few-group cross-sections adjusted during plant adaption must be reused in future fuel cycle design. Future fuel cycles must then utilize the same fuel assembly designs as used in previous fuel cycles. Although desirable with regards to equilibrium fuel cycle, this restriction in design freedom opposes recent gains in fuel cycle optimization that introduces multiple fresh fuel assembly designs to the reload cycle [11], and potentially offsets the improvement in model fidelity.

Multi-group cross-section adjustment also influences the mechanical design of the fuel assembly (e.g. - fuel pin radius or fuel pin pitch). However, geometric changes in the fuel assembly influence the unit cell calculations in the lattice physics model. As explained later, the unit cell calculation is modified to propagate resonance parameter uncertainties through the lattice physics calculation. For this work, the use of adjusted multi-group cross-sections for future fuel cycle optimization is only applicable for lattices with the same geometry (e.g. - GE14 10 x 10 lattice designs [12]). Extension of the adjusted multi-group cross-sections to mechanical fuel design optimization is discussed in Section 3.2.

The multi-group cross-section adjustment addresses two important issues in the previous work on ACS. First, the few-group cross-section covariances are now quantified for a larger set of fuel colors and thermal hydraulic conditions. This provides a more representative measure of uncertainty for the few-group cross-sections used by the core simulator model. Using the ESM-based approach, the number of lattice physics calculations required is approximately $N*10^3$ where $N$ is the number of lattice cases and the number $10^3$

depends on the number of degrees of freedom associated with the multi-group cross-section covariance matrix. In previous work by the author, Abdel-Khalik, and Turinsky [9], $N$ was assumed equal to 1, but is realistically ~$10^3$ for current core designs. Since $10^6$ lattice physics calculations are computationally intractable, one of the objectives of this work is to determine the number of *active* degrees of freedom (i.e. – multi-group cross-sections with high uncertainty and high sensitivity) that are passed through the lattice physics calculation and core simulation. This is performed using both the ESM approach and sensitivity and uncertainty analysis of the lattice physics calculation using generalized perturbation theory (GPT). This approach reduces the number of lattice physics calculations per lattice case by nearly an order of magnitude. For this work, 10 lattice cases are chosen to provide a better understanding of the few-group cross-section uncertainty for the large range of lattice cases required by the core simulator.

Second, core attributes uncertainties due to important resonance parameters' uncertainties are more accurately quantified. In the previous work on ACS, the multi-group cross-section covariance libraries (44GROUPV5COV and 44GROUPANLCOV [13]) were calculated using the multi-group cross-section preparation code PUFF-III [14].[1] PUFF-III calculates multi-group cross-section covariance matrices for resonance-absorbing isotopes using an infinitely-dilute approximation. Therefore, these covariance matrices apply only to infinitely-dilute multi-group cross-sections, and were not previously treated as such. For this work, resonance parameter uncertainties are provided for key resonance-absorbing isotopes

[1] The original covariance library 44GROUPV5COV did not contain uncertainty data for important elements such as gadolinium and zirconium. The covariance library 44GROUPANLCOV contains approximate covariance evaluations for these elements produced by Argonne National Laboratory (ANL) [15].

(e.g. U-238, Pu-239, Pu-240, Pu-242, Am-241, and Gd isotopes), and their uncertainty contribution is quantified accounting for spatial and energy resonance self-shielding.

Similar to previous work, it is assumed that BWR model prediction uncertainties are dominated by neutron cross-section uncertainties. The uncertainty in key core attributes due to neutron cross-section uncertainty is comparable in magnitude to the observed discrepancies between experimental measurements and plant predictions. Furthermore, the uncertainty quantification calculations using a simplified fuel pin model are comparable in magnitude to the same calculations using the lattice physics model and core simulator. These consistent comparisons validate the claim that neutron cross-section uncertainties dominate the uncertainties due to modeling errors.

In the following section, historical approaches to plant adaption are reviewed along with previous applications of data adjustment in reactor physics. Following the literature review, this thesis is organized into four sections. First, methods of uncertainty analysis based on sensitivity analysis and data adjustment are provided for BWR reactor physics calculations in Chapter 2. In Chapter 3, the generation of the few-group cross-section covariance matrix is discussed. This includes a detailed review of the modified resonance self-shielding model implemented into the lattice physics code TRITON [16] to propagate resonance parameter uncertainties to few-group cross-section uncertainties. In Chapter 4, results of numerical experiments are provided to show the improvement in BWR modeling fidelity based on the proposed adjustment techniques. This is followed by concluding remarks and recommendation for future work in Chapter 5.

## 1.6. Literature Review

The purpose of this work is to increase the fidelity of BWR computational models through the use measured plant data to adjust multi-group cross-sections. Measured BWR plant data is provided in the form of LPRM and TIP detector readings. For a typical GE BWR/6 reactor core, a string of four LPRM detectors is positioned in the center of four fuel assemblies, in the opposite corner of the control rod blade (see Figure 1-2). The four detectors are positioned at different elevations to monitor the axial power profile. The average of the LPRM signals (i.e. – Average Power Range Monitor (APRM) readings) are displayed in the control room panels and a subset of these readings are input to the reactor protection system. LPRMs are recalibrated every 5 to 6 weeks using TIP measurements [17]. TIP measurements are recorded at 100-150 different axial elevations to recalibrate both the LPRM measurements and the on-line core simulator predictions. A BWR typically uses 4 to 5 TIP machines to service one quarter of the detector channels along with a common channel for calibration. The TIP measurement channels coexist along the LPRM detector strings.

Since on-line core simulators employ 3-D coarse-mesh nodal methods, the LPRM detector response is reconstructed from the node-averaged powers or fluxes of the surrounding nodes (typically 4 to 8). One of the original published papers for on-line core simulator adaption was by Crowther in 1981 for the GE 3D Monicore core monitoring system. In [18], Crowther uses a nodal k-infinity correction technique to adjust coarse-mesh coupling coefficients in the FLARE type [19] nodal diffusion calculation. This correction is used to improve the agreement between the on-line core simulator prediction and the measured TIP data within a specified tolerance.

Although current BWR adaption methods are highly proprietary with few published papers, they generally employ similar semi-empirical adjustment techniques verified through operating experience [20]. These approaches differ from the proposed adaptive method of uncertainty-based cross-section adjustment. The proposed approach, formally presented in Section 2.3, requires 1) the sensitivity matrix mapping changes in predicted LPRM readings with respect to changes in multi-group cross-sections, 2) the prior covariance matrices of the multi-group cross-sections and measured LPRM readings[2], and 3) the Generalized Linear Least Squares (GLLS) algorithm for cross-section adjustment. Therefore, the proposed adaptive method is rooted in a rigorous mathematical formulation that has been previously applied in other fields of nuclear engineering.

Data adjustment methods have been used extensively for fast reactor design, criticality safety, and reactor shielding. In the 1970s, Weisbin and Marable et al. ([21]-[22]) developed cross-section adjustment methods for fast reactor design in conjunction with the development of the FORSS code system for sensitivity and uncertainty analysis [23]. In [22], measured integral parameters from fast reactor critical benchmark experiments are used to adjust multi-group cross-section libraries used for liquid metal fast breeder reactor design. Covariance data for both the multi-group cross-sections and the integral experiments are used in the data adjustment. Similar to other work on fast reactor analysis [24]-[27] and recent parametric studies for Generation IV reactor concepts by Aliberti et al [28], only a few number of "observables" or integral parameters (e.g. multiplication factor and breeding ratio)

[2] In a more general formalism of the generalized linear least squares problem, covariance information exists between the input data and output data. For BWR ACS, the prior multi-group cross-section covariance matrix is uncorrelated to the prior measured LPRM covariance matrix.

are used to consistently adjust a large number of multi-group cross-sections. Because of the small number of observables and that the benchmark experimental system has negligible burnup effects, cross-section sensitivities are calculated using first-order eigenvalue perturbation theory (FOEPT) [29] and generalized perturbation theory (GPT) [30]-[34]. For this work, these methods have limited applicability for three reasons. First, the number of observables (~$10^5$ LPRM detector readings) is too large to employ a conventional GPT-based approach. Second, BWR design calculations, as shown in Figure 1-1, are loosely-coupled multi-level nonlinear computational models. Although the theory of adjoint-based sensitivity analysis for nonlinear models is well-developed [35]-[36], it requires considerable effort to "back-fit" existing forward models with linearized first-order adjoint capability. Finally, the computational run-time to determine the first-order adjoint is of the same order as to solve the forward model. In other words, $10^5$ adjoint calculations are just as infeasible as $10^6$ forward calculations in a conventional forward sensitivity study.

GPT-based and FOEPT-based sensitivity methods are reasonably employed to model critical benchmark experiments because computational models can closely emulate the physics of the experiment. For more complicated experiments, approximation techniques have been developed that improve the accuracy of data adjustment for a faster simplified model. These so-called bias factor (BF) and generalized bias operator (BO) methods have been used extensively in the past [37]-[38]. However, these methods generally require a thorough testing of the simplified model that is used to approximate the more sophisticated model and generally require expert judgment to interpret the quality of the adjustment. For this work, it is the authors attempt to use the same computational models in the sensitivity

and uncertainty analysis as in the best-estimate analysis rather than employ BF and BO approaches.

In the last 15 to 20 years, automated differentiation (AD) tools have been developed to calculate sensitivity matrices used for data adjustment. Two main developments have been the OpenAD/F software [39] by Argonne National Laboratory and the Gradient Enhanced Software System (GRESS) [40] used in the TSUNAMI sensitivity and uncertainty analysis code package from Oak Ridge National Laboratory [41] . AD tools generally applied to the same sets of problems as the previous outlined work. That is, for experiments with few input data and many observables or vice versa. Since sensitivity generation is fully automated, AD tools can be applied to highly sophisticated models or sequence of models. For this work, AD tools were not explored because of the major code modification necessary for the AD compiler.

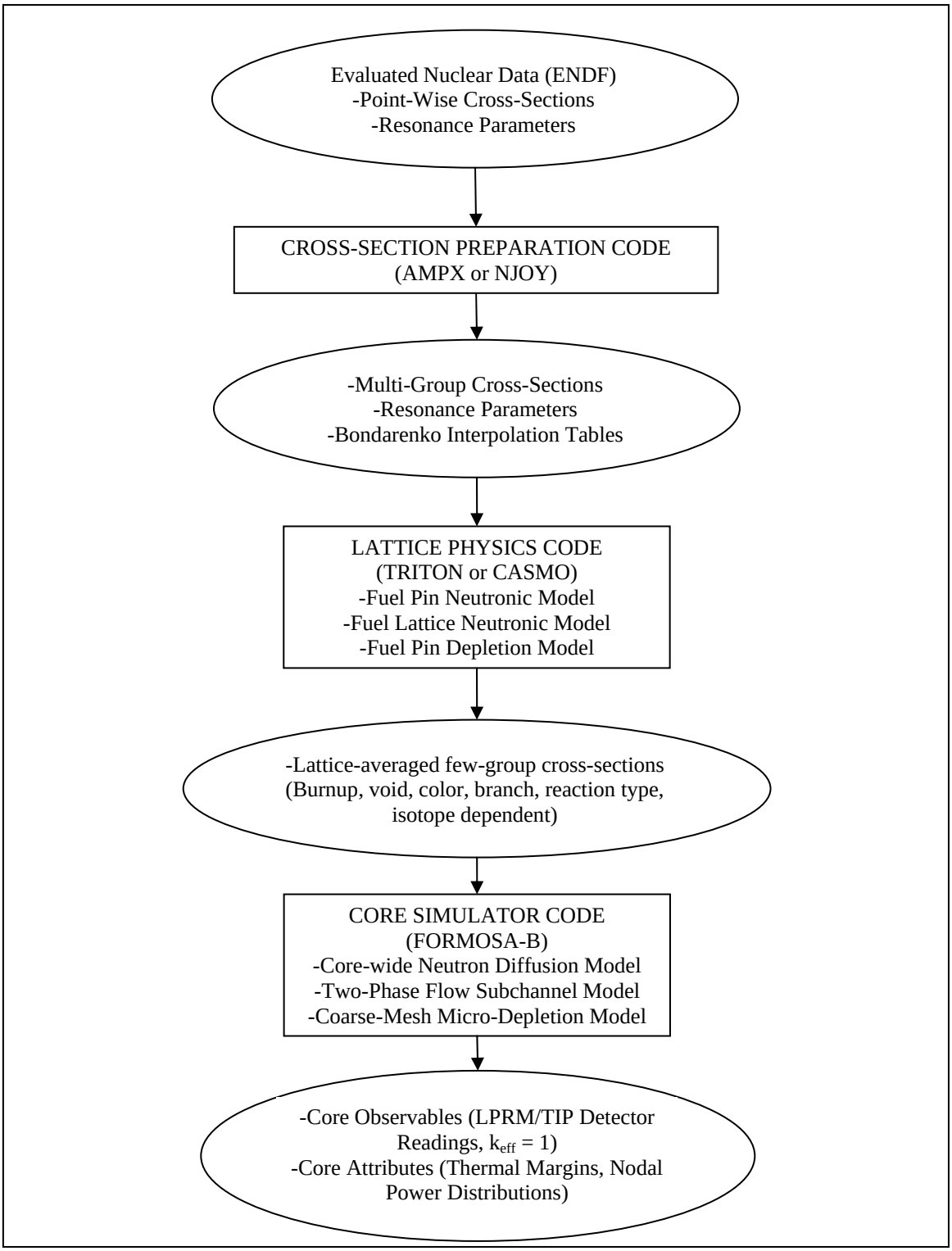


Figure 1-1 Computational sequence for BWR reactor physics design calculations.

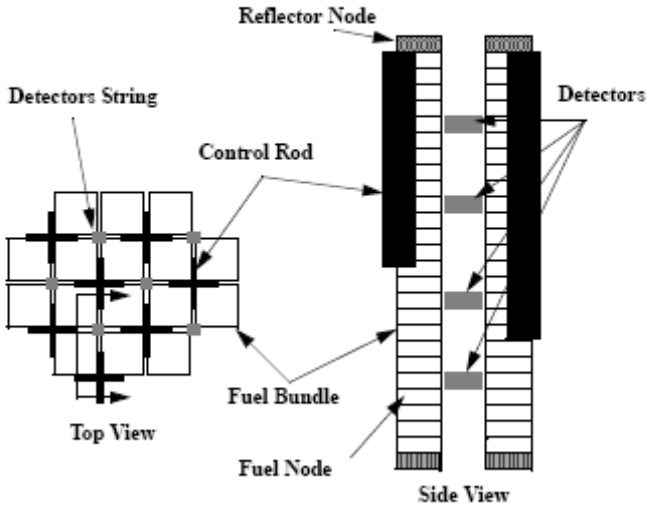


Figure 1-2 Detectors Layout (courtesy of Abdel-Khalik).

# 2. Mathematical Methods for BWR Adaptive Simulation

This chapter outlines the mathematical theory and methods for BWR ACS. The two main methods employed are uncertainty analysis based on first-order sensitivity analysis (i.e. – the "sandwich rule"), and the generalized linear least-squares approach to inverse problems. For this work, these methods are referred to as the uncertainty propagation method and data adjustment method, respectively. A review of the uncertainty propagation method is given in Section 2.2, and the data adjustment method is presented in Section 2.3 based on Tarantola [42]. In each section, the theory of each method is outlined followed by the implementation for BWR ACS.

## 2.1. Mathematical Notation

The following notation is used consistently throughout this work. Any modified or auxiliary notation is provided in subsequent chapters if needed.

| | |
|---|---|
| $\overline{\overline{\mathbf{C}}}$ | Matrix. Subscripts are used for descriptiveness (e.g. - $\overline{\overline{\mathbf{C}}}_{FG}$ - "few-group cross-section covariance matrix"). Superscripts are used for matrix operations (e.g. - $\overline{\overline{\mathbf{C}}}_{FG}^{T}$ or $\overline{\overline{\mathbf{C}}}_{FG}^{-1}$). |
| $\overline{\overline{\mathbf{C}}}_{i,j}$ | the $i$-th row and $j$-th column element of matrix $\overline{\overline{\mathbf{C}}}$. Descriptive subscripts are listed before element indices (e.g. $\overline{\overline{\mathbf{C}}}_{FG,i,j}$). |
| $\overline{\overline{\mathbf{C}}}_{i,*}$ | the $i$-th row vector of matrix $\overline{\overline{\mathbf{C}}}$. |
| $\overline{\overline{\mathbf{C}}}_{*,j}$ | the $j$-th column vector of matrix $\overline{\overline{\mathbf{C}}}$. |

$\bar{x}$ — Vector. Subscripts are used for descriptiveness and superscripts are used for vector operations (e.g. - $\bar{x}_{FG}^{T}$).

$\bar{x}_k$ — the *k*-th element of vector $\bar{x}$. Descriptive subscripts are listed before the element index (e.g. $\bar{x}_{FG,k}$).

$\alpha, b, x_2$ — Scalars. Greek letters are reserved for cross-sections unless noted otherwise.

$\bar{y} = \bar{\boldsymbol{\Theta}}(\bar{x})$ — Nonlinear operator. Subscripts are used for descriptiveness. Parentheses are used to list the independent variables that are "mapped" by the operator (e.g. - $\bar{z} = \bar{\boldsymbol{\Theta}}(\bar{x}, \bar{y})$ - "operator $\bar{\boldsymbol{\Theta}}$ maps $\bar{x}$ and $\bar{y}$ to $\bar{z}$"). Nonlinear operators are frequently referred to simply as $\bar{\boldsymbol{\Theta}}$, where the notation for the domain and range of the operator is suppressed.

$\langle \cdot, \cdot \rangle$ — Inner product. (e.g. - $\langle \bar{x}, \bar{y} \rangle = \bar{x}^T \bar{y}$ and $\langle \bar{x}, \bar{y} \rangle_{\bar{\bar{\mathbf{C}}}} = \bar{x}^T \bar{\bar{\mathbf{C}}} \bar{y}$ for symmetric, positive definite $\bar{\bar{\mathbf{C}}}$).

$\|\cdot\|$ — Norm. Matrix norms are induced vector norms unless noted otherwise. Subscripts are used in traditional manner (e.g. - $\|\cdot\|_p$ - p-norm and $\|\bar{x}\|_{\bar{\bar{\mathbf{A}}}}^2 = \langle \bar{x}, \bar{x} \rangle_{\bar{\bar{\mathbf{A}}}}$ for symmetric, positive definite $\bar{\bar{\mathbf{A}}}$). 2-norm is implied unless noted otherwise.

## 2.2. Uncertainty Propagation

### 2.2.1. Theory

The uncertainty propagation method known as the "sandwich rule" is used to calculate the covariance matrix of a set of observables given a) the covariance matrix of the input parameters, and b) the sensitivity matrix characterizing the change in observables with respect to the change in input parameters [43]. The sandwich rule is derived from the general case of uncertainty propagation concerning a nonlinear computational model with input

parameters uncertainties described by possibly non-Gaussian probability density functions (PDFs). The mathematical expectation of an arbitrary function $g(\bar{x})$ of a vector of continuous input parameters $\bar{x}$ is given as [44]:

$$\begin{aligned} E[g(\bar{x})] &= \int_{-\infty}^{\infty} d\bar{x}_1 \int_{-\infty}^{\infty} d\bar{x}_2 \cdots \int_{-\infty}^{\infty} d\bar{x}_n g(\bar{x}) f(\bar{x}) \\ &= \int_{-\infty}^{\infty} d\bar{x}\, g(\bar{x}) f(\bar{x}) \end{aligned} \tag{2.1}$$

where $E[g(\bar{x})]$ is the expected value of $g(\bar{x})$ and $f(\bar{x})$ is the multivariate PDF that characterizes the input parameter uncertainty. Introducing the computational model as a nonlinear operator:

$$\bar{y} = \bar{\Theta}(\bar{x}) \tag{2.2}$$

where $\bar{x}$ is an $n$-th dimensional vector of input parameters, and $\bar{y}$ is an $m$-th dimensional vector of observables, then the expected mean and expected covariance of the observables is given as:

$$\begin{aligned} E[\bar{y}_i] &= \int_{-\infty}^{\infty} d\bar{x}\, \bar{\Theta}(\bar{x})_i f(\bar{x}) \\ &for\ i = 1, 2, \ldots, m \end{aligned} \tag{2.3}$$

$$\begin{aligned} \overline{\overline{\mathbf{C}}}_{i,j} &= E[(\overline{y}_i - E[\overline{y}_i])(\overline{y}_j - E[\overline{y}_j])] \\ &= \int_{-\infty}^{\infty} d\overline{x}(\overline{\mathbf{\Theta}}(\overline{x})_i - E[\overline{y}_i])(\overline{\mathbf{\Theta}}(\overline{x})_j - E[\overline{y}_j])f(\overline{x}) \\ &\quad for\, i, j = 1, 2, \ldots m \end{aligned} \tag{2.4}$$

In Eq. (2.3) and Eq. (2.4), $\overline{\mathbf{\Theta}}(\overline{x})_i$ denotes the *i*-th observable of the nonlinear operator $\overline{\mathbf{\Theta}}(\overline{x})$. The first-order approximation of the computational model is now introduced as:

$$\overline{y} \cong \overline{\mathbf{\Theta}}(\overline{x}_0) + \overline{\overline{\mathbf{\Theta}}}(\overline{x} - \overline{x}_0) \tag{2.5}$$

where $\overline{x}_0$ stores the mean values of the input parameters and $\overline{\overline{\mathbf{\Theta}}}$ is the model sensitivity matrix, defined as:

$$\overline{\overline{\mathbf{\Theta}}}_{i,j} = \left.\frac{\partial \overline{y}_i}{\partial \overline{x}_j}\right|_{\overline{x}_0} \quad for \begin{matrix} i = 1, 2, \cdots, m \\ j = 1, 2, \cdots, n \end{matrix} \tag{2.6}$$

Substituting the first-order approximation of the computational model into Eq. (2.3), the mean values of the observables $\overline{y}_0$ is derived as:

$$\begin{aligned}\bar{y}_{0,i} &= \int_{-\infty}^{\infty} d\bar{x}[\bar{\boldsymbol{\Theta}}(\bar{x}_0)_i + \sum_{j=1}^{n} \bar{\bar{\boldsymbol{\Theta}}}_{i,j}(\bar{x}_j - \bar{x}_{0,j})]f(\bar{x}) \\ &= \bar{\boldsymbol{\Theta}}(\bar{x}_0)_i \int_{-\infty}^{\infty} d\bar{x}\, f(\bar{x}) + \sum_{j=1}^{n} \bar{\bar{\boldsymbol{\Theta}}}_{i,j} \int_{-\infty}^{\infty} d\bar{x}_j\, (\bar{x}_j - \bar{x}_{0,j})\, f(\bar{x}_j) \\ &= \bar{\boldsymbol{\Theta}}(\bar{x}_0)_i + \sum_{j=1}^{n} \bar{\bar{\boldsymbol{\Theta}}}_{i,j}\, (\bar{x}_{0,j} - \bar{x}_{0,j}) = \bar{\boldsymbol{\Theta}}(\bar{x}_0)_i\end{aligned} \tag{2.7}$$

$$\Rightarrow \bar{y}_0 = \bar{\boldsymbol{\Theta}}(\bar{x}_0) \tag{2.8}$$

Likewise, the observables covariance matrix $\bar{\bar{\mathbf{C}}}_y$ is derived as:

$$\begin{aligned}\bar{\bar{\mathbf{C}}}_{y,i,j} &= \int_{-\infty}^{\infty} d\bar{x}[\sum_{k=1}^{n} \bar{\bar{\boldsymbol{\Theta}}}_{i,k}(\bar{x}_k - \bar{x}_{0,k})][\sum_{l=1}^{n} \bar{\bar{\boldsymbol{\Theta}}}_{j,l}(\bar{x}_l - \bar{x}_{0,l})]f(\bar{x}) \\ &= \sum_{k=1}^{n} \bar{\bar{\boldsymbol{\Theta}}}_{i,k} \sum_{l=1}^{n} \bar{\bar{\boldsymbol{\Theta}}}_{j,l} \int_{-\infty}^{\infty} d\bar{x}_k \int_{-\infty}^{\infty} d\bar{x}_l f(\bar{x}_k, \bar{x}_l)(\bar{x}_k - \bar{x}_{0,k})(\bar{x}_l - \bar{x}_{0,l}) \\ &= \sum_{k=1}^{n} \bar{\bar{\boldsymbol{\Theta}}}_{i,k} \sum_{l=1}^{n} \bar{\bar{\boldsymbol{\Theta}}}_{j,l} \bar{\bar{\mathbf{C}}}_{x,l,k}\end{aligned} \tag{2.9}$$

$$\Rightarrow \bar{\bar{\mathbf{C}}}_y = \bar{\bar{\boldsymbol{\Theta}}} \bar{\bar{\mathbf{C}}}_x \bar{\bar{\boldsymbol{\Theta}}}^T \tag{2.10}$$

where $\bar{\bar{\mathbf{C}}}_x$ is the input parameters covariance matrix. Eq. (2.10) is referred to as the "sandwich rule" and is used to propagate cross-section uncertainties for BWR ACS. Using the derivation above, the following statements can be made regarding model nonlinearity and the observables PDF:

1) If $\bar{\boldsymbol{\Theta}}$ is linear and the input parameters PDF is Gaussian, then the observables PDF is Gaussian and is fully characterized by $\bar{y}_0$ and $\bar{\bar{\mathbf{C}}}_x$ determined by Eq. (2.8) and Eq. (2.10).

2) If $\bar{\boldsymbol{\Theta}}$ is linear and the input parameters PDF is non-Gaussian, then the first and second moments (i.e. mean and covariance) of the observables PDF are determined exactly by Eq. (2.8) and Eq. (2.10). However, $\bar{y}_0$ and $\bar{\bar{\mathbf{C}}}_x$ do not fully characterize the observables PDF due to the nonzero higher order moments of the input parameters PDF.

3) If $\bar{\boldsymbol{\Theta}}$ is nonlinear and the input parameters PDF is Gaussian, then the first and second moments of the observables PDF are approximately determined by Eq. (2.8) and Eq. (2.10). If $\boldsymbol{\Theta}$ has weak nonlinearity effects, then the Gaussian PDF characterized by $\bar{y}_0$ and $\bar{\bar{\mathbf{C}}}_x$ is an accurate approximation of the observables PDF.

4) If $\bar{\boldsymbol{\Theta}}$ is nonlinear and the input parameters PDF is non-Gaussian, then the first and second moments of the observables PDF are approximately determined by Eq. (2.8) and Eq. (2.10). Further calculations are necessary to determine more accurate first and second moments of the observables PDF and possibly important higher order moments.

For BWR ACS, only the mean value of cross-sections and their covariances are provided in ENDF cross-section files. Cross-section uncertainty contains both stochastic errors due to statistical counting uncertainties in cross-section measurements and systematic errors (i.e. operator errors) that are usually harder to estimate [45]. More understanding of the systematic errors is necessary before characterizing the cross-section PDF as Gaussian. As shown in later sections, the lattice physics computational model and core simulator model have very small nonlinearity effects. Therefore, the application of the sandwich rule for BWR ACS accurately determines the first and second moments of the core observables (or core attributes) PDF. The first and second moments can be used to calculate a Gaussian PDF

that closely approximates the exact core observables PDF assuming that the systematic errors in cross-section measurements are small.

### 2.2.2. Implementation

For BWR ACS, the uncertainty propagation method outlined above is used to propagate cross-section covariance data through each stage of the BWR calculation sequence shown in Figure 1-1. Using Eq. (2.10), the following relationships are derived:

$$\overline{\overline{\mathbf{C}}}_{MG} = \overline{\overline{\mathbf{S}}}_{XP} \overline{\overline{\mathbf{C}}}_{ENDF} \overline{\overline{\mathbf{S}}}_{XP}^{T} \tag{2.11}$$

$$\overline{\overline{\mathbf{C}}}_{FG} = \overline{\overline{\mathbf{S}}}_{LP} \overline{\overline{\mathbf{C}}}_{MG} \overline{\overline{\mathbf{S}}}_{LP}^{T} \tag{2.12}$$

$$\overline{\overline{\mathbf{C}}}_{CO} = \overline{\overline{\mathbf{S}}}_{CS} \overline{\overline{\mathbf{C}}}_{FG} \overline{\overline{\mathbf{S}}}_{CS}^{T} \tag{2.13}$$

In Eqs. (2.11)-(2.13), $\overline{\overline{\mathbf{C}}}_{ENDF}$ is the ENDF cross-section covariance matrix, $\overline{\overline{\mathbf{S}}}_{XP}$ is the cross-section preparation code sensitivity matrix, $\overline{\overline{\mathbf{C}}}_{MG}$ is the self-shielded multi-group cross-section covariance matrix, $\overline{\overline{\mathbf{S}}}_{LP}$ is the lattice physics sensitivity matrix, $\overline{\overline{\mathbf{C}}}_{FG}$ is the few-group cross-section covariance matrix, $\overline{\overline{\mathbf{S}}}_{CS}$ is the core simulator sensitivity matrix, and $\overline{\overline{\mathbf{C}}}_{CO}$ is the core observables covariance matrix. The sizes of these matrices are approximately $10^6$ x $10^6$, $10^6$ x $10^7$, $10^7$ x $10^7$, $10^7$ x $10^6$, $10^6$ x $10^6$, $10^6$ x $10^5$, and $10^5$ x $10^5$ respectively. It is evident

that these equations are not used directly because of a) the size of the various matrices, b) the computational burden of each matrix multiplication, and c) the computational burden of evaluating each sensitivity matrix. In addition, conventional forward and adjoint sensitivity methods are not used due to the storage and computational burden of both approaches. For this work, Efficient Subspace Methods are used as developed by Abdel-Khalik in [1].

### 2.2.3. ESM Implementation

Efficient Subspace Methods (ESM) calculate accurate low-rank approximations for sensitivity and covariance matrices using singular value decomposition (SVD). ESM only requires the action of the sensitivity matrix operating on a vector (i.e. – matrix-vector product) and possibly the action of the transpose of the sensitivity matrix operating on a vector (i.e. – transpose matrix-vector product). One possible method to calculate a matrix-vector product is by the forward perturbation approach. That is, given any vector $\bar{q} \in R^n$ and computational model $\bar{\boldsymbol{\Theta}}$, vector $\bar{\bar{\boldsymbol{\Theta}}}\bar{q} \in R^m$ is calculated as:

$$\bar{\bar{\boldsymbol{\Theta}}}\bar{q} \cong \frac{\bar{\boldsymbol{\Theta}}(\bar{x}_0 + \varepsilon\bar{q}) - \bar{\boldsymbol{\Theta}}(\bar{x}_0)}{\varepsilon} \tag{2.14}$$

where the sensitivities are evaluated at $\bar{x}_0$. The transpose matrix-vector product for the sensitivity matrix is referred to as $\bar{\bar{\boldsymbol{\Theta}}}^T(\bar{p})$ for some input vector $\bar{p} \in R^m$ and is commonly calculated using first-order adjoint methods [36].

Throughout this work, the following definitions for singular value decomposition are used from [46][1]:

$$\overline{\overline{\mathbf{\Theta}}}_{mxn},\ rank(\overline{\overline{\mathbf{\Theta}}}) = r,\ r < n < m \tag{2.15}$$

SVD: $$\overline{\overline{\mathbf{\Theta}}}_{mxn} = \overline{\overline{\mathbf{U}}}_{mxm}\overline{\overline{\mathbf{\Sigma}}}_{m\,xn}\overline{\overline{\mathbf{V}}}^{T}_{nxn} \tag{2.16}$$

Thin SVD: $$\overline{\overline{\mathbf{\Theta}}}_{mxn} = \overline{\overline{\mathbf{U}}}_{mxn}\overline{\overline{\mathbf{\Sigma}}}_{n\,xn}\overline{\overline{\mathbf{V}}}^{T}_{nxn} \tag{2.17}$$

Compact SVD: $$\overline{\overline{\mathbf{\Theta}}}_{mxn} = \overline{\overline{\mathbf{U}}}_{mxr}\overline{\overline{\mathbf{\Sigma}}}_{r\,xr}\overline{\overline{\mathbf{V}}}^{T}_{rxn} \tag{2.18}$$

Truncated-SVD: $$\overline{\overline{\mathbf{\Theta}}}_{t} = \overline{\overline{\mathbf{U}}}_{mxt}\overline{\overline{\mathbf{\Sigma}}}_{t\,xt}\overline{\overline{\mathbf{V}}}^{T}_{txn} = \overline{\overline{\mathbf{U}}}_{t}\overline{\overline{\mathbf{\Sigma}}}_{t}\overline{\overline{\mathbf{V}}}^{T}_{t} \tag{2.19}$$

where the truncated-SVD $\overline{\overline{\mathbf{\Theta}}}_{t}$ is rank-*t*, where $t < r$, and is the minimizer of

$$\overline{\overline{\mathbf{\Theta}}}_{t} = \min_{\overline{\overline{\mathbf{A}}}} \left\| \overline{\overline{\mathbf{\Theta}}} - \overline{\overline{\mathbf{A}}} \right\|_2,\ for\ any\ \overline{\overline{\mathbf{A}}}\ with\ rank(\overline{\overline{\mathbf{A}}}) = t \tag{2.20}$$

The 2-norm error in $\overline{\overline{\mathbf{\Theta}}}_{t}$ is equal to the $t+1$-singular value of $\overline{\overline{\mathbf{\Theta}}}$ (i.e. - $\overline{\overline{\mathbf{\Theta}}}_{t+1,t+1}$). ESM determines the truncated-SVD of $\overline{\overline{\mathbf{\Theta}}}$ provided that the matrix-vector product and the

[1] Rank can be defined here as exact mathematical rank or numerical rank. For BWR ACS, only a few singular values and singular vectors of the sensitivity and covariance matrices are needed since the singular values relative to the largest singular value decrease in magnitude rapidly ([1] and [9]). Therefore, the use of rank in this work implies the number of singular values and singular vectors used in the calculation unless noted otherwise.

transpose matrix-vector product are available.[2] Since the transpose matrix-vector product is unavailable for both the lattices physics model and the core simulator model, the ESM approach utilizes the truncated-SVD of the self-shielded multi-group cross-section covariance matrix to minimize storage and calculation burden. Introducing the truncated-SVD of $\overline{\overline{\mathbf{C}}}_{MG}$ with *t*-singular values as:

$$\overline{\overline{\mathbf{C}}}_{MG} \cong \overline{\overline{\mathbf{U}}}_{MG,t}\,\overline{\overline{\boldsymbol{\Sigma}}}_{MG,t}\,\overline{\overline{\mathbf{U}}}^{T}_{MG,t} \tag{2.21}$$

then the few-group cross-section covariance matrix $\overline{\overline{\mathbf{C}}}_{FG}$ is given as (cf. - Eq. (2.12)):

$$\begin{aligned}\overline{\overline{\mathbf{C}}}_{FG} &= \overline{\overline{\mathbf{S}}}_{LP}\,\overline{\overline{\mathbf{C}}}_{MG}\,\overline{\overline{\mathbf{S}}}^{T}_{LP} \\ &\cong \overline{\overline{\mathbf{S}}}_{LP}\,\overline{\overline{\mathbf{U}}}_{MG,t}\,\overline{\overline{\boldsymbol{\Sigma}}}_{MG,t}\,\overline{\overline{\mathbf{U}}}^{T}_{MG,t}\,\overline{\overline{\mathbf{S}}}^{T}_{LP}\end{aligned} \tag{2.22}$$

$$\begin{aligned}\overline{\overline{\mathbf{C}}}_{FG} &= (\overline{\overline{\mathbf{S}}}_{LP}\,\overline{\overline{\mathbf{U}}}_{MG,t}\,\overline{\overline{\boldsymbol{\Sigma}}}^{1/2}_{MG,t})(\overline{\overline{\mathbf{S}}}_{LP}\,\overline{\overline{\mathbf{U}}}_{MG,t}\,\overline{\overline{\boldsymbol{\Sigma}}}^{1/2}_{MG,t})^{T} \\ &= \overline{\overline{\mathbf{R}}}_{LP,t}\,\overline{\overline{\mathbf{R}}}^{T}_{LP,t}\end{aligned} \tag{2.23}$$

Using this approach, $\overline{\overline{\mathbf{C}}}_{FG}$ is calculated with *t* matrix-vector products of $\overline{\overline{\mathbf{S}}}_{LP}$ (i.e. - $\overline{\overline{\mathbf{S}}}_{LP}(\overline{\overline{\mathbf{U}}}_{MG,t}\,\overline{\overline{\boldsymbol{\Sigma}}}^{1/2}_{MG,t})$). The matrix $\overline{\overline{\mathbf{R}}}_{LP,t}$ denotes the matrix storage of the *t* matrix-vector

[2] In the original development of ESM in [1], Abdel-Khalik distinguishes the exact transpose matrix-vector product from an auxiliary transpose matrix-vector product that spans the subspace of the right-singular vectors with nonzero singular values (see . The former can be formally derived by the first-order adjoint equations for each of the *m* observables while the latter requires expert judgment as to where the dominant subspace "projection" occurs in each computational model. The reader is referred to Section A.V (pp. 179-194) of [1] for further detail on the transpose vector product approximation.

products. Since there are ~$10^6$ few-group cross-sections, the matrix-matrix multiplication $\overline{\overline{\mathbf{R}}}_{LP,t}\overline{\overline{\mathbf{R}}}^{T}_{LP,t}$ is impractical. However, important elements of $\overline{\overline{\mathbf{C}}}_{FG}$ (e.g. – diagonal elements), are calculated by:

$$\overline{\overline{\mathbf{C}}}_{FG_{i,j}} = \sum_{k=1}^{t} \overline{\overline{\mathbf{R}}}_{LP,t_{i,k}} \overline{\overline{\mathbf{R}}}_{LP,t_{j,k}} \tag{2.24}$$

The matrix $\overline{\overline{\mathbf{R}}}_{LP,t}$ is directly used to calculate the core observables covariance matrix. Given the truncated-SVD of $\overline{\overline{\mathbf{R}}}_{LP,t}$ with rank-$t_2$, which is less than rank-$t$:

$$\overline{\overline{\mathbf{R}}}_{LP,t} \cong \overline{\overline{\mathbf{U}}}_{LP,t_2} \overline{\overline{\mathbf{\Sigma}}}_{LP,t_2} \overline{\overline{\mathbf{\Psi}}}^{T}_{LP,t_2} \tag{2.25}$$

then $\overline{\overline{\mathbf{C}}}_{CO}$ is calculated as (cf. - Eq. (2.13)):

$$\begin{aligned} \overline{\overline{\mathbf{C}}}_{CO} &= \overline{\overline{\mathbf{S}}}_{CS} \overline{\overline{\mathbf{C}}}_{FG} \overline{\overline{\mathbf{S}}}^{T}_{CS} \\ &= \overline{\overline{\mathbf{S}}}_{CS} \overline{\overline{\mathbf{R}}}_{LP,t} \overline{\overline{\mathbf{R}}}^{T}_{LP,t} \overline{\overline{\mathbf{S}}}^{T}_{CS} \end{aligned} \tag{2.26}$$

$$\begin{aligned} \overline{\overline{\mathbf{C}}}_{CO} &= (\overline{\overline{\mathbf{S}}}_{CS} \overline{\overline{\mathbf{U}}}_{LP,t_2} \overline{\overline{\mathbf{\Sigma}}}_{LP,t_2}) \overline{\overline{\mathbf{\Psi}}}^{T}_{LP,t_2} \overline{\overline{\mathbf{\Psi}}}_{LP,t_2} (\overline{\overline{\mathbf{S}}}_{CS} \overline{\overline{\mathbf{U}}}_{LP,t_2} \overline{\overline{\mathbf{\Sigma}}}_{LP,t_2})^{T} \\ &= \overline{\overline{\mathbf{R}}}_{CS,t_2} \overline{\overline{\mathbf{R}}}^{T}_{CS,t_2} \end{aligned} \tag{2.27}$$

In Eq. (2.27), $\overline{\overline{\mathbf{C}}}_{CO}$ is calculated with $t_2$ matrix-vector products of $\overline{\overline{\mathbf{S}}}_{CS}$. Since the right singular vectors $\overline{\overline{\mathbf{\Psi}}}_{LP,t_2}$ are not needed in Eq. (2.27) (i.e. - $\overline{\overline{\mathbf{\Psi}}}^{T}_{LP,t_2}\overline{\overline{\mathbf{\Psi}}}_{LP,t_2} = \overline{\mathbf{I}}$), matrix $\overline{\overline{\mathbf{R}}}_{CS,t_2}$ stores only $\overline{\overline{\mathbf{S}}}_{CS}(\overline{\overline{\mathbf{U}}}_{LP,t_2}\overline{\overline{\mathbf{\Sigma}}}_{LP,t_2})$. However, $\overline{\overline{\mathbf{\Psi}}}_{LP,t_2}$ is needed for data adjustment and is explained in Section 2.3.2. Important elements of $\overline{\overline{\mathbf{C}}}_{CO}$ are calculated by:

$$\overline{\overline{\mathbf{C}}}_{CO_{i,j}} = \sum_{k=1}^{t_2} \overline{\overline{\mathbf{R}}}_{CS,t_2\,i,k}\,\overline{\overline{\mathbf{R}}}_{CS,t_2\,j,k} \tag{2.28}$$

In summary, the ESM approach of uncertainty propagation for BWR ACS requires 1) the calculation of the truncated-SVD of $\overline{\overline{\mathbf{C}}}_{MG}$, 2) the selection of rank-*t*, 3) *t*-matrix vector products of $\overline{\overline{\mathbf{S}}}_{LP}$, 4) the truncated-SVD of $\overline{\overline{\mathbf{R}}}_{LP,t}$, 5) the selection of rank-$t_2$, and 6) $t_2$ matrix-vector products of $\overline{\overline{\mathbf{S}}}_{CS}$. These steps are outlined in more detail in Chapter 3.

## 2.3. Data Adjustment

### 2.3.1. Theory

The data adjustment method for BWR ACS follows the generalized linear least-square approach given in [42]. The following information about the input parameters and observables is given a priori:

$\overline{x}_0$ prior input parameters

| | |
|---|---|
| $\overline{\overline{\mathbf{C}}}_x$ | prior input parameters covariance matrix |
| $\overline{y}_m$ | prior observables (i.e. - measured observables) |
| $\overline{\overline{\mathbf{C}}}_{y_m}$ | prior observables covariance matrix (i.e. - the uncertainty in the measured observables). |
| $\overline{y} = \overline{\mathbf{\Theta}}(\overline{x})$ | the computational model |

The goal is to adjust $\overline{x}_0$ to a new value, denoted $\overline{\tilde{x}}$, that minimizes[3]:

$$\overline{\tilde{x}} = \min_{\overline{x}} \{ \left\| \overline{y}_m - \overline{\mathbf{\Theta}}(\overline{x}) \right\|^2_{\overline{\overline{\mathbf{C}}}^{-1}_{y_m}} + \left\| \overline{x} - \overline{x}_0 \right\|^2_{\overline{\overline{\mathbf{C}}}^{-1}_{x}} \} \tag{2.29}$$

Using the first-order approximation to the nonlinear computational model $\overline{\mathbf{\Theta}}$:

$$\overline{y} \cong \overline{y}_0 + \overline{\overline{\mathbf{\Theta}}}(\overline{x} - \overline{x}_0) \tag{2.30}$$

then Eq. (2.29) becomes:

$$\overline{\tilde{x}} = \min_{\overline{x}} \{ \left\| \overline{y}_m - \overline{y}_0 - \overline{\overline{\mathbf{\Theta}}}(\overline{x} - \overline{x}_0) \right\|^2_{\overline{\overline{\mathbf{C}}}^{-1}_{y_m}} + \left\| \overline{x} - \overline{x}_0 \right\|^2_{\overline{\overline{\mathbf{C}}}^{-1}_{x}} \} \tag{2.31}$$

[3] In this formulation, the prior input parameters uncertainty is uncorrelated to the prior observables uncertainty. This a valid assumption for BWR ACS, because neutron cross-sections are measured independently from measured plant data. Some formulations consider nonzero correlations between the prior input parameters uncertainty and prior observables uncertainty. In addition, other formulations consider only the prior observables uncertainty and the second term in Eq. (2.31) is not considered.

The solution to Eq. (2.31) is given in [42] as:

$$\begin{aligned}
\bar{\tilde{x}} &= \bar{x}_0 + (\bar{\bar{\mathbf{\Theta}}}^T \bar{\bar{\mathbf{C}}}_{y_m}^{-1} \bar{\bar{\mathbf{\Theta}}} + \bar{\bar{\mathbf{C}}}_x^{-1})^{-1} \bar{\bar{\mathbf{\Theta}}}^T \bar{\bar{\mathbf{C}}}_{y_m}^{-1} (\bar{y}_m - \bar{y}_0) \\
\bar{\tilde{y}} &= \mathbf{\Theta}(\bar{\tilde{x}}) \cong \bar{y}_0 + \bar{\bar{\mathbf{\Theta}}}(\bar{\tilde{x}} - \bar{x}_0) \\
\bar{\bar{\mathbf{C}}}_{\tilde{x}} &= (\bar{\bar{\mathbf{\Theta}}}^T \bar{\bar{\mathbf{C}}}_{y_m}^{-1} \bar{\bar{\mathbf{\Theta}}} + \bar{\bar{\mathbf{C}}}_x^{-1})^{-1} \\
\bar{\bar{\mathbf{C}}}_{\tilde{y}} &= \bar{\bar{\mathbf{\Theta}}} \bar{\bar{\mathbf{C}}}_{\tilde{x}} \bar{\bar{\mathbf{\Theta}}}^T
\end{aligned} \tag{2.32}$$

where $\bar{\tilde{x}}$ is the posterior input parameters, $\bar{\tilde{y}}$ is the posterior observables, $\bar{\bar{\mathbf{C}}}_{\tilde{x}}$ is the posterior input parameters covariance matrix, and $\bar{\bar{\mathbf{C}}}_{\tilde{y}}$ is the posterior observables covariance matrix. The posterior values in Eq. (2.32) are determined by the normal equation solution of the generalized linear least-squares equation.

## 2.3.2. ESM Implementation

For BWR ACS, the goal is to adjust the set of self-shielded multi-group cross-sections to minimize the disagreement between measured core observables and predicted core observables. The following information is given a priori:

| | |
|---|---|
| $\bar{x}_{MG_0}$ | prior self-shielded multi-group cross-sections |
| $\bar{x}_{FG_0}$ | prior lattice-averaged few-group cross-sections |
| $\bar{\bar{\mathbf{C}}}_{MG}$ | prior self-shielded multi-group cross-sections covariance matrix |
| $\bar{y}_{CO_m}$ | prior core observables (i.e. - measured observables) |

| | |
|---|---|
| $\overline{\overline{\mathbf{C}}}_{CO_m}$ | prior core observables covariance matrix (i.e. - the uncertainty in the measurements of core observables). |
| $\overline{\boldsymbol{\Theta}}_{LP}$ | lattice physics computational model |
| $\overline{\boldsymbol{\Theta}}_{CS}$ | core simulator computational model |
| $\overline{y}_{CO_0}$ | prior core observables as predicted by computational model |
| $n$ | dimension of $\overline{x}_{MG_0}$ ($\sim 10^7$) |
| $m$ | dimension of $\overline{y}_{CO_m}$ ($\sim 10^5$) |

The first-order approximation to the computational model is given as:

$$\overline{y}_{CO} = \overline{y}_{CO_0} + \overline{\overline{\mathbf{S}}}_{CS}\overline{\overline{\mathbf{S}}}_{LP}(\overline{x}_{MG} - \overline{x}_{MG_0}) \tag{2.33}$$

where $\overline{\overline{\mathbf{S}}}_{LP}$ and $\overline{\overline{\mathbf{S}}}_{CS}$ are the sensitivity matrices of the lattice physics model and core simulator model respectively. The data adjustment problem is now given as (cf. – Eq. (2.31)):

$$\overline{\tilde{x}}_{MG} = \min_{\overline{x}_{MG}}\{\left\| \overline{y}_{CO_m} - \overline{y}_{CO_0} - \overline{\overline{\mathbf{S}}}_{CS}\overline{\overline{\mathbf{S}}}_{LP}(\overline{x}_{MG} - \overline{x}_{MG_0})\right\|^2_{\overline{\overline{\mathbf{C}}}^{-1}_{CO_m}} + \left\| \overline{x}_{MG} - \overline{x}_{MG_0}\right\|^2_{\overline{\overline{\mathbf{C}}}^{-1}_{MG}}\} \tag{2.34}$$

where $\overline{\tilde{x}}_{MG}$ is the posterior self-shielded multi-group cross-sections. Eq. (2.34) represents an ill-posed data adjustment problem for the following two reasons. First, the prior self-shielded multi-group cross-sections covariance matrix $\overline{\overline{\mathbf{C}}}_{MG}$ is replaced by its truncated-SVD (i.e. - $\overline{\overline{\mathbf{U}}}_{MG,t}\overline{\overline{\boldsymbol{\Sigma}}}_{MG,t}\overline{\overline{\mathbf{U}}}^{T}_{MG,t}$), so $\overline{\overline{\mathbf{C}}}^{-1}_{MG}$ does not exist. The second term in Eq. (2.34) is now redefined as

$(\bar{x}_{MG} - \bar{x}_{MG_0})^T \bar{\bar{\mathbf{C}}}^{\dagger}_{MG} (\bar{x}_{MG} - \bar{x}_{MG_0})$, where the Moore-Penrose pseudoinverse matrix of $\bar{\bar{\mathbf{C}}}_{MG}$ has been introduced (i.e. - $\bar{\bar{\mathbf{C}}}^{\dagger}_{MG} \bar{\bar{\mathbf{U}}}_{MG,t} \bar{\bar{\mathbf{\Sigma}}}^{-1}_{MG,t} \bar{\bar{\mathbf{U}}}^{T}_{MG,t}$). Introducing the pseudoinverse of $\bar{\bar{\mathbf{C}}}_{MG}$ leads to an infinite number of possible solutions for the data adjustment problem. To ensure that the least-squares solution is unique (i.e. – well-posed), the self-shielded multi-group cross-section adjustment is constrained to the subspace spanned by the *t* singular vectors of $\bar{\bar{\mathbf{U}}}_{MG,t}$. Second, $\bar{\bar{\mathbf{S}}}_{LP}$ and $\bar{\bar{\mathbf{S}}}_{CS}$ are ill-conditioned (i.e. – small singular values) and $\bar{y}_{CO_m}$ contains inherent noise that is several orders of magnitude larger than the small singular values associated with the ill-conditioned sensitivity matrices. This can lead to unphysical cross-section adjustments along singular vectors corresponding to the small singular values of the sensitivity matrices. Regularization techniques need to be employed to recast the ill-conditioned, ill-posed data adjustment problem into a well-posed one..

For BWR ACS, the following modifications are made to Eq. (2.34) to produce a well-posed data adjustment problem:

$$\bar{\tilde{x}}_{MG} = \min_{\bar{x}_{MG}} \{ [\bar{y}_{CO_m} - \bar{y}_{CO_0} - \bar{\bar{\mathbf{S}}}_{CS} \bar{\bar{\mathbf{S}}}_{LP} (\bar{x}_{MG} - \bar{x}_{MG_0})]^T \bar{\bar{\mathbf{C}}}^{\dagger}_{CO_m} [\bar{y}_{CO_m} - \bar{y}_{CO_0} - \bar{\bar{\mathbf{S}}}_{CS} \bar{\bar{\mathbf{S}}}_{LP} (\bar{x}_{MG} - \bar{x}_{MG_0})] + \alpha^2 (\bar{x}_{MG} - \bar{x}_{MG_0})^T \bar{\bar{\mathbf{C}}}^{\dagger}_{MG} (\bar{x}_{MG} - \bar{x}_{MG_0}) \} \quad (2.35)$$
$$subject\ to\ \bar{x}_{MG} - \bar{x}_{MG_0} \in R(\bar{\bar{\mathbf{U}}}_{MG,t})$$

where $R(\bar{\bar{\mathbf{U}}}_{MG,t})$ represents the range of matrix $\bar{\bar{\mathbf{U}}}_{MG,t}$ and have introduced $\alpha^2$ the Tikhonov regularization parameter [7]. The first term on the right-hand side of Eq. (2.35) is referred to

as the misfit chi-square $\chi_m^2$, and the second term is referred to as the regularization chi-square $\chi_r^2$. The *n* by *n* matrix $\overline{\overline{\mathbf{C}}}_{CO_m}^{-1}$ is replaced with its pseudoinverse $\overline{\overline{\mathbf{C}}}_{CO_m}^{\dagger}$ by introducing the following compact SVD of the prior core observables covariance matrix:[4]

$$\begin{aligned}\overline{\overline{\mathbf{C}}}_{CO_m} &= \overline{\overline{\mathbf{U}}}_{CO_m}\,\overline{\overline{\mathbf{\Sigma}}}_{CO_m}\,\overline{\overline{\mathbf{U}}}_{CO_m}^{T} \\ \overline{\overline{\mathbf{C}}}_{CO_m}^{\dagger} &= \overline{\overline{\mathbf{U}}}_{CO_m}\,\overline{\overline{\mathbf{\Sigma}}}_{CO_m}^{-1}\,\overline{\overline{\mathbf{U}}}_{CO_m}^{T}\end{aligned} \tag{2.36}$$

Because the self-shielded multi-group cross-section adjustment $\overline{x}_{MG} - \overline{x}_{MG_0}$ is constrained to $R(\overline{\overline{\mathbf{U}}}_{MG,t})$, the following change in variables is introduced:

$$\overline{z}_{MG} = \overline{\overline{\mathbf{\Sigma}}}_{MG,t}^{-1/2}\,\overline{\overline{\mathbf{U}}}_{MG,t}^{T}(\overline{x}_{MG} - \overline{x}_{MG_0}) \tag{2.37}$$

$$\overline{x}_{MG} = \overline{x}_{MG_0} + \overline{\overline{\mathbf{U}}}_{MG,t}\,\overline{\overline{\mathbf{\Sigma}}}_{MG,t}^{1/2}\,\overline{z}_{MG} \tag{2.38}$$

where $\overline{z}_{MG}$ is defined as the data adjustment vector. From Eq.(2.37), the *j*-th element of vector $\overline{z}_{MG}$ represents the magnitude of self-shielded multi-group cross-section adjustment along the *j*-th singular vector of $\overline{\overline{\mathbf{U}}}_{MG,t}$, divided by the square root of the *j*-th singular value.

---

[4] $\overline{\overline{\mathbf{C}}}_{CO_m}$ is treated as a diagonal matrix. With real plant data, $\overline{\overline{\mathbf{C}}}_{CO_m}$ is expected to be block diagonal, with each block containing measurement correlations because of periodic LPRM/TIP calibration [17]. Therefore, $n^2$ storage requirement (with $n \sim 10^5$) is not expected. The pseudoinverse representation is adopted to plan for any future rank deficiency in the prior core observables covariance matrix because of measurement correlations.

The physical interpretation of this change in variables is explained in the following example. Suppose that $\overline{\overline{\mathbf{C}}}_{MG}$ is a diagonal matrix where the diagonal elements represent the variance of each self-shielded multi-group cross-section. The *j*-th singular vector of $\overline{\overline{\mathbf{C}}}_{MG}$ is the standard basis vector $\overline{e}_j$ and the *j*-th singular value is the variance of the *j*-th self-shielded multi-group cross-section. Eq. (2.37) and Eq. (2.38) become:

$$\overline{z}_{MG,j} = \frac{1}{SD(\overline{x}_{MG_0,j})}\langle \overline{e}_j, \overline{x}_{MG} - \overline{x}_{MG_0} \rangle = \frac{\overline{x}_{MG,j} - \overline{x}_{MG_0,j}}{SD(\overline{x}_{MG_0,j})} \tag{2.39}$$

$$\overline{x}_{MG,j} = \overline{x}_{MG_0,j} + SD(\overline{x}_{MG_0,j})\overline{z}_{MG,j} \tag{2.40}$$

where $SD(\overline{x}_{MG_0,j})$ is the standard deviation in the *j*-th self-shielded multi-group cross-section. Eq. (2.40) states that if $\overline{z}_{MG,j}$ equals one, then the *j*-th self-shielded multi-group cross-section is adjusted by one standard deviation. In the general case of Eq. (2.37), $\overline{z}_{MG,j}$ represents the number of "standard deviations" the self-shielded multi-group cross-sections are adjusted along the orthornomal direction specified by the *j*-th singular vector of $\overline{\overline{\mathbf{C}}}_{MG}$. Because of the truncated-SVD representation of $\overline{\overline{\mathbf{C}}}_{MG}$, the dimension of $\overline{z}_{MG}$ is only *t* as compared to *n* in the above example. Using this change in variables, Eq. (2.35) reduces to:

$$\overline{\tilde{z}}_{MG} = \min_{\overline{z}_{MG}}\left\{\left\| \begin{bmatrix} \overline{\overline{\mathbf{\Sigma}}}_{CO_m}^{-1/2}\overline{\overline{\mathbf{U}}}_{CO_m}^{T}(\overline{y}_{CO_m} - \overline{y}_{CO_0}) \\ 0 \end{bmatrix} - \begin{bmatrix} \overline{\overline{\mathbf{\Sigma}}}_{CO_m}^{-1/2}\overline{\overline{\mathbf{U}}}_{CO_m}^{T}\overline{\overline{\mathbf{S}}}_{CS}\overline{\overline{\mathbf{S}}}_{LP}\overline{\overline{\mathbf{U}}}_{MG_t}\overline{\overline{\mathbf{\Sigma}}}_{MG}^{1/2} \\ \alpha\overline{\overline{\mathbf{I}}} \end{bmatrix}\overline{z}_{MG} \right\|_2^2\right\} \tag{2.41}$$

where $\bar{\tilde{z}}_{MG}$ is the posterior data adjustment vector. The approach to solving Eq. (2.41) builds upon the ESM solution method for uncertainty propagation. Using matrices $\bar{\bar{\Psi}}_{LP,t_2}$ and $\bar{\bar{R}}^{T}_{CS,t_2}$ from Section 2.2.3, the following thin SVD is defined:

$$\begin{gathered}\bar{\bar{\Sigma}}^{-1/2}_{CO_m}\bar{\bar{U}}^{T}_{CO_m}\bar{\bar{R}}_{CS,t_2}\bar{\bar{\Psi}}^{T}_{LP,t_2}=\bar{\bar{U}}_{t_3}\bar{\bar{\Sigma}}_{t_3}\bar{\bar{V}}^{T}_{t_3}\\ \bar{\bar{U}}\ is\ n\times t_3\\ \bar{\bar{\Sigma}}\ is\ t_3\times t_3\\ \bar{\bar{V}}^{T}\ is\ t_3\times t\\ t_3\le t_2\le t\end{gathered}\tag{2.42}$$

Using the thin SVD in Eq. (2.42), it is shown in Appendix A that the solution to Eq. (2.41) is the following (cf. - Eq. (2.32)):[5]

$$\begin{gathered}\bar{\tilde{z}}_{MG}=\bar{\bar{V}}(\bar{\bar{\Sigma}}^{2}+\alpha^{2}\bar{\bar{I}})^{-1}\bar{\bar{\Sigma}}\bar{\bar{U}}^{T}\bar{\bar{\Sigma}}^{-1/2}_{CO_m}\bar{\bar{U}}^{T}_{CO_m}(\bar{y}_{CO_m}-\bar{y}_{CO_0})\\ \bar{\tilde{x}}_{MG}=\bar{x}_{MG_0}+\bar{\bar{U}}_{MG,t}\bar{\bar{\Sigma}}^{1/2}_{MG,t}\bar{\tilde{z}}_{MG}\\ \bar{\tilde{x}}_{FG}=\mathbf{\Theta}_{LP}(\bar{\tilde{x}}_{MG})\cong\bar{x}_{FG_0}+\bar{\bar{R}}_{LP,t}\bar{\tilde{z}}_{MG}\\ \bar{\tilde{y}}_{CO}=\mathbf{\Theta}_{CS}(\mathbf{\Theta}_{LP}(\bar{\tilde{x}}_{MG}))\cong\bar{y}_{CO_0}+\bar{\bar{R}}_{CS,t_2}\bar{\bar{\Psi}}^{T}_{LP,t_2}\bar{\tilde{z}}_{MG}\\ \bar{\bar{C}}_{MG,post}=\bar{\bar{U}}_{MG,t}\bar{\bar{\Sigma}}^{1/2}_{MG,t}\bar{\bar{V}}(\bar{\bar{\Sigma}}^{2}+\alpha^{2}\bar{\bar{I}})^{-2}(\bar{\bar{\Sigma}}^{2}+\alpha^{4}\bar{\bar{I}})\bar{\bar{V}}^{T}\bar{\bar{\Sigma}}^{1/2}_{MG,t}\bar{\bar{U}}^{T}_{MG,t}\\ \bar{\bar{C}}_{FG,post}=\bar{\bar{R}}_{LP,t}\bar{\bar{V}}(\bar{\bar{\Sigma}}^{2}+\alpha^{2}\bar{\bar{I}})^{-2}(\bar{\bar{\Sigma}}^{2}+\alpha^{4}\bar{\bar{I}})\bar{\bar{V}}^{T}\bar{\bar{R}}^{T}_{LP,t}\\ \bar{\bar{C}}_{CO,post}=\bar{\bar{R}}_{CS,t_2}\bar{\bar{\Psi}}^{T}_{LP,t_2}\bar{\bar{V}}(\bar{\bar{\Sigma}}^{2}+\alpha^{2}\bar{\bar{I}})^{-2}(\bar{\bar{\Sigma}}^{2}+\alpha^{4}\bar{\bar{I}})\bar{\bar{V}}^{T}\bar{\bar{\Psi}}_{LP,t_2}\bar{\bar{R}}^{T}_{CS,t_2}\end{gathered}\tag{2.43}$$

[5] In this formulation, the Tikhonov regularization parameter is assumed be nonzero. If the Tikhonov regularization parameter is zero, the matrix $(\bar{\bar{\Sigma}}^{2}+\alpha^{2}\bar{\bar{I}})^{-1}$ is replaced by the pseudoinverse $(\bar{\bar{\Sigma}}^{2})^{\dagger}$.

where $\bar{\tilde{x}}_{MG}$ is the posterior self-shielded multi-group cross-sections, $\bar{\tilde{x}}_{FG}$ is the posterior few-group cross-sections, $\bar{\tilde{y}}_{CO}$ is the posterior core observables, $\bar{\bar{\mathbf{C}}}_{MG,post}$ is the posterior self-shielded multi-group cross-section covariance matrix, $\bar{\bar{\mathbf{C}}}_{FG,post}$ is the posterior few-group cross-section covariance matrix, and $\bar{\bar{\mathbf{C}}}_{CO,post}$ is the posterior core observables covariance matrix. In Chapter 4, posterior values $\bar{\tilde{x}}_{MG}$, $\bar{\tilde{x}}_{FG}$, $\bar{\tilde{y}}_{CO}$, $\bar{\bar{\mathbf{C}}}_{MG,post}$, $\bar{\bar{\mathbf{C}}}_{FG,post}$, and $\bar{\bar{\mathbf{C}}}_{CO,post}$ are given for a BWR case study along with selection of the Tikhonov regularization parameter.

# 3. Cross-Section Uncertainty Propagation

In this section, the uncertainty propagation calculations outlined in Chapter 2 are now described in more detail. These calculations involve 1) propagating ENDF cross-section covariance data to calculate the self-shielded multi-group cross-section covariance matrix, 2) propagating the self-shielded multi-group cross-section covariance matrix through the lattice physics model TRITON, and 3) propagating the few-group cross-section covariance matrix through the core-simulator model FORMOSA-B [47]. In step 1), PUFF-IV processes the ENDF covariance files to calculate an infinitely-dilute multi-group cross-section covariance matrix. Additional calculations are necessary to quantify the uncertainty in self-shielded multi-group cross-sections used in the lattice physics calculation. To perform these calculations, the resonance treatment model in TRITON was modified to quantify this uncertainty contribution due to spatial and energy resonance self-shielding effects for each fuel pin. In Section 3.1, the modified resonance self-shielding model is presented and the uncertainty propagation calculations are described.

As a result of the calculations described in Section 3.1, the truncated-rank of the self-shielded multi-group cross-section covariance matrix is 2223. This rank is still too large to compute the few-group cross-section covariance matrix for a representative number of lattice cases (i.e. a set of burnup dependent few-group cross-sections for a given fuel color and thermal hydraulic condition). To reduce the number of lattice physics forward perturbation calculations, a GPT-based approach was employed to approximate the action of the lattice

physics sensitivity matrix on the self-shielded multi-group cross-section covariance matrix. This GPT-based approach is used to reduce the number of lattice physics forward perturbations calculations to 481 per lattice case. These calculations are summarized in Section 3.2.

As a result of the calculations described in Section 3.2, the truncated-rank of the few-group cross-section covariance matrix is 362. This implies that 362 core simulator forward perturbation calculations are necessary to calculate the core observables covariance matrix. The analysis of these calculations for a BWR/4 reload core design is deferred to Chapter 4.

## 3.1. Multi-Group Cross-Section Covariance Matrix

### 3.1.1. PUFF-IV Methodology

Quantifying multi-group cross-section uncertainty due to ENDF cross-section uncertainty constitutes a major contribution to BWR ACS in this work. Repeating from Chapter 2, this calculation is given as:

$$\overline{\overline{\mathbf{C}}}_{MG} = \overline{\overline{\mathbf{S}}}_{XP}\,\overline{\overline{\mathbf{C}}}_{ENDF}\,\overline{\overline{\mathbf{S}}}_{XP}^{T} \tag{3.1}$$

where $\overline{\overline{\mathbf{C}}}_{ENDF}$ is the ENDF cross-section covariance matrix, $\overline{\overline{\mathbf{S}}}_{XP}$ is the cross-section preparation code sensitivity matrix, and $\overline{\overline{\mathbf{C}}}_{MG}$ is the self-shielded multi-group cross-section covariance matrix. The ENDF cross-section files contain 1) the point-wise cross-section data, 2) resonance parameter data that characterizes the sharp energy variation of the cross-section

in the resolved resonance energy range, 3) point-wise cross-section covariance data, and 4) the resonance parameter covariance data. The point-wise cross-section data are represented in vector form as $\bar{\sigma}_{PW}$ where each element corresponds to a unique point-wise cross-section for a given reaction type and isotope at a specific neutron kinetic energy. Similarly, the point-wise cross-section covariance data is represented in matrix form as $\bar{\bar{\mathbf{C}}}_{PW}$. Since cross-sections for each isotope are measured independently (with the possible exception of ratio measurements to determine fission cross-sections), $\bar{\bar{\mathbf{C}}}_{PW}$ is sparse, block diagonal in structure with each diagonal block corresponding to a given isotope. Likewise, the resonance parameter data is represented as $\bar{x}_{RP}$ and $\bar{\bar{\mathbf{C}}}_{RP}$. Combining the covariance data from both of these matrices, $\bar{\bar{\mathbf{C}}}_{ENDF}$ is given as:

$$\bar{\bar{\mathbf{C}}}_{ENDF} = \begin{bmatrix} \bar{\bar{\mathbf{C}}}_{PW} & \bar{\bar{0}} \\ \bar{\bar{0}} & \bar{\bar{\mathbf{C}}}_{RP} \end{bmatrix} \tag{3.2}$$

Although $\bar{\bar{\mathbf{C}}}_{PW}$ and $\bar{\bar{\mathbf{C}}}_{RP}$ are represented as uncorrelated in Eq. (3.2), each matrix characterizes two components of the uncertainty in the resolved resonance energy region. From the PUFF-IV code manual [45], the point-wise cross-section covariance data in the resolved resonance energy region characterize the cross-section correlations attributed to the interaction of cross-section resonances over many energy ranges (i.e. – long-range components). The short-range components of the cross-section covariance data are attributed to the uncertainty of individual cross-section resonances as well as the interaction of cross-

section resonances in the neighborhood of an individual resonance. Combining the long-range and short-range covariance components by Eq. (3.2) completely describes the cross-section uncertainty over the full cross-section energy range.

Cross-section preparation codes generate multi-group cross-sections by 1) constructing the neutron cross-section component described by the resonance parameters over an ultra-fine energy mesh (i.e. - ~$10^5$ energy grid points), 2) adding the resonance parameter cross-section component to the point-wise cross-section component, and 3) homogenizing the combined cross-section using an ultra-fine neutron flux spectra. This calculation is represented by the following:

$$\bar{\sigma}_{ID} = \overline{\overline{\mathbf{H}}}_{ID}(\overline{\overline{\mathbf{P}}}\bar{\sigma}_{PW} + \bar{\mathbf{\Pi}}(\bar{x}_{RP})) \tag{3.3}$$

where $\bar{\sigma}_{ID}$ is the multi-group cross-section vector, $\overline{\overline{\mathbf{H}}}_{ID}$ is the energy-averaging homogenization operator, $\overline{\overline{\mathbf{P}}}$ is a prolongation operator the maps $\bar{\sigma}_{PW}$ from the ENDF point-wise energy mesh to the ultra-fine energy mesh, and $\bar{\mathbf{\Pi}}$ is the nonlinear operator that maps cross-section resonance parameters to cross-section values on the ultra-fine energy mesh.

Similar to multi-group cross-section preparation codes, PUFF-IV calculates multi-group cross-section covariance matrices by applying the sandwich rule to the ENDF cross-section covariance matrix and the computational model in Eq. (3.3). The multi-group cross-section covariance matrix $\overline{\overline{\mathbf{C}}}_{ID}$ is given by the following:

$$\begin{aligned}\overline{\overline{\mathbf{C}}}_{ID} &= \begin{bmatrix}\overline{\overline{\mathbf{S}}}_{PW} & \overline{\overline{\mathbf{S}}}_{RP}\end{bmatrix}\begin{bmatrix}\overline{\overline{\mathbf{C}}}_{PW} & \overline{\overline{0}} \\ \overline{\overline{0}} & \overline{\overline{\mathbf{C}}}_{RP}\end{bmatrix}\begin{bmatrix}\overline{\overline{\mathbf{S}}}^{T}_{PW} \\ \overline{\overline{\mathbf{S}}}^{T}_{RP}\end{bmatrix} \\ &= \overline{\overline{\mathbf{S}}}_{PW}\overline{\overline{\mathbf{C}}}_{PW}\overline{\overline{\mathbf{S}}}^{T}_{PW} + \overline{\overline{\mathbf{S}}}_{RP}\overline{\overline{\mathbf{C}}}_{RP}\overline{\overline{\mathbf{S}}}^{T}_{RP} \\ &= \overline{\overline{\mathbf{C}}}_{LR} + \overline{\overline{\mathbf{S}}}_{RP}\overline{\overline{\mathbf{C}}}_{RP}\overline{\overline{\mathbf{S}}}^{T}_{RP}\end{aligned} \tag{3.4}$$

where $\overline{\overline{\mathbf{S}}}_{PW} = \overline{\overline{\mathbf{H}}}_{ID}\overline{\overline{\mathbf{P}}}$ and $\overline{\overline{\mathbf{S}}}_{RP} = \overline{\overline{\mathbf{H}}}_{ID}\overline{\overline{\mathbf{\Pi}}}$. PUFF-IV has many options to analytically calculate the sensitivity matrix $\overline{\overline{\mathbf{\Pi}}}$ for the nonlinear operator $\overline{\mathbf{\Pi}}$ evaluated at the prior mean values of the resonance parameters. In the last expression in Eq. (3.4), the matrix $\overline{\overline{\mathbf{C}}}_{LR}$ is used to represent $\overline{\overline{\mathbf{S}}}_{PW}\overline{\overline{\mathbf{C}}}_{PW}\overline{\overline{\mathbf{S}}}^{T}_{PW}$. This matrix represents the long-range uncertainty contribution to the multi-group cross-section covariance matrix as well as the uncertainties in multi-group cross-sections for energy ranges above and below the resolved resonance energy region.

PUFF-IV was used to calculate the 44GROUPV6REC multi-group cross-section covariance file that is used for this work. A complete description of 44GROUPV6REC is given in [48]. In generating the 44GROUPV6REC covariance file, a 1/E neutron flux spectrum was used to homogenize the ultra-fine cross-sections. The subscript "ID" in $\bar{\sigma}_{ID}$, $\overline{\overline{\mathbf{H}}}_{ID}$, and $\overline{\overline{\mathbf{C}}}_{ID}$ is used to denote the infinitely-dilute approximation used in generating multi-group cross-section covariance matrices. It is well known that infinitely-dilute multi-group cross-sections can differ with multi-group cross-sections that account for spatial and energy resonance self-shielding by several orders of magnitude. Consequently, the self-shielded multi-group cross-section covariance matrix $\overline{\overline{\mathbf{C}}}_{MG}$ can differ from $\overline{\overline{\mathbf{C}}}_{ID}$. Unfortunately, the self-shielded neutron flux spectra that accounts for spatial and energy resonance self-

shielding effects for each fuel pin depends on local thermal hydraulic conditions and fuel pin number densities. It is computationally infeasible to calculate $\overline{\overline{\mathbf{C}}}_{MG}$ for each fuel pin at each burnup step for each lattice case using problem-dependent self-shielded neutron flux spectra. In the following section, the Nordheim Integral Treatment is presented to calculate $\overline{\overline{\mathbf{C}}}_{MG}$ for a single unit cell (i.e. - fuel pin/clad/coolant "unit" used to construct the lattice). The modified resonance self-shielding model presented in Section 3.1.3 is used to consistently perturb the self-shielded multi-group cross-sections for any unit cell in the lattice physics uncertainty calculations.

### 3.1.2. Nordheim Integral Treatment

In the Nordheim Integral Treatment Method presented in the NITAWL code manual [49], the unit cell is represented by two spatial regions: the absorber region containing the resonance absorber (i.e. – resonance-absorbing isotope) and the external moderator region. By using first-flight escape probabilities to describe the neutron transport into and out of each region, as well as the reciprocity relationship between the first-flight escape probabilities in these two regions, the following equation can be shown to describe the energy-dependent neutron flux in the absorber region over a given cross-section resonance[1]:

$$\Sigma_t(E,T)\phi(E,T) = (1-P_0^*(E,T))\sum_{j=1}^{3}\int_{E}^{E/(1-\alpha_j)}\frac{\Sigma_{s,j}(E',T)\phi(E',T)}{E'}dE' + P_0^*(E,T)\Sigma_t(E,T)W(E) \quad (3.5)$$

[1] The reader is referred to [49] and its references for more detail on derivation and computational solution of Eq. (3.5), as well as the determination of the Dancoff-correction factor.

where $\phi(E,T)$ is the self-shielded neutron flux over the cross-section resonance energy range, $\Sigma_t(E,T)$ is the total macroscopic cross-section of the absorber region, $P_0^*(E,T)$ is the Dancoff-corrected escape probability of the absorber region, $\Sigma_{s,j}(E,T)$ is the macroscopic scattering cross-section of mixture-*j* in the absorber region, *W(E)* is the neutron slowing-down source in the external moderator region, and $\alpha_j$ is the parameter used to describe the neutron energy loss due to elastic scattering. In this formulation, $\alpha_j$ is equal to $4A_j/(A_j+1)^2$, where $A_j$ is the effective nuclide mass of mixture-*j*. (Note that this definition of alpha is actually 1 minus alpha in many sources [49].) The temperature dependence is explicitly shown in the variables above to indicate the use of Doppler-broadened cross-sections.

Eq. (3.5) is referred to as the Nordheim Integral Equation, and is used to determine the self-shielded neutron flux for both clad-region resonance absorbers and fuel-region resonance absorbers. For clad-region resonance absorbers, the absorber region in Eq. (3.5) is the clad volume and the external moderator region is the fuel and coolant volume. Likewise for fuel-region resonance absorbers, the absorber region is the fuel volume and the external moderator is the clad and coolant volume. Once the self-shielded neutron flux is determined for all cross-section resonances for a given resonance absorber, the self-shielded multi-group cross-sections for that resonance absorber are determined by the following equations:

$$\sigma_{x,g,T}^{shielded} = \sigma_{x,g,T_{ref}}^{\infty} + \Delta_{x,g,T} \tag{3.6}$$

$$\Delta_{x,g,T} \equiv \sum_i \left( \frac{\int_{E_g}^{E_{g-1}} \sigma_{x,i}(E',T)\phi_i(E',T)dE'}{\int_{E_g}^{E_{g-1}} \phi_i(E',T)dE'} - \frac{\int_{E_g}^{E_{g-1}} \sigma_{x,i}(E',T_{ref})\frac{dE'}{E'}}{\int_{E_g}^{E_{g-1}} \frac{dE'}{E'}} \right) \quad (3.7)$$

where $\sigma_{x,g,T}^{shielded}$ is the self-shielded multi-group cross-section, $\sigma_{x,g,T_{ref}}^{\infty}$ is the reference infinitely-dilute multi-group cross-section, $\Delta_{x,g,T}$ is the multi-group cross-section resonance self-shielding correction factor, $\phi_i(E,T)$ is the self-shielded neutron flux at the *i*-th cross-section resonance, and $\sigma_{x,i}(E,T)$ is the Doppler-broadened Single-Level Breit Wigner (SLBW) microscopic cross-section at the *i*-th cross-section resonance at fuel temperature *T*. The multi-group cross-section terms $\sigma_{x,g,T}^{shielded}$, $\sigma_{x,g,T_{ref}}^{\infty}$, and $\Delta_{x,g,T}$, are given for fission, capture, and scattering reactions and for all energy groups in the resolved resonance energy region. The summation in Eq. (3.7) is taken over all cross-section resonances within the energy range of group *g* for a given resonance absorber. The variable $\Delta_{x,g,T}$ is simply referred to as the resonance correction factor and is similar to the Bondarenko self-shielding factors used in many lattice physics codes.

The self-shielded multi-group cross-section equation (Eq. (3.6)) and the energy-averaging homogenization equation to determine $\Delta_{x,g,T}$ (Eq. (3.7)) are closely related to the energy-averaging homogenization equation used by the multi-group cross-section preparation code (Eq. (3.3)). To see this, Eq. (3.6) is rewritten in matrix-vector form as:

$$\begin{aligned} \bar{\sigma}_{SS} &= \bar{\sigma}_{ID} + \bar{\Delta} \\ \Rightarrow \bar{\sigma}_{SS} &= \bar{\bar{\mathbf{H}}}_{ID}(\bar{\bar{\mathbf{P}}}\bar{\sigma}_{PW} + \bar{\mathbf{\Pi}}(\bar{x}_{RP})) + \bar{\Delta} \\ \Rightarrow \bar{\sigma}_{SS} &= \bar{\bar{\mathbf{H}}}_{ID}(\bar{\bar{\mathbf{P}}}\bar{\sigma}_{PW} + \bar{\mathbf{\Pi}}(\bar{x}_{RP})) + \bar{\mathbf{H}}_{\Delta}(\bar{x}_{RP}) \end{aligned} \tag{3.8}$$

where $\bar{\mathbf{H}}_{\Delta}(\bar{x}_{RP})$ is a nonlinear operator that maps the cross-section resonance parameters $\bar{x}_{RP}$ to the resonance correction factor vector $\bar{\Delta}$. Linearizing Eq. (3.8) about the prior mean values of the point-wise cross-sections ($\bar{\sigma}_{PW_0}$) and resonance parameters ($\bar{x}_{RP_0}$), then the first-order approximation is given as:

$$\bar{\sigma}_{SS} - \bar{\sigma}_{SS_0} \cong \left[\bar{\bar{\mathbf{S}}}_{PW} \quad (\bar{\bar{\mathbf{S}}}_{RP} + \bar{\bar{\mathbf{H}}}_{\Delta})\right]\begin{bmatrix} \bar{\sigma}_{PW} - \bar{\sigma}_{PW_0} \\ \bar{x}_{RP} - \bar{x}_{RP_0} \end{bmatrix} \tag{3.9}$$

where $\bar{\bar{\mathbf{H}}}_{\Delta}$ is the sensitivity matrix for the nonlinear homogenization operator $\bar{\mathbf{H}}_{\Delta}$. Alternatively, the linearized system of equations is written as:

$$\bar{\sigma}_{MG} - \bar{\sigma}_{MG_0} \equiv \begin{bmatrix} \bar{\sigma}_{ID} - \bar{\sigma}_{ID_0} \\ \bar{\Delta} - \bar{\Delta}_0 \end{bmatrix} = \begin{bmatrix} \bar{\bar{\mathbf{S}}}_{PW} & \bar{\bar{\mathbf{S}}}_{RP} \\ \bar{\bar{0}} & \bar{\bar{\mathbf{H}}}_{\Delta} \end{bmatrix}\begin{bmatrix} \bar{\sigma}_{PW} - \bar{\sigma}_{PW_0} \\ \bar{x}_{RP} - \bar{x}_{RP_0} \end{bmatrix} \tag{3.10}$$

where the self-shielded multi-group cross-section vector $\bar{\sigma}_{MG}$ is now formally defined as the set of infinitely-dilute multi-group cross-sections and the set of resonance correction factors.

The sandwich rule is now applied to Eq. (3.10) to determine the self-shielded multi-group cross-section covariance matrix $\overline{\overline{\mathbf{C}}}_{MG}$ as:

$$\begin{aligned}\overline{\overline{\mathbf{C}}}_{MG} &= \overline{\overline{\mathbf{S}}}_{XP}\,\overline{\overline{\mathbf{C}}}_{ENDF}\,\overline{\overline{\mathbf{S}}}_{XP}^{T} \\ &= \begin{bmatrix} \overline{\overline{\mathbf{S}}}_{PW} & \overline{\overline{\mathbf{S}}}_{RP} \\ \overline{\overline{0}} & \overline{\overline{\mathbf{H}}}_{\Delta} \end{bmatrix} \begin{bmatrix} \overline{\overline{\mathbf{C}}}_{PW} & \overline{\overline{0}} \\ \overline{\overline{0}} & \overline{\overline{\mathbf{C}}}_{RP} \end{bmatrix} \begin{bmatrix} \overline{\overline{\mathbf{S}}}_{PW}^{T} & \overline{\overline{0}} \\ \overline{\overline{\mathbf{S}}}_{RP}^{T} & \overline{\overline{\mathbf{H}}}_{\Delta}^{T} \end{bmatrix} \\ &= \begin{bmatrix} \overline{\overline{\mathbf{C}}}_{ID} & \overline{\overline{\mathbf{S}}}_{RP}\overline{\overline{\mathbf{C}}}_{RP}\overline{\overline{\mathbf{H}}}_{\Delta}^{T} \\ \overline{\overline{\mathbf{H}}}_{\Delta}\overline{\overline{\mathbf{C}}}_{RP}\overline{\overline{\mathbf{S}}}_{RP}^{T} & \overline{\overline{\mathbf{H}}}_{\Delta}\overline{\overline{\mathbf{C}}}_{RP}\overline{\overline{\mathbf{H}}}_{\Delta}^{T} \end{bmatrix} \end{aligned} \tag{3.11}$$

where $\overline{\overline{\mathbf{C}}}_{ID}$ is the infinitely-dilute multi-group cross-section covariance matrix given by 44GROUPV6REC, $\overline{\overline{\mathbf{H}}}_{\Delta}\overline{\overline{\mathbf{C}}}_{RP}\overline{\overline{\mathbf{H}}}_{\Delta}^{T}$ represents the uncertainty in resonance correction factors due to the uncertainty in resonance parameters, and the off-diagonal terms $\overline{\overline{\mathbf{S}}}_{RP}\overline{\overline{\mathbf{C}}}_{RP}\overline{\overline{\mathbf{H}}}_{\Delta}^{T}$ and $\overline{\overline{\mathbf{H}}}_{\Delta}\overline{\overline{\mathbf{C}}}_{RP}\overline{\overline{\mathbf{S}}}_{RP}^{T}$ represent the correlations between the uncertainties in resonance correction factors and infinitely-dilute multi-group cross-sections induced by the uncertainties in resonance parameters.

The covariance matrix given by Eq. (3.11) characterizes the uncertainty for only one unit cell and for one resonance absorber. The dimension of this covariance matrix is $(44N_x*2)$ x $(44N_x*2)$ where $N_x$ is the total number of reaction types for the resonance absorber and the number of energy groups is 44. Considering a second unit cell that contains a different number density of the resonance absorber or is at a different thermal-hydraulic condition, the self-shielded neutron flux computed by the Nordheim Integral Equation is

different than the first unit cell. This leads to a different resonance correction factor. Likewise, the self-shielded multi-group cross-section covariance matrix for the second unit cell is different due to different sensitivities to the resonance parameters. However, the uncertainties in self-shielded multi-group cross-sections for each unit cell are correlated with one another. This is evident by rewriting Eq. (3.10) and Eq. (3.11) for a two unit cell system:

$$\bar{\sigma}_{MG} - \bar{\sigma}_{MG_0} \equiv \begin{bmatrix} \bar{\sigma}_{ID} - \bar{\sigma}_{ID_0} \\ \bar{\Delta}^1 - \bar{\Delta}_0^1 \\ \bar{\Delta}^2 - \bar{\Delta}_0^2 \end{bmatrix} = \begin{bmatrix} \bar{\bar{\mathbf{S}}}_{PW} & \bar{\bar{\mathbf{S}}}_{RP} \\ \bar{\bar{0}} & \bar{\bar{\mathbf{H}}}_{\Delta}^1 \\ \bar{\bar{0}} & \bar{\bar{\mathbf{H}}}_{\Delta}^2 \end{bmatrix} \begin{bmatrix} \bar{\sigma}_{PW} - \bar{\sigma}_{PW_0} \\ \bar{x}_{RP} - \bar{x}_{RP_0} \end{bmatrix} \tag{3.12}$$

$$\bar{\bar{\mathbf{C}}}_{MG} = \begin{bmatrix} \bar{\bar{\mathbf{C}}}_{ID} & \bar{\bar{\mathbf{S}}}_{RP} \bar{\bar{\mathbf{C}}}_{RP} \bar{\bar{\mathbf{H}}}_{\Delta}^{1\,T} & \bar{\bar{\mathbf{S}}}_{RP} \bar{\bar{\mathbf{C}}}_{RP} \bar{\bar{\mathbf{H}}}_{\Delta}^{2\,T} \\ \bar{\bar{\mathbf{H}}}_{\Delta}^1 \bar{\bar{\mathbf{C}}}_{RP} \bar{\bar{\mathbf{S}}}_{RP}^T & \bar{\bar{\mathbf{H}}}_{\Delta}^1 \bar{\bar{\mathbf{C}}}_{RP} \bar{\bar{\mathbf{H}}}_{\Delta}^{1\,T} & \bar{\bar{\mathbf{H}}}_{\Delta}^1 \bar{\bar{\mathbf{C}}}_{RP} \bar{\bar{\mathbf{H}}}_{\Delta}^{2\,T} \\ \bar{\bar{\mathbf{H}}}_{\Delta}^2 \bar{\bar{\mathbf{C}}}_{RP} \bar{\bar{\mathbf{S}}}_{RP}^T & \bar{\bar{\mathbf{H}}}_{\Delta}^2 \bar{\bar{\mathbf{C}}}_{RP} \bar{\bar{\mathbf{H}}}_{\Delta}^{1\,T} & \bar{\bar{\mathbf{H}}}_{\Delta}^2 \bar{\bar{\mathbf{C}}}_{RP} \bar{\bar{\mathbf{H}}}_{\Delta}^{2\,T} \end{bmatrix} \tag{3.13}$$

where $\bar{\bar{\mathbf{C}}}_{MG}$ has dimension $(44N_x)*3$ x $(44N_x)*3$. This process is naturally extended to an $N_u$ unit cell system where $\bar{\bar{\mathbf{C}}}_{MG}$ has dimension $(44N_x)*(N_u+1)$ x $(44N_x)*(N_u+1)$.

### 3.1.3. Modified Resonance Self-Shielding Model

The modified resonance self-shielding model has been developed so that resonance correction factors are accurately approximated by linear interpolation. In other words, the Nordheim Integral Treatment is used to calculate resonance correction factors for a finite set

of unit cells, which are then used as an interpolation mesh for all other unit cell calculations. The dimension and spectral properties of $\overline{\overline{\mathbf{C}}}_{MG}$ are determined by the number of unit cells used to construct the interpolation table.

The resonance correction factors $\overline{\Delta}$ are functionalized in terms of six system parameters that describe the local conditions of the unit cell. The six system parameters are the temperature of the resonance absorber ($T$), the Dancoff correction factor ($C$), the macroscopic potential scattering cross-section of the internal moderators ($\Sigma_{p,2}$ and $\Sigma_{p,3}$), the mass of the second internal moderator ($M_3$), and the number density of the resonance absorber ($N_1$):

$$\overline{\Delta} = \overline{f}(T, C, \Sigma_{p,2}, \Sigma_{p,3}, M_3, N_1) \tag{3.14}$$

The subscript indexing of the independent variables was chosen to be consistent with the notation used in the NITAWL code manual. For this work, the first internal moderator is always Oxygen, and the mass of Oxygen is not included in the functionalization. The mass of the second internal moderator depends on the number density of all the other moderating isotopes in the absorber region.

Lattice physics calculations were performed using the Nordheim Integral Treatment to determine the number of data points, or interpolation mesh, to accurately approximate $\overline{\Delta}$. Three lattice designs (i.e. - 1 reflector, 1 vanished, and 1 dominant lattice) were depleted at nominal void fractions of 0%, 40%, and 80%. At each burnup step, 6 thermal hydraulic

branch conditions were also simulated. From this set of lattice physics calculations, the six independent variables of Eq. (3.14) were stored for each unit cell calculation along with the resonance correction factor for each reaction type and energy group. From this data, the following conclusions were made for each of the six independent variables in Eq. (3.14):

- Temperature ($T$) - Nine fuel temperatures are required ranging from 293K to 879K. The fuel temperatures were chosen such that linear interpolation in terms of $\sqrt{T}$ accurately determines lattice k-infinity (i.e. – neutron multiplication factor) to within 50 pcm. Two clad temperatures were chosen for clad-region resonance absorbers.

- Dancoff correction factor ($C$) - Four Dancoff correction factors are used for the fuel-region resonance absorbers. These values correspond to the four thermal hydraulic conditions of the coolant (0%, 40%, and 80% void fraction at 560K and 0% void fraction at 293K). For clad-region resonance absorbers, the fuel is treated as part of the external moderator region in determining the Dancoff correction factor. The Dancoff correction factor varies slightly due to changes in fuel-region nuclide concentrations. Two Dancoff correction factors are needed for linear interpolation at each of the four thermal hydraulic conditions of the coolant.[2]

- Macroscopic potential scattering cross-section of the first internal moderator ($\Sigma_{p,2}$) - For fuel-region resonance absorbers, the macroscopic potential scattering cross-section of Oxygen ($\Sigma_{p,O}$) varies slightly with burnup since Oxygen nuclides in the fuel-region are tracked in the depletion calculation. Only two values of $\Sigma_{p,O}$ are used to linear interpolate the resonance correction factors. Since the clad-region nuclide concentrations are not tracked in the depletion calculation, only one value of $\Sigma_{p,2}$ is needed for clad-region resonance absorbers.

- Macroscopic potential scattering cross-section of the second moderator ($\Sigma_{p,3}$) - $\Sigma_{p,3}$ changes with burnup due to changes in the fuel-region nuclide concentrations.

[2] As a default, TRITON calculates Dancoff correction factors by assuming an infinite repetitive lattice of identical fuel pins. For strong neighbor effects (e.g. - water holes, control rods, etc.), TRITON does allow for user-defined Dancoff correction factors, but this requires external calculations to determine the neighbor effects for each fuel pin. For this work, we assume that the infinite repetitive lattice assumption is reasonable for calculating sensitivity coefficients for BWR ACS. For future work, it is expected that accounting for neighbor effects would minimally impact the functionalization described here.

However, because of the large number density of uranium-238 (U-238), $\Sigma_{p,3}$ is dominated by the macroscopic potential scattering cross-section of U-238. Since the U-238 number density varies slightly with burnup, only two values of $\Sigma_{p,3}$ are needed for fuel region resonance absorbers other than U-238. For U-238, $\Sigma_{p,3}$ shows more burnup dependence as well as dependence on initial burnable poison (BP) concentration. Twenty values of $\Sigma_{p,3}$ are used to accurately determine the shielded multi-group cross-section with linear interpolation for U-238. For clad-region resonance absorbers, only one value of $\Sigma_{p,3}$ is needed.

- Mass of the second moderator ($M_3$) - The functional dependence on the mass of the second moderator is similar to $\Sigma_{p,3}$. Only two values of $M_3$ are needed for linear interpolation for fuel-region resonance absorbers other than U-238. U-238 requires five values for accurate linear interpolation. Only one value for $M_3$ is necessary for clad- region resonance absorbers.

- Number density of the resonance absorber ($N_1$) - The variations of number density concentration are different for each fuel-region resonance absorber and can change up to 6 orders of magnitude. The resonance correction factors are fitted using linear interpolation over 5-15 values of $\log_{10}(N_1)$. Only one value of $N_1$ is required for clad-region resonance absorbers. The $\log_{10}$ fit is consistent with the functionalization of the background cross-section in lattice physics codes that use Bondarenko factor interpolation tables.

The number of mesh points required for each input parameter for each resonance absorber in the lattice physics model is summarized in Table 3.1. Table 3.1 also gives the mesh points for resonance absorbers in surrounding structural materials. TRITON treats each resonance absorber in the surrounding structural materials as infinite media. Thus, resonance calculations for these nuclides only need to be done once and used for all burnup steps, void fractions, and branch conditions. The overhead computing cost to build the interpolation table requires ~$10^5$ unit cell calculations using NITAWL. This is two orders of magnitude smaller than the number of required calculations if the Nordheim Integral Equation is solved

for each unit cell, burnup step, and lattice case. For each interpolation point, the computed resonance correction factor for fission, capture, and scattering multi-group cross-sections are stored and then used in the interpolation procedure in the modified resonance self-shielding model.

Comparisons of k-infinity as a function of burnup were made between TRITON calculations using NITAWL and the modified resonance self-shielding model. Each model was used to calculate burnup-dependent k-infinities for a dominant and vanished lattice design at three different void fractions. The chosen lattice designs had different enrichment and BP loadings than the lattices used to determine the interpolation mesh. The maximum reactivity difference over all test cases was -15 pcm at BOC, -20 pcm at the Gadolinium peak, and 35 pcm at End-of-cycle. The average run-time to generate self-shielded multi-group cross-sections for a single unit cell was 0.1 seconds for the modified resonance self-shielding model and 9 seconds using NITAWL. These calculations were performed using a 2.8 GHz Intel Xeon processor.

### 3.1.4. Uncertainty Propagation

In this section, the generation of the self-shielded multi-group cross-section covariance matrix is described. First, uncertainty data from the 44GROUPV6REC covariance file is used to construct the infinitely-dilute multi-group cross-section covariance matrix. The 44GROUPV6REC covariance file contains covariance data for 77 isotopes used in the lattice physics model. For these isotopes, 221 covariance matrices are given in 44 x 44 energy group structure that characterize the uncertainty for a specific cross-section reaction type. The

isotope and reaction type for each covariance matrix is listed in Table 3.2. In addition to this set of covariance matrices, 118 covariance matrices are provided that characterize the covariances between different reaction types of the same isotope. These correlations between different reaction types arise from either the resonance model for each isotope or from the nature of the cross-section measurement. In previous work on BWR ACS ([1] and [9]), the 44GROUPANLCOV and 44GROUPV5COV covariance files contained covariances of cross-section reaction-types across different isotopes. These covariances do not exist in the 44GROUPV6REC covariance file.

Due to the lack of covariance data for resonance parameters, only 13 of the 77 isotopes contain resonance parameter covariance data: Gd-152, Gd-154, Gd-155, Gd-156, Gd-157, Gd-158, Gd-160, U-235, U-238, Pu-239, Pu-240, Pu-242, and Am-241. For the remaining 54 isotopes, the multi-group cross-section uncertainty in the resolved resonance region is either zero or is approximated by processing tabulated resonance parameter uncertainty information given in [50]. For these 54 isotopes, the uncertainty in the resonance correction factor is fully-correlated to the uncertainty in infinitely-dilute multi-group cross-sections. This is a reasonable assumption for minor actinides and fission product isotopes that can be modeled as infinitely-dilute at low burnup or for high-energy cross-section resonances where the neutron flux depression across the resonance is minimal. The uncertainties in self-shielded multi-group cross-sections in the unresolved resonance region are assumed to be fully correlated to the uncertainty in infinitely-dilute multi-group cross-sections. This is due to the lack of covariance data for the Bondarenko self-shielding factors in the unresolved resonance region. This is a reasonable assumption given that BWR core observables are not

expected to be highly sensitive to multi-group cross-sections in the unresolved resonance region.

The self-shielded multi-group cross-section covariance matrix $\overline{\overline{\mathbf{C}}}_{MG}$ is partitioned into a 170 x 170 block diagonal form. The first 157 diagonal blocks correspond to infinitely-dilute multi-group covariance matrices for the 54 isotopes without resonance parameter covariance data. The eigenvalue decomposition (EVD) of these 157 blocks reveal several negative eigenvalues that are orders of magnitude smaller than the largest positive eigenvalue for each block. Since the uncertainty contribution for these negative eigenvalues is negligible, each matrix block is reconstructed using only the positive eigenvalues and their associated eigenvectors. All positive eigenvalues less than the absolute value of the largest negative eigenvalue are also removed. The reconstructed matrix blocks are symmetric, positive semi-definite, and are now described in terms of SVD rather than EVD. The truncated-rank of this section of $\overline{\overline{\mathbf{C}}}_{MG}$ (i.e. – the first 157 diagonal blocks) is 728, which is an order of magnitude smaller than the dimension of this section of $\overline{\overline{\mathbf{C}}}_{MG}$ (7788 x 7788).

The 13 remaining diagonal blocks of $\overline{\overline{\mathbf{C}}}_{MG}$ correspond to the 13 isotopes that have cross section resonance parameter data. These matrix blocks contain covariance data for both the infinitely-dilute multi-group cross-sections and the resonance correction factors as described in Section 3.1.3. The number of unit cells for each isotope is given in Table 3.1. Using the Pu-242 covariance matrix block as an example, $\overline{\overline{\mathbf{C}}}_{ID}$ is 220 x 220 (i.e. fission, capture, elastic, inelastic, and n2n cross-sections), $\overline{\overline{\mathbf{C}}}_{RP}$ is 232 x 232, $\overline{\overline{\mathbf{S}}}_{RP}$ is 220 x 232, $N_u$=2600, and $\overline{\overline{\mathbf{H}}}_{\Delta}^{i}$ is 220 x 232 for i=1,2,…,$N_u$. The final size of $\overline{\overline{\mathbf{C}}}_{MG}$ for Pu-242 is 572,220

x 572,220. The resonance parameter covariance matrix is given for 67 cross-section resonances in SLBW format where there is no covariance given between resonance parameters at different resonance energies. In SLBW format, covariance data is available for the resonance energy, the neutron line width, the capture line width, and the fission line width. The sensitivity matrix $\overline{\overline{\mathbf{S}}}_{RP}$ is determined by the forward perturbation approach where each of the 232 resonance parameters are perturbed independently and the change in the infinitely-dilute multi-group cross-section is determined. Similarly, the sensitivity matrix $\overline{\overline{\mathbf{H}}}_{\Delta}^{i}$ is computed by perturbing each resonance parameter and determining the change in the resonance correction factor for the *i*-th unit cell. In total, the $\overline{\overline{\mathbf{C}}}_{MG}$ matrix block for Pu-242 requires 232 NITAWL calculations to compute $\overline{\overline{\mathbf{S}}}_{RP}$, and 232 NITAWL calculations to compute $\overline{\overline{\mathbf{H}}}_{\Delta}^{i}$ for each of the 2600 unit cells. The first 150 eigenvalues and eigenvectors of $\overline{\overline{\mathbf{C}}}_{MG}$ are computed using the MATLAB function `eigs`. The `eigs` function only requires the action of $\overline{\overline{\mathbf{C}}}_{MG}$ operating on a vector. This matrix-vector product is efficiently calculated by the much smaller matrices $\overline{\overline{\mathbf{C}}}_{ID}$ $\overline{\overline{\mathbf{C}}}_{RP}$, $\overline{\overline{\mathbf{S}}}_{RP}$, and $\overline{\overline{\mathbf{H}}}_{\Delta}^{i}$.

Similar to the first 157 matrix blocks, the EVD calculations in MATLAB reveal negative eigenvalues that are much smaller than the largest positive eigenvalue for each of the remaining covariance blocks. The negative eigenvalues are removed from these covariance blocks and the truncated-SVD of $\overline{\overline{\mathbf{C}}}_{MG}$ contains 2223 singular values and associated singular vectors. The size and rank of each matrix block is summarized in Table 3.3, and the singular values of $\overline{\overline{\mathbf{C}}}_{MG}$ are plotted in Figure 3.1.

It is important to note that the resonance parameter covariance matrix for the Gadolinium isotopes, U-235, U-238, and Pu-239 are given in Reich-Moore (RM) format. The RM format allows for possible interference effects among neighboring resonances. Therefore, the resonance parameter covariance matrix $\overline{\overline{\mathbf{C}}}_{RP}$ is dense as compared to the sparse, block diagonal matrix structure in the SLBW format. For this work, it is assumed that the use of $\overline{\overline{\mathbf{C}}}_{RP}$ in RM format is valid even though the NITAWL computational model computes resonance correction factors for SLBW cross-section resonances. This assumption is discussed in more detail in Chapter 5. For fissile isotopes in RM format, the two fission channel line widths are added together to form an equivalent SLBW fission width.

The impact of resonance parameter uncertainty on lattice k-infinity uncertainty is shown to be higher when accounting for spatial and energy resonance self-shielding affects as opposed to simply using the infinitely-dilute multi-group cross-section uncertainties. For example, one of the major contributors to lattice k-infinity uncertainty is the U-238 capture cross-section. The U-238 multi-group capture cross-section in energy group form is given as a function of neutron energy in Figure 3-1. In addition, the absolute standard deviation for this cross-section is graphed in Figure 3-2, the relative standard deviation (RSD) is given in Figure 3-3, and the lattice k-infinity relative sensitivity coefficient for this cross-section is given in Figure 3-4. The lattice k-infinity sensitivity coefficients are computed for a dominant lattice modeled at Beginning-of-Life (BOL) with 40% nominal void fraction. In these figures, the infinitely-dilute multi-group cross-section is denoted “ID” and the self-shielded multi-group cross-section is denoted “SS”. The infinitely-dilute cross-section is shown to be one to two orders of magnitude higher than the self-shielded cross-section.

Likewise, the absolute standard deviation of the infinitely-dilute cross-section is one to two orders of magnitude higher than the uncertainty in the self-shielded cross-section. Because neutron resonance capture is deemphasized due to spatial and energy resonance self-shielding effects, the absolute standard deviation of the self-shielded cross-section is expected to be lower than the absolute standard deviation of the infinitely-dilute cross-section. However, the RSD of the self-shielded cross-section is shown to be higher than the RSD of the infinitely-dilute cross-section for some energy groups. For energy group 17 (i.e. – neutron energies above 30 eV and below 100 eV), the self-shielded cross-section RSD is 5.5%. The uncertainty in the infinitely-dilute group-17 capture cross-section is 3.0%. This increase in RSD has been verified by using the analytic expressions of resonance capture integrals in terms of SLBW resonance parameters in [51] to compare the RSD in infinitely-dilute cross-sections with the RSD in self-shielded cross-sections using the narrow resonance infinite mass approximation.

The increase in the RSD of the self-shielded multi-group cross-section is shown to increase the uncertainty in lattice k-infinity. Figure 3-4 displays the lattice k-infinity sensitivity coefficients for U-238 self-shielded multi-group capture cross-sections in the resolved resonance energy range. Because U-238 low-lying resonances have large capture line widths, the k-infinity sensitivity coefficients have negative sign. For energy group 17, the relative sensitivity coefficient is negative 2.80%. This energy group covers three important low-lying resonances of U-238: 1) the 36.67 eV cross-section resonance (with 5.98% capture line width uncertainty), 2) the 66.01 eV cross-section resonance (with 6.85% capture line width uncertainty), and 3) the 80.73 eV cross-section resonance (with 14.1%

capture line width uncertainty). Accounting for the spatial and energy resonance self-shielding effects on the multi-group cross-section uncertainty, the group-17 U-238 capture cross-section uncertainty contribution to lattice k-infinity uncertainty is 0.154%. Using the infinitely-dilute multi-group cross-section uncertainties (i.e. – assuming the self-shielding effects are negligible), the uncertainty contribution to lattice k-infinity uncertainty is only 0.084%. Although the group-17 k-infinity uncertainty contribution differs by 45%, the difference in the energy-integrated uncertainty contribution for the U-238 capture cross-section is much smaller (i.e. 0.291% (self-shielded) compared to 0.255% (infinitely-dilute)). This analysis shows that spatial and energy resonance self-shielding effect must be accounted for in propagating cross-section uncertainty, and that group-wise uncertainty contribution can very significantly.

## 3.2. Generation of the Few-Group Cross-Section Covariance Matrix

Quantifying few-group cross-section uncertainty due to multi-group cross-section uncertainty is addressed in the dissertation of Abdel-Khalik [1] and by the author, Abdel-Khalik and Turinsky in [9]. Using the same ESM-based approach, the calculations in this work address three inadequacies of the previous work. First, the uncertainty contribution from multi-group cross-section uncertainty in the resolved resonance energy range is correctly quantified. Recalling from Section 2.2.3, the few-group cross-section covariance matrix $\overline{\overline{\mathbf{C}}}_{FG}$ is computed by running a series of lattice physics calculations in which the self-shielded multi-group cross-sections are perturbed along the singular vectors of $\overline{\overline{\mathbf{C}}}_{MG}$. In the

previous work, the pre-shielded multi-group cross-sections were perturbed along the singular vectors of the infinitely-dilute multi-group cross-section covariance matrix given by the 44GROUPV5COV and 44GROUPANLCOV covariance files. The self-shielded multi-group cross-sections in the resolved resonance energy range are computed by Eq. (3.6), which overwrites the pre-shielded multi-group cross-section with the infinitely-dilute multi-group cross-section minus the resonance correction factor. Therefore, the few-group cross-section uncertainty quantification calculations in the previous work do not account for multi-group cross-section uncertainty in the resolved resonance energy range for any resonance absorbing isotope listed in Table 3.1. The calculations in the previous work do account for the following: 1) the uncertainty in all reaction types that are unaffected by spatial and energy resonance self-shielding effects (e.g. – chi, nu-bar, (n,n'), (n,2n), etc.), 2) the uncertainty attributed from all non-resonance absorbers (e.g. – H-1 and O-16), and 3) the uncertainty in the resonance absorbers' multi-group cross-sections in the thermal and unresolved resonance energy ranges.

Second, the few-group cross-section uncertainty quantification calculations in this work account for multiple lattice cases, which are defined as a set of burnup dependent few-group cross-sections for a given fuel color and thermal hydraulic condition. Recalling from Section 2.2.3, the few-group cross-section uncertainty propagation equation is given as:

$$\begin{aligned} \overline{\overline{\mathbf{C}}}_{FG} &= \overline{\overline{\mathbf{S}}}_{LP}\,\overline{\overline{\mathbf{C}}}_{MG}\,\overline{\overline{\mathbf{S}}}_{LP}^{T} \\ &= (\overline{\overline{\mathbf{S}}}_{LP}\,\overline{\overline{\mathbf{U}}}_{MG,t}\,\overline{\overline{\mathbf{\Sigma}}}_{MG,t}^{1/2})(\overline{\overline{\mathbf{S}}}_{LP}\,\overline{\overline{\mathbf{U}}}_{MG,t}\,\overline{\overline{\mathbf{\Sigma}}}_{MG,t}^{1/2})^{T} \\ &= \overline{\overline{\mathbf{R}}}_{LP,t}\,\overline{\overline{\mathbf{R}}}_{LP,t}^{T} \end{aligned} \tag{3.15}$$

where $\overline{\overline{\mathbf{U}}}_{MG,t}\overline{\overline{\mathbf{\Sigma}}}_{MG,t}\overline{\overline{\mathbf{U}}}^{T}_{MG,t}$ is the truncated-SVD of $\overline{\overline{\mathbf{C}}}_{MG}$. The lattice physics sensitivity matrix $\overline{\overline{\mathbf{S}}}_{LP}$ is $10^6$ x *n* where *n* is the number of rows of $\overline{\overline{\mathbf{C}}}_{MG}$. Similar to the matrix partitioning of $\overline{\overline{\mathbf{C}}}_{MG}$ for $N_u$ unit cells, $\overline{\overline{\mathbf{C}}}_{FG}$ is partitioned into an $N_l$ x $N_l$ matrix where $N_l$ is the number of lattice cases used to describe the few-group cross-sections. To see this, Eq. (3.15) is rewritten for $N_l$=3 as:

$$\overline{\overline{\mathbf{C}}}_{FG} = \begin{bmatrix} \overline{\overline{\mathbf{S}}}^{1}_{LP} \\ \overline{\overline{\mathbf{S}}}^{2}_{LP} \\ \overline{\overline{\mathbf{S}}}^{3}_{LP} \end{bmatrix} \overline{\overline{\mathbf{C}}}_{MG} \begin{bmatrix} \overline{\overline{\mathbf{S}}}^{1\ T}_{LP} & \overline{\overline{\mathbf{S}}}^{2\ T}_{LP} & \overline{\overline{\mathbf{S}}}^{3\ T}_{LP} \end{bmatrix} \tag{3.16}$$

or

$$\overline{\overline{\mathbf{C}}}_{FG} = \begin{bmatrix} \overline{\overline{\mathbf{R}}}^{1}_{LP,t} \\ \overline{\overline{\mathbf{R}}}^{2}_{LP,t} \\ \overline{\overline{\mathbf{R}}}^{3}_{LP,t} \end{bmatrix} \begin{bmatrix} \overline{\overline{\mathbf{R}}}^{1\ T}_{LP,t} & \overline{\overline{\mathbf{R}}}^{2\ T}_{LP,t} & \overline{\overline{\mathbf{R}}}^{3\ T}_{LP,t} \end{bmatrix} \tag{3.17}$$

where $\overline{\overline{\mathbf{R}}}^{i}_{LP,t}$ is the lattice physics response matrix for the *i*-th lattice case and i=1,2,or 3. If ~$10^3$ few-group cross-sections are computed for each lattice case, then the dimensions of $\overline{\overline{\mathbf{R}}}^{i}_{LP,t}$ for this example are $10^3$ x *t* and the computing cost to construct $\overline{\overline{\mathbf{C}}}_{FG}$ is 3**t* lattice-physics calculations. For the BWR/4 reload core design analyzed in this work and in previous work, $N_l$ is equal to 777 (i.e. – 37 fuel colors * 3 void fractions * 7 thermal

hydraulic or control rod conditions). This implies 777**t* lattice physics calculations are required for the computation of $\overline{\overline{\mathbf{C}}}_{FG}$. Since this number of lattice physics calculations is too large using current computing resources, $\overline{\overline{\mathbf{R}}}^{i}_{LP,t}$ is only calculated for a few lattice cases. In [1], Abdel-Khalik calculated $\overline{\overline{\mathbf{R}}}^{i}_{LP,t}$ for 2 lattice cases and the computed lattice physics response matrices was assumed fully correlated to lattice cases of similar type. The 44GROUPV5COV covariance file was used to construct $\overline{\overline{\mathbf{C}}}_{MG}$, and the truncated-rank *t* was equal to 200. In [9], $\overline{\overline{\mathbf{R}}}^{i}_{LP,t}$ was calculated for 1 lattice case and then assumed a fully correlated lattice physics response matrix to all lattice cases. The 44GROUPANLCOV covariance file was used and *t* was equal to 900. In both cases, the correlation was based on the relative change in few-group cross-sections in response to multi-group cross-section perturbations (e.g. - a 10% change in $\sigma^{25}_{f2}$ in lattice case *i* implies a 10% change in $\sigma^{25}_{f2}$ for similar lattice *j*).

For this work, 10 lattice physics response matrices are computed and then assumed fully correlated to the remaining lattice cases. The chosen lattice cases include one bottom axial blanket modeled at 0% void fraction, one dominant lattice modeled at 40% void fraction (i.e. - nominal calculation + 6 branch calculations), one vanished lattice modeled at 80% void fraction, and one top axial blanket modeled at 80% void fraction. This subset of lattice cases should provide a representative measure of the few-group cross-section uncertainty that is to be propagated through the core simulation calculations.

The final contribution in this work in calculating $\overline{\overline{\mathbf{C}}}_{FG}$ is reducing the required number of lattice physics calculations using a GPT-based sensitivity analysis to determine the number of important singular vectors of the self-shielded multi-group covariance matrix that significantly contribute to the uncertainty in few-group cross-sections. In the previous work [9], expert judgment was used in determining that 900 singular vectors of $\overline{\overline{\mathbf{C}}}_{MG}$ contributed to the few-group cross-section covariance matrix. Only principle directions for fissile isotopes, Gd, H-1, O-16, and Zr were considered. Without prior knowledge of the few-group cross-section sensitivity coefficients along each singular vectors of $\overline{\overline{\mathbf{C}}}_{MG}$, a conservative singular value cutoff criteria was used in previous work in order to prevent removing a singular vector with large few-group cross-section sensitivity and small singular value (i.e. - $\sigma_{900}/\sigma_1$=1e-6). The GPT-based approach is used to generate sensitivity coefficients for peak pin power, detector fission power, and k-infinity for each singular vector of $\overline{\overline{\mathbf{C}}}_{MG}$. The magnitudes of the sensitivity coefficients are scaled by the square root of the singular values of $\overline{\overline{\mathbf{C}}}_{MG}$, and then used as a qualitative measure of the "worth" of the singular vector in terms of peak pin power uncertainty, detector fission power uncertainty, or k-infinity uncertainty. These three responses were chosen because of their similarity to key core attributes such a core k-effective, LPRM detector response, cold shutdown margin, and thermal limits that depend on peak pin power.

The use of GPT to generate first-order accurate sensitivity coefficients has been extensively used in the field of reactor physics, and the underlying theory is given in numerous historical papers [30]-[34]. For this reason, the equations used to determine GPT

sensitivity coefficients and the solution methods to determine the generalized importance function for each response are not provided in this work.[3]

To generate sensitivity coefficients for the three responses above, four TRITON calculations in adjoint mode are required. (The fundamental mode calculation precedes the GPT calculation for each of the three responses). These four calculations were computed for numerous statepoints in the lattice physics calculation to account for the change in sensitivity coefficients to various physical conditions such as void fraction, fuel temperature, control rod insertion, and burnup. For burnup steps beyond BOL, the change in the sensitivity coefficient with respect to changes in the time-dependent nuclide concentrations was assumed to be zero. This assumption leads to large errors in the End-of-Life (EOL) sensitivity coefficients for important cross-sections such as the U-238 capture cross-section that strongly affects plutonium and minor actinide buildup. For this reason, the GPT sensitivity coefficients only at BOL were used to identify 481 singular vectors of $\overline{\overline{\mathbf{C}}}_{MG}$ that significantly contribute to the uncertainty in few-group cross-sections. If the EOL sensitivity coefficient error was small, the sensitivity coefficients can be used to reduce the number of lattice physics calculations since the changes in peak pin power, detector fission power, and k-infinity for the selected 481 singular vectors are expected to by highly correlated. This is discussed in more detail in the recommendations for future work in Section 5.2.

[3] The calculation of the critical eigenvalue sensitivity coefficient is generally not classified as a GPT problem, since it only requires the determination of the fundamental mode of the adjoint eigenvalue problem. For this work, the k-infinity sensitivity coefficient is defined as a generalized response using the critical-spectrum corrected neutron flux calculated in TRITON. Accounting for the critical-spectrum leakage effects, the generalized adjoint source to determine first-order accurate changes in k-infinity is nonzero, making the k-infinity sensitivity analysis a GPT problem.

Using the selected subspace of $\overline{\overline{\mathbf{C}}}_{MG}$ with truncated-rank $t$ equal to 481, the few-group cross-section covariance matrix is computed using Eq. (3.15) from the 4810 lattice physics calculations. The SVD of the few-group cross-section covariance matrix $\overline{\overline{\mathbf{C}}}_{FG}$ reveals a rank reduction as uncertainty is propagated through the lattice physics calculation. The truncated-rank of $\overline{\overline{\mathbf{C}}}_{FG}$ (i.e. $t_2$) was selected to be 362 by using an absolute singular value cutoff of 1e-8 in order to accurately approximate the relative standard deviation in k-infinity to within 0.01%. This cutoff criterion is of the same order of magnitude as the modeling error uncertainty and the linearization error of the lattice physics model. Using Eq.(2.22), the core observables covariance matrix is calculated from the 362 core simulations. The singular value spectrum of each covariance matrix is given in Figure 3-6. The singular value spectrum denoted "MG2" represents the selected 481 singular values of the 2223 singular values of $\overline{\overline{\mathbf{C}}}_{MG}$, which is denoted "MG" on the graph. It is noted that several large singular values have been removed in the GPT analysis because of low sensitivities to lattice k-infinity, detector fission power, and peak pin power that would have otherwise been included in the calculations in previous work. The largest rank reduction occurs in propagating the uncertainty data provided in ENDF to the self-shielded multi-group cross-section matrix. For this calculation, the changes in infinitely-dilute multi-group cross-sections due to changes in resonance parameters are highly correlated when many cross-section resonance are located in the same energy group. The resonance parameter sensitivity coefficients to the resonance correction factors in the interpolation tables are also highly correlated. The rank reduction in the few-group cross-section covariance matrix is explained

by the strong correlations introduced by multi-group cross-section homogenization. The rank reduction in the core observables covariance matrix is not as significant as the cross-section covariance matrices. This is due to large similarities in the lattice physics sensitivity matrix and the core simulator sensitivity covariance matrix. For example, if the reactor core could be approximated as 2-D infinite sea of the identical fuel lattice, then the core simulator sensitivity matrix would be identical to the lattice physics sensitivity matrix and the rank reduction would be zero.

This concludes the ESM analysis of the uncertainty propagation calculations. In summary, calculating the core observables covariance matrix requires: 1) ~$10^5$ unit cell calculations to generate the interpolation table of resonance correction factors used in the modified resonance self-shielding model, 2) an additional ~$10^7$ unit cell calculations to compute the multi-group cross-section sensitivity coefficients to resonance parameters, 3) ~$10^3$ lattice physics calculations, and 4) ~$10^2$ core simulator calculations. For the evaluation of core observables uncertainties of future fuel cycles, only a subset of these calculations must be recomputed. For example, if the fresh fuel assembly design for the next reload cycle is unaltered (i.e. - same mechanical design, initial enrichment loading, and initial BP loading as current or previous fuel assemblies), then only the ~$10^2$ core simulator calculations need to be recomputed using the adjusted few-group cross-sections and their posterior uncertainties. The lattice physics calculations only need to be recomputed if the fresh fuel assembly initial enrichment loading or initial BP loading is significantly different than current or previous fuel assembly designs. In this case, only the 481 lattice physics calculations need to be recalculated for the lattice designs associated with the newly-designed fresh fuel assemblies.

In addition, two scenarios exist in which the unit cell calculations must be recomputed: 1) the lattice physics modeling methodology is significantly changed (e.g. – additional 90% nominal void fraction calculations must be implemented to accurately model few-group cross-sections in high-void regions of the core), or 2) changes in the fuel pin geometry (e.g. - fuel radius, clad thickness, and lattice pitch). In the latter case, unit cell calculations are required to evaluate resonance correction factors that reflect the change in fuel pin geometry. In addition, the resonance correction factor sensitivity coefficients must be evaluated with respect to the posterior resonance parameter covariance matrix and posterior infinitely-dilute multi-group cross-section covariance matrix. Although the evaluation of the posterior resonance parameter covariance matrix and posterior infinitely-dilute multi-group cross-section covariance matrix is beyond the scope of this work, these matrices can be readily evaluated from the adjusted resonance correction factors.

Table 3.1 Interpolation mesh for modified resonance self-shielding model.

| Isotope | Absorber type | # of T x C mesh points | # of $\Sigma_{p,2}$ mesh points | # of $M_1$ mesh points | # of $\Sigma_{p,3}$ mesh points | # of $N_1$ mesh points | Total # of mesh points |
|---|---|---|---|---|---|---|---|
| Cr-Nat | clad | 8 | 1 | 1 | 1 | 1 | 8 |
| | structure | 1 | 1 | 1 | 1 | 1 | 1 |
| Mn-55 | structure | 8 | 1 | 1 | 1 | 1 | 8 |
| Fe-Nat | clad | 8 | 1 | 1 | 1 | 1 | 8 |
| | structure | 1 | 1 | 1 | 1 | 1 | 1 |
| Ni-Nat | clad | 8 | 1 | 1 | 1 | 1 | 8 |
| Kr-86 | fuel | 25 | 2 | 2 | 2 | 7 | 1400 |
| Zr-Nat | clad | 8 | 1 | 1 | 1 | 1 | 8 |
| | structure | 1 | 1 | 1 | 1 | 1 | 1 |
| Zr-94 | fuel | 25 | 2 | 2 | 2 | 7 | 1400 |
| Mo-95 | fuel | 25 | 2 | 2 | 2 | 13 | 2600 |
| Tc-99 | fuel | 25 | 2 | 2 | 2 | 9 | 1800 |
| Rh-103 | fuel | 25 | 2 | 2 | 2 | 11 | 2200 |
| Ag-109 | fuel | 25 | 2 | 2 | 2 | 11 | 2200 |
| Sn-112 | clad | 8 | 1 | 1 | 1 | 1 | 8 |
| | structure | 1 | 1 | 1 | 1 | 1 | 1 |
| Sn-114 | clad | 8 | 1 | 1 | 1 | 1 | 8 |
| | structure | 1 | 1 | 1 | 1 | 1 | 1 |
| Sn-115 | clad | 8 | 1 | 1 | 1 | 1 | 8 |
| | structure | 1 | 1 | 1 | 1 | 1 | 1 |
| Sn-116 | clad | 8 | 1 | 1 | 1 | 1 | 8 |
| | structure | 1 | 1 | 1 | 1 | 1 | 1 |
| Sn-117 | clad | 8 | 1 | 1 | 1 | 1 | 8 |
| | structure | 1 | 1 | 1 | 1 | 1 | 1 |
| Sn-118 | clad | 8 | 1 | 1 | 1 | 1 | 8 |
| | structure | 1 | 1 | 1 | 1 | 1 | 1 |
| Sn-119 | clad | 8 | 1 | 1 | 1 | 1 | 8 |
| | structure | 1 | 1 | 1 | 1 | 1 | 1 |
| Sn-120 | clad | 8 | 1 | 1 | 1 | 1 | 8 |
| | structure | 1 | 1 | 1 | 1 | 1 | 1 |
| Sn-122 | clad | 8 | 1 | 1 | 1 | 1 | 8 |
| | structure | 1 | 1 | 1 | 1 | 1 | 1 |
| Sn-124 | clad | 8 | 1 | 1 | 1 | 1 | 8 |
| | structure | 1 | 1 | 1 | 1 | 1 | 1 |
| Xe-131 | fuel | 25 | 2 | 2 | 2 | 9 | 1800 |
| Cs-133 | fuel | 25 | 2 | 2 | 2 | 9 | 1800 |
| Nd-143 | fuel | 25 | 2 | 2 | 2 | 11 | 2200 |

Table 3.1 (continued).

| Isotope | Absorber type | # of T x C mesh points | # of $\Sigma_{p,2}$ mesh points | # of $M_1$ mesh points | # of $\Sigma_{p,3}$ mesh points | # of $N_1$ mesh points | Total # of mesh points |
|---|---|---|---|---|---|---|---|
| Nd-145 | fuel | 25 | 2 | 2 | 2 | 7 | 1400 |
| Nd-148 | fuel | 25 | 2 | 2 | 2 | 7 | 1400 |
| Sm-149 | fuel | 25 | 2 | 2 | 2 | 5 | 1000 |
| Sm-150 | fuel | 25 | 2 | 2 | 2 | 11 | 2200 |
| Sm-151 | fuel | 25 | 2 | 2 | 2 | 7 | 1400 |
| Sm-152 | fuel | 25 | 2 | 2 | 2 | 9 | 1800 |
| Eu-151 | fuel | 25 | 2 | 2 | 2 | 5 | 1000 |
| Eu-153 | fuel | 25 | 2 | 2 | 2 | 9 | 1800 |
| Eu-154 | fuel | 25 | 2 | 2 | 2 | 9 | 1800 |
| Eu-155 | fuel | 25 | 2 | 2 | 2 | 7 | 1400 |
| Gd-152 | fuel | 25 | 2 | 2 | 2 | 11 | 2200 |
| Gd-154 | fuel | 25 | 2 | 2 | 2 | 13 | 2600 |
| Gd-155 | fuel | 25 | 2 | 2 | 2 | 15 | 3000 |
| Gd-156 | fuel | 25 | 2 | 2 | 2 | 13 | 2600 |
| Gd-157 | fuel | 25 | 2 | 2 | 2 | 15 | 3000 |
| Gd-158 | fuel | 25 | 2 | 2 | 2 | 15 | 3000 |
| Gd-160 | fuel | 25 | 2 | 2 | 2 | 15 | 3000 |
| Hf- Nat | clad | 8 | 1 | 1 | 1 | 1 | 8 |
| | structure | 1 | 1 | 1 | 1 | 1 | 1 |
| U-234 | fuel | 25 | 2 | 2 | 2 | 7 | 1400 |
| U-235 | fuel | 25 | 2 | 2 | 2 | 11 | 2200 |
| U-236 | fuel | 25 | 2 | 2 | 2 | 7 | 1400 |
| U-238 | fuel | 25 | 2 | 5 | 20 | 2 | 10000 |
| Np-237 | fuel | 25 | 2 | 2 | 2 | 9 | 1800 |
| Pu-238 | fuel | 25 | 2 | 2 | 2 | 11 | 2200 |
| Pu-239 | fuel | 25 | 2 | 2 | 2 | 7 | 1400 |
| Pu-240 | fuel | 25 | 2 | 2 | 2 | 13 | 2600 |
| Pu-242 | fuel | 25 | 2 | 2 | 2 | 13 | 2600 |
| Am-241 | fuel | 25 | 2 | 2 | 2 | 11 | 2200 |
| Am-243 | fuel | 25 | 2 | 2 | 2 | 11 | 2200 |
| Cm-242 | fuel | 25 | 2 | 2 | 2 | 9 | 1800 |
| Cm-243 | fuel | 25 | 2 | 2 | 2 | 7 | 1400 |
| Cm-244 | fuel | 25 | 2 | 2 | 2 | 11 | 2200 |
| | | | | | | **Total** | **93335** |

Table 3.2 Cross-sections with quantified covariance data.

| Index | Isotope | Reaction Types |
|---|---|---|
| 1 | H-1 | (n,n), (n,g) |
| 2 | B-10 | (n,n), (n,a), (n,g) |
| 3 | B-11 | (n,n), (n,g) |
| 4 | C-Nat | (n,p), (n,d), (n,a), (n,n'), (n,n), (n,g) |
| 5 | N-14 | (n,n), (n,g) |
| 6 | O-16 | (n,n'), (n,g), (n,p), (n,d), (n,n), (n,a) |
| 7 | Si-Nat | (n,p), (n,a), (n,n), (n,n'), (n,g) |
| 8 | P-31 | (n,n), (n,g) |
| 9 | Mn-55 | (n,n), (n,g), (n,n'), (n,2n), (n,p), (n,d), (n,t), (n,He-3), (n,a) |
| 10 | Kr-83 | (n,g) |
| 11 | Zr-Nat | (n,n), (n,n'), (n,g) |
| 12 | Zr-94 | (n,n), (n,g) |
| 13 | Nb-93 | (n,n), (n,n'), (n,2n)(n,g) |
| 14 | Mo-95 | (n,n), (n,g) |
| 15 | Tc-99 | (n,n), (n,g) |
| 16 | Ru-106 | (n,g) |
| 17 | Rh-103 | (n,g) |
| 18 | Rh-105 | (n,g) |
| 19 | Ag-109 | (n,n), (n,g) |
| 20 | Sn-112 | (n,n), (n,g) |
| 21 | Sn-114 | (n,n), (n,g) |
| 22 | Sn-115 | (n,g) |
| 23 | Sn-116 | (n,g) |
| 24 | Sn-117 | (n,g) |
| 25 | Sn-118 | (n,n), (n,g) |
| 26 | Sn-119 | (n,n), (n,g) |
| 27 | Sn-120 | (n,n), (n,g) |
| 28 | Sn-122 | (n,g) |
| 29 | Sn-124 | (n,n), (n,g) |
| 30 | Xe-131 | (n,g) |
| 31 | Xe-135 | (n,g) |
| 32 | Cs-133 | (n,n), (n,g) |
| 33 | Cs-134 | (n,g) |
| 34 | Cs-135 | (n,g) |
| 35 | Cs-137 | (n,g) |
| 36 | Ce-144 | (n,g) |
| 37 | Pr-143 | (n,g) |
| 38 | Nd-143 | (n,n), (n,g) |

Table 3.2 (continued).

| Index | Isotope | Reaction Types |
|---|---|---|
| 39 | Nd-145 | (n,n), (n,g) |
| 41 | Nd-147 | (n,g) |
| 42 | Nd-148 | (n,g) |
| 43 | Pm-147 | (n,n), (n,g) |
| 44 | Pm-148 | (n,g) |
| 45 | Pm-149 | (n,g) |
| 46 | Sm-147 | (n,n), (n,g) |
| 47 | Sm-149 | (n,n), (n,g) |
| 48 | Sm-150 | (n,n), (n,g) |
| 49 | Sm-151 | (n,n), (n,g) |
| 50 | Sm-152 | (n,n), (n,g) |
| 51 | Eu-151 | (n,n), (n,g) |
| 52 | Eu-153 | (n,n), (n,g) |
| 53 | Eu-154 | (n,g) |
| 54 | Eu-155 | (n,g) |
| 55 | Gd-152 | (n,n), (n,g), (n,n'), (n,2n), (n,p) |
| 56 | Gd-154 | (n,n), (n,g), (n,n'), (n,2n), (n,p), (n,a) |
| 57 | Gd-155 | (n,n), (n,g), (n,n'), (n,2n), (n,p) |
| 58 | Gd-156 | (n,n), (n,g), (n,n'), (n,2n), (n,p), (n,a) |
| 59 | Gd-157 | (n,n), (n,g), (n,n'), (n,2n), (n,p) |
| 60 | Gd-158 | (n,n), (n,g), (n,n'), (n,2n), (n,p), (n,a) |
| 61 | Gd-160 | (n,n), (n,g), (n,n'), (n,2n), (n,p), (n,a) |
| 62 | Hf-Nat | (n,n), (n,g) |
| 63 | U-234 | (n,n), (n,f), (n,g) |
| 64 | U-235 | (n,n'), (n,2n), (n,n), (n,f), (n,g), nu-bar, chi |
| 65 | U-236 | (n,n), (n,f), (n,g) |
| 66 | U-238 | (n,n'), (n,2n), (n,n), (n,f), (n,g), nu-bar, chi |
| 67 | Np-237 | nu-bar, (n,n), (n,f), (n,g) |
| 68 | Pu-238 | nu-bar, (n,n), (n,f), (n,g) |
| 69 | Pu-239 | (n,n'), (n,2n), (n,n), (n,f), (n,g), nu-bar, chi |
| 70 | Pu-240 | (n,n'), (n,2n), (n,n), (n,f), (n,g), nu-bar, chi |
| 71 | Pu-241 | (n,n'), (n,2n), (n,n), (n,f), (n,g), nu-bar, chi |
| 72 | Pu-242 | (n,n'), (n,2n), (n,n), (n,f), (n,g), chi |
| 73 | Am-241 | (n,n'), (n,2n), (n,n), (n,f), (n,g), nu-bar |
| 74 | Am-243 | (n,f), (n,g) |
| 75 | Cm-242 | (n,f), (n,g) |
| 76 | Cm-243 | nu-bar, (n,f), (n,g) |
| 77 | Cm-244 | (n,n), (n,f), (n,g) |

Table 3.3 Rank and dimension of the self-shielded multi-group cross-section covariance matrix.

| Matrix Block | Isotope | RP uncertainty format | truncated-rank of block | # of rows of block |
|---|---|---|---|---|
| 1-157 | -- | n/a | 728 | 7788 |
| 158 | Gd-152 | RM | 77 | 193688 |
| 159 | Gd-154 | RM | 106 | 228888 |
| 160 | Gd-155 | RM | 143 | 264088 |
| 161 | Gd-156 | RM | 91 | 228888 |
| 162 | Gd-157 | RM | 102 | 264088 |
| 163 | Gd-158 | RM | 105 | 264088 |
| 164 | Gd-160 | RM | 112 | 264088 |
| 165 | U-235 | RM | 83 | 484220 |
| 166 | U-238 | RM | 150 | 2200220 |
| 167 | Pu-239 | RM | 150 | 308220 |
| 168 | Pu-240 | SLBW | 128 | 572220 |
| 169 | Pu-242 | SLBW | 150 | 572220 |
| 170 | Am-241 | SLBW | 98 | 484220 |
| | | Total | 2223 | 6336924 |

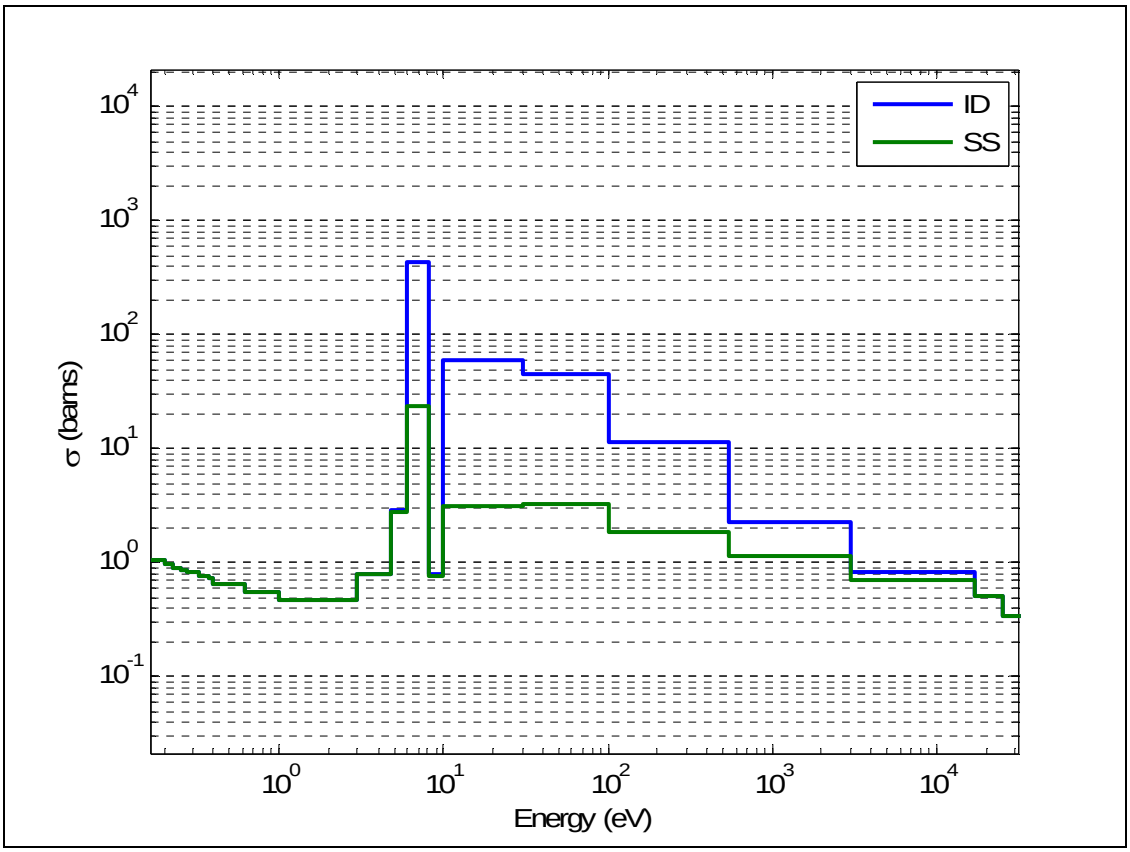


Figure 3-1 U-238 capture cross-section in the resolved resonance energy range.

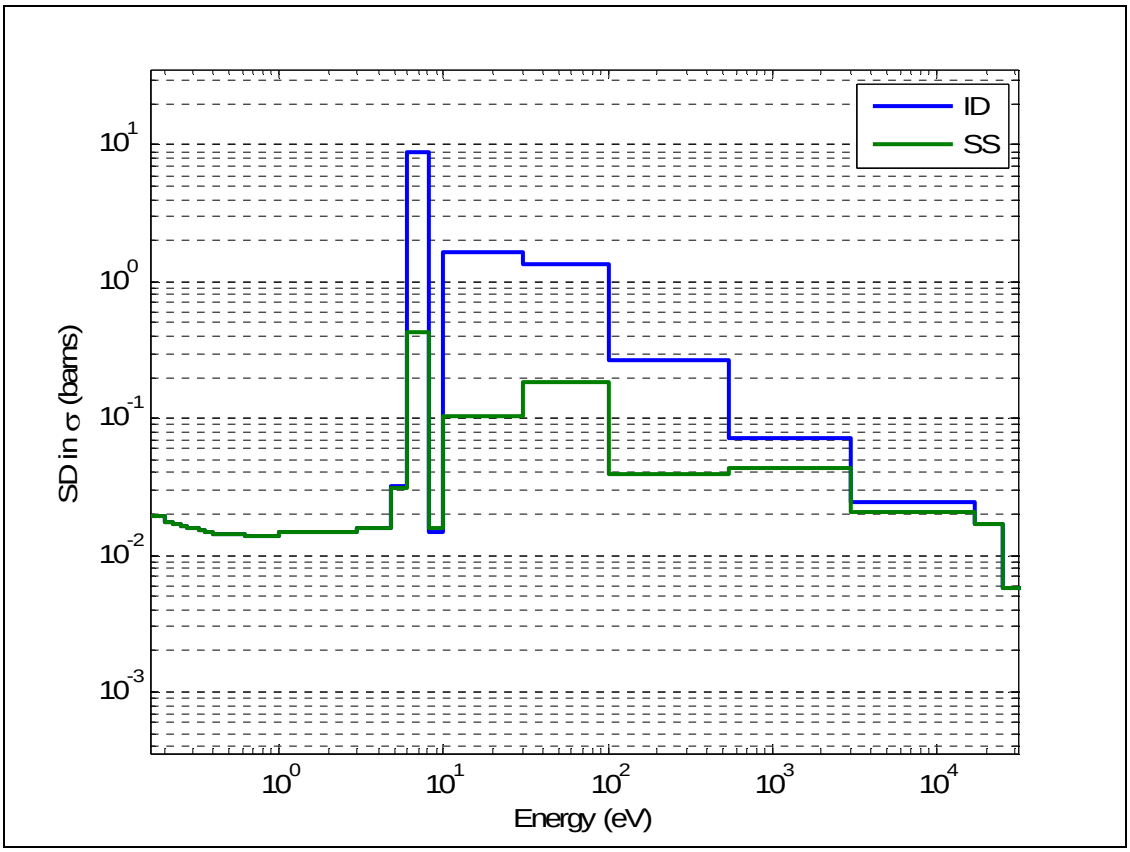


Figure 3-2 Absolute standard deviation in U-238 multi-group capture cross-section.

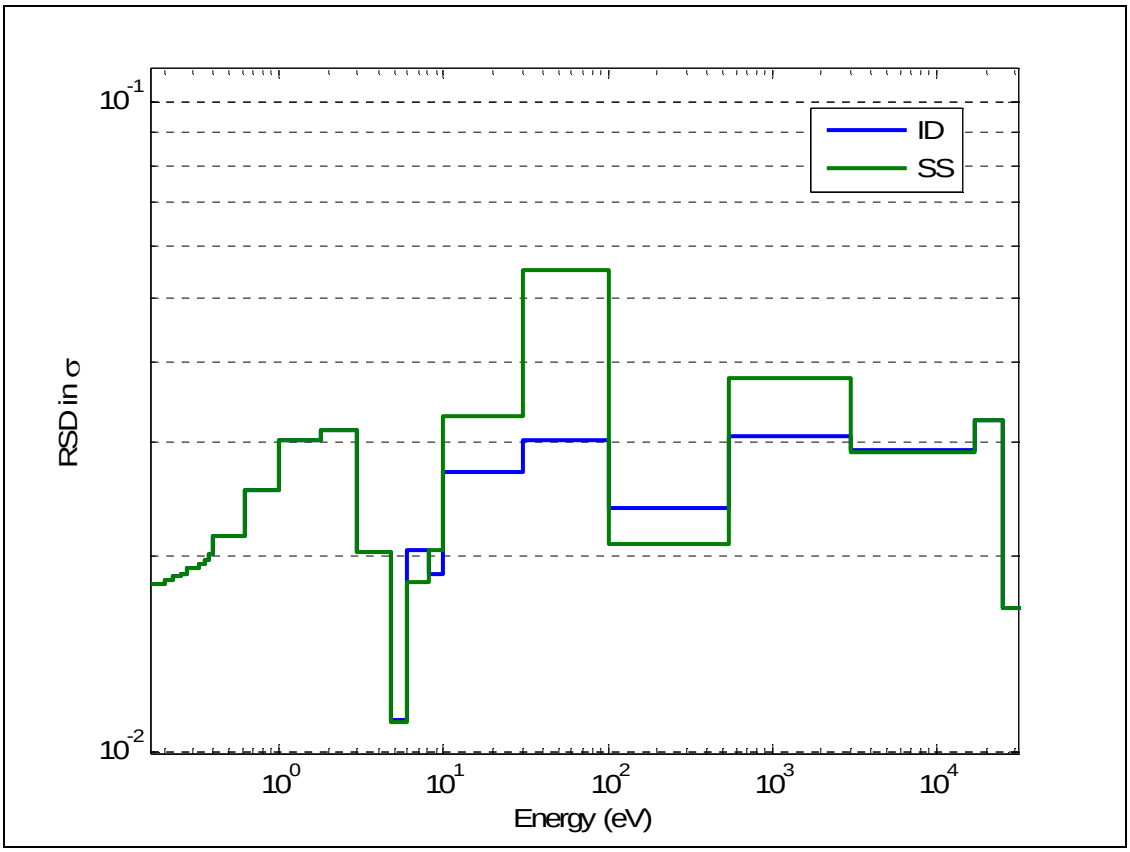


Figure 3-3 Relative standard deviation in U-238 multi-group capture cross-section.

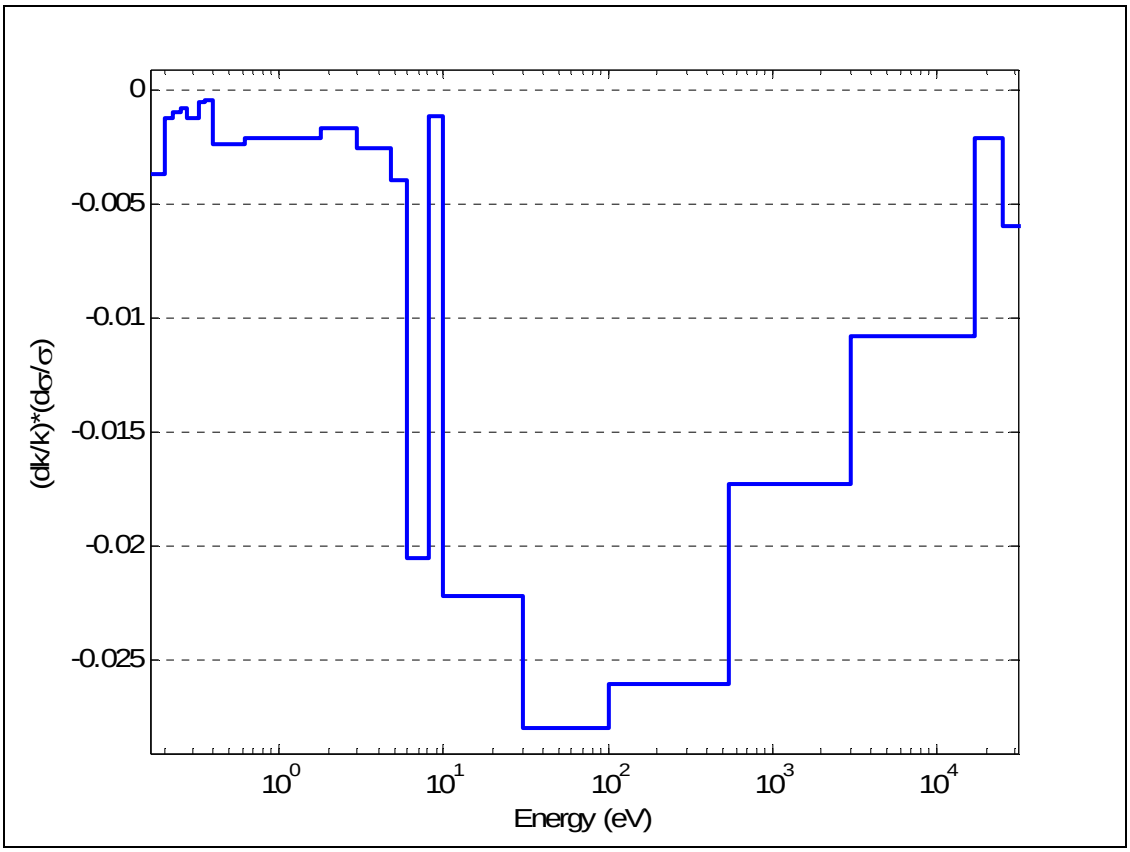


Figure 3-4 Lattice k-infinity relative sensitivity coefficient for U-238 capture multi-group cross-section.

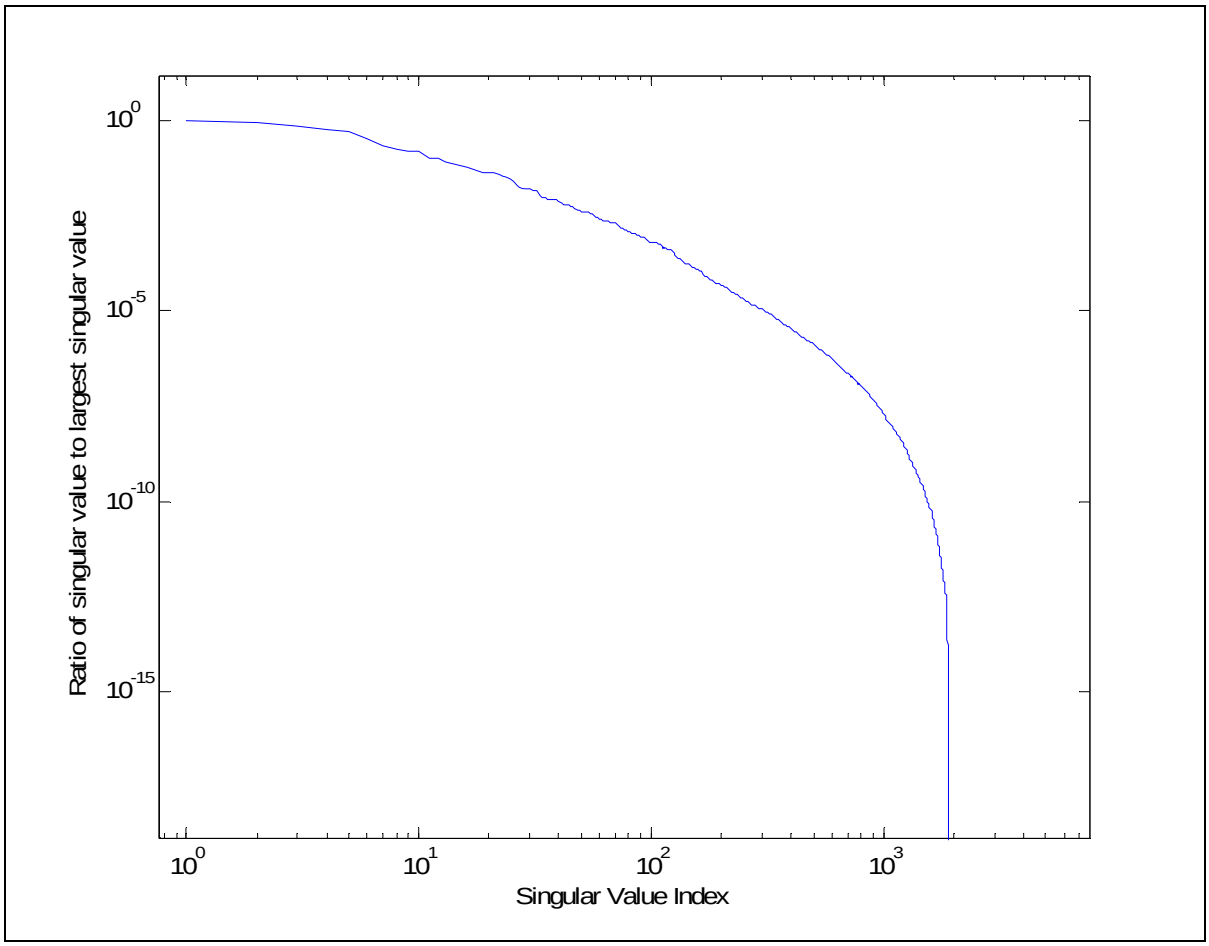


Figure 3-5 Singular values for self-shielded multi-group cross-section covariance matrix.

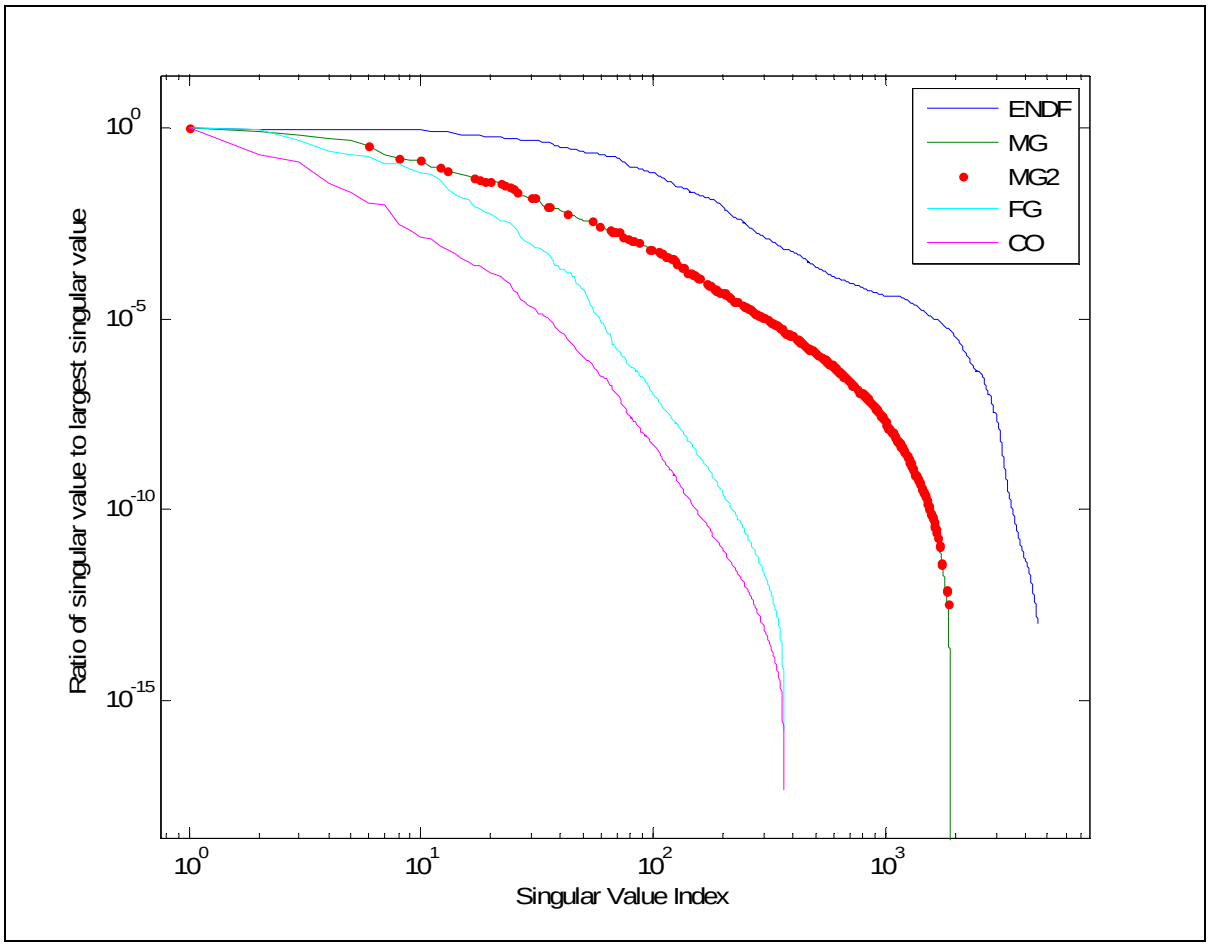


Figure 3-6 Singular values for all covariance matrices.

# 4. Results and Interpretations

## 4.1. Uncertainty Propagation

The uncertainty propagation calculations for both the lattice physics model and the core simulator are described in Chapters 2 and 3. In this section, uncertainty values are presented for lattice k-infinity and key core attributes as a result of these calculations. For the lattice physics model, uncertainties in few-group cross-sections and lattice k-infinity are computed for 10 different lattice cases. For each lattice case, cross-section perturbations are introduced in the multi-group cross-section library, which includes perturbations to the resonance correction factors in the interpolation tables used in the modified resonance self-shielding model. The cross-section perturbations are determined by the singular vectors of the self-shielded multi-group cross-section covariance matrix. After the perturbed lattice physics calculations are completed (481 for each lattice case), the standard deviation in lattice k-infinity is computed from Eq. (2.24).

In Figure 4-1, the relative standard deviation (RSD) in lattice k-infinity is given as a function of burnup for a vanished lattice depleted at 80% nominal void fraction. In addition to the total standard deviation, the standard deviation is subdivided into contributions from different isotopes. Isotopic contributions to k-infinity uncertainty are provided for 1) U-235, 2) U-238, 3) Gd-155 and Gd-157, and 4) Pu and minor actinide isotopes. (Note that the total RSD is equal to the square root of the sum of the squares of each isotope's RSD). At zero burnup (i.e. – BOL), the total standard deviation is 0.57%, and U-235 and U-238 cross-section uncertainties are the major contributors to the total uncertainty. This is attributed to

two different effects. First, large k-infinity sensitivity coefficients to U-235 and U-238 capture and fission cross-sections exist even though the cross-section uncertainties for these reaction types are small (i.e. – less than two percent) in the thermal and resolved resonance energy region. Second, the U-238 inelastic scattering cross-section uncertainty is greater than twenty percent, which is large enough to significantly contribute to k-infinity uncertainty even though the k-infinity sensitivity coefficient to the U-238 inelastic scattering cross-section is small. In addition, the BOL k-infinity uncertainty due to Gd-155 and Gd-157 is 0.12%. Since Gd-155 and Gd-157 are strong thermal neutron absorbers, gadolinium is used as a burnable poison to hold down hot excess reactivity at low burnup. The uncertainty in k-infinity due to these gadolinium isotopes is attributed to large k-infinity sensitivity coefficients to the Gd-155 and Gd-157 capture cross-sections in the thermal energy region. Because the BOL number density of Pu and minor actinides is zero, their cross-sections uncertainties do not contribute to the uncertainty in BOL k-infinity.

As the lattice is depleted, there are many nuclide transmutation effects that influence k-infinity uncertainty. First, the U-235 cross-section uncertainty contribution decreases with burnup since the U-235 number density (i.e. – sensitivity) decreases with burnup. Likewise, the Gd cross-section uncertainty contribution decreases to zero as the Gd-155 and Gd-157 number densities decrease to zero. Since Pu and minor actinides number densities increase with burnup, their cross-section uncertainties increase the k-infinity uncertainty as function of burnup. The U-238 cross-section uncertainty contribution is rather constant with burnup (0.40% RSD in k-infinity at BOL, 0.36% at 16 Gigawatt-days per metric-tonne-U (GWD/MTU), and 0.41% at EOL) since the number density of U-238 does not significantly

decrease with burnup. In addition to these general trends in number density buildup and depletion, perturbations in U-238 and gadolinium cross-sections significantly influence the k-infinity curve before the gadolinium peak, which is the burnup value at which the positive fuel reactive worth offsets the negative gadolinium or BP reactivity worth. For this lattice, the gadolinium peak occurs at 19 GWD/MTU. Before the gadolinium peak, the nonlinear curvature in the k-infinity uncertainty is influenced by many competing reactivity effects such as resonance and spatial self-shielding, spatially-dependent gadolinium depletion, and spatially dependent Pu buildup.

As for other lattices cases, the k-infinity uncertainty is similar to that given in Figure 4-1, such as the k-infinity uncertainty for a dominant lattice depleted at 40% nominal void fraction in Figure 4-2. The Gd-155 and Gd-157 uncertainty contribution is lower at BOL for the dominant lattice modeled at 40% nominal void fraction compared to the vanished lattice modeled at 80% nominal void fraction. Since there are more fuel rods in the dominate lattice as compared to the vanished lattice, the gadolinium neutron absorption rate decreases. This leads to smaller k-infinity sensitivity coefficients to gadolinium cross-sections for the dominant lattice, which in turn leads to a smaller gadolinium uncertainty contribution.

Similar to lattice k-infinity uncertainty, uncertainties in key core attributes are calculated by propagating cross-section uncertainty through the core simulator model. For this work, the FORMOSA-B core simulator is used to model a GE BWR/4 core design with 560 fuel assemblies. The core model consists of 36 burnup steps with an End-of-Cycle (EOC) burnup of 19948.3 GWD/MTU. The FORMOSA-B core simulator uses few-group cross-sections generated by the CASMO-3 lattice physics code [52]. Since the CASMO-3

lattice physics code was unavailable for this work, TRITON was used to generate the few-group cross-section covariance matrix. However, the calculation methods employed by the CAMSO-3 lattice physics code are considerably different than that of the TRITON lattice physics code. This difference in methodology leads to small differences in the nominal few-group cross-section values. Similar to previous work, it is assumed that the relative few-group cross-section covariance matrix generated by the TRITON lattice physics code is equal to the relative few-group cross-section covariance matrix as would be calculated by the CASMO-3 code. This is a reasonable assumption since the concern here is accurately approximating the relative change in few-group cross-sections with respect to multi-group cross-section perturbations, which is less difficult than accurately predicting the nominal values of the few-group cross-sections.

To calculate core attribute uncertainties, the CASMO-3 few-group cross-sections are perturbed based on the singular vectors of the few-group cross-section covariance matrix generated by TRITON. Core simulator calculations are completed for each perturbed few-group cross-section library (362 total), and the uncertainty in key core attributes are computed using Eq. (2.28). Figure 4-3 graphs the core k-effective RSD as a function of burnup. The total core k-effective is subdivided into isotopic contributions similar to the lattice k-infinity uncertainties in Figure 4-1 and Figure 4-2. The RSD in k-effective is 0.56% at BOC and increases to 0.63% at EOC. The k-effective uncertainty is dominated by U-238 cross-section uncertainty at BOC and by plutonium and minor actinide cross-section uncertainty at EOC. The two main differences between core k-effective uncertainty and lattice k-infinity uncertainty are 1) the non-zero plutonium and minor actinide uncertainty

contribution at BOC, and 2) the decrease in U-235 and gadolinium cross-section uncertainty contribution. These effects are due to the reuse of once-burned and twice-burned fuel assemblies in a checkerboard fuel assembly loading pattern (LP). Consequently, the checkerboard LP tends to smooth out the k-effective uncertainty as a function of burnup.

In Figure 4-4, the standard deviation in nodal power at BOC is given as a function of axial position for a fresh fuel located near the center of the core. Similar profiles are given in Figure 4-5 at Middle-of-Cycle (MOC) and in Figure 4-6 at EOC. The nodal power uncertainty profiles are given in terms of the absolute standard deviation rather than RSD because the low-power axial blanket nodes (i.e. - nodes 1 and 25) have high relative standard deviations that graphically distort the measure of uncertainty in the high-power interior nodes. There are several reasons for the complex shape in the nodal power uncertainty profiles. First, the node-dependent few-group cross-sections and their uncertainties may differ due to changes in lattice design. The lattice design changes in nodes 1, 15, 25, and possibly node 10 if power-shaping BP rods are present in the fuel assembly. Second, the few-group cross-sections vary due to different local thermal hydraulics conditions and exposure history. Finally, several nodal power uncertainty profiles exhibit a “double hump” because of a change in sign of the nodal power sensitivity coefficients moving from the bottom node to the top node. For example, U-238 capture cross-section perturbations tend to shift the relative nodal power towards the bottom or the top of the fuel assembly, depending on the direction of the cross-section perturbation. This leads to a positive sensitivity coefficient at the bottom of the fuel assembly and a negative sensitivity coefficient at the top of the fuel assembly (or

vice versa). The double hump effect occurs by calculating the square root of the sum of the squares of the sensitivity profile.

In addition to nodal power uncertainties, Figure 4-7 – Figure 4-9 graphs the uncertainty in thermal margins. The Average Linear Power Density Ratio (APRAT) uncertainty is given in Figure 4-7 for the same fuel assembly in the nodal power uncertainty figures. The APRAT ratio represents to the approach to limiting Average Planar Linear Heat Generation Rate (APLHGR). This thermal limit is determined by the maximum peak clad temperature during a Loss of Cooling Accident (LOCA). Similar to the APRAT margin, Figure 4-8 graphs the fraction to limiting power density (FLPD) margin and its standard deviation. The FLPD margin corresponds to the thermal limit on pin-wise linear heat generation rates due to pellet-clad interaction. Both the APRAT and FLPD margin uncertainties are highly correlated to the uncertainties in nodal power. In addition to these thermal margins, the uncertainty in Maximum Fraction to Limiting Critical Power Ratio (MFLCPR) is given in Figure 4-9. The MFLCPR thermal margin represents the approach to the critical heat flux limit, and is also highly correlated to the nodal power uncertainty. The MFLCPR thermal margin uncertainties are also dependent upon the axially integrated power uncertainty as a function of elevation via the critical heat flux correlation dependence on coolant quality.

## 4.2. BWR Adaptive Simulation

The quantified uncertainties in BWR core observables can be used as a basis for self-shielded multi-group cross-section adjustment to improve BWR modeling fidelity. To

display this capability, the virtual approach is employed as described in the previous work by Abdel-Khalik in [1] and [2]. For the virtual approach, the design basis core simulator, denoted DC, is adapted to a set of virtual core observables, denoted VC. The VC nodal power distributions and core k-effective are used to represent the measured core observables rather than LRPM/TIP detector readings and core k-effective equal to one. This is a valid assumption because the LPRM/TIP detector readings' prediction uncertainties are highly correlated to the nodal power prediction uncertainties.[1] For the rest of this work, the core nodal power distribution is referred to as a core observable rather than a core attribute.

The VC core observables are generated by perturbing the self-shielded multi-group cross-sections in a statistically consistent manner with their prior uncertainties. Specifically, the VC core observables, denoted $\bar{y}_{CO_m}$, are calculated according to:

$$\bar{y}_{CO_m} = \bar{\mathbf{\Theta}}_{CS}(\bar{\mathbf{\Theta}}_{LP}(\bar{x}_{MG_0} + \bar{\bar{\mathbf{U}}}_{MG,t}\,\bar{\bar{\mathbf{\Sigma}}}^{1/2}_{MG,t}\,\bar{z}_{MG,t})) + \bar{\eta}_{noise} \tag{4.1}$$

where $\bar{z}_{MG,t}$ is the perturbation to the prior self-shielded multi-group cross-sections, and $\bar{\eta}_{noise}$ is the noise applied to the VC nodal power distributions. In the first adaption experiment presented (i.e. – Case A), the perturbations in $\bar{z}_{MG,t}$ are stochastically sampled from a normal probability density function with a mean value of zero and a standard deviation of one. To create the VC, each of the 2223 singular vectors are stochastically sampled while only 481 singular vectors are used to adjust the multi-group cross-sections of

[1] For future work, the LPRM/TIP detector readings' uncertainties will be directly evaluated using a realistic core simulator's detector model.

the DC. The selected subspace of the self-shielded multi-group cross-section singular vectors is determined by the GPT sensitivity analysis outlined in Chapter 3. The noise vector is determined by stochastic sampling from a Gaussian distribution with of mean value of zero and a standard deviation of 0.04. This is representative of the noise level in the LPRM detector readings.

Figure 4-10 plots the prior and posterior error in k-effective for Case A as a function of burnup. In Figure 4-11, the nodal power RMS error is given as a function of burnup. The core k-effective error before the adaption (i.e. - <DC/VC> in Figure 4-10) is 550 pcm at BOC and increases to 1200 pcm at EOC. After the cross-section adjustment, the core-k-effective error, denoted <AC/DC>, deceases to a value less than 100 pcm. The posterior error in k-effective is of the same order of magnitude as the linearization error for the lattice physics and core simulator models in assuming that changes in observables respond linearly to cross-section perturbations for each model. In Figure 4-11, the prior and posterior nodal power RMS error is denoted <DC/VC> and <AC/VC> respectively. The prior error is slightly larger than the noise level in simulated VC core observables' measurements. The posterior error is essentially equal to the 4% noise in the VC core observables' measurements. Removing the noise component from the nodal power distribution, the prior and posterior errors are given as <DC/VC*> and <AC/VC*>, respectively. The posterior error is less than 0.5% as a function of burnup as compared to the 1.0-1.3% nodal power error before the adaption. This shows that the cross-section adjustment acts as a powerful noise filter. For this case, the prior nodal power RMS is somewhat smaller than the expected error in LPRM detector readings. The Tikhonov regularization parameter is therefore set to

1.0. In other words, equal weighting is given to the misfit chi-square $\chi_m^2$ and the regularization chi-square $\chi_r^2$. The formulas for $\chi_m^2$ and $\chi_r^2$ are extracted from Eq. (2.35) as:

$$\chi_m^2 = \left\| (\bar{y}_{CO_m} - \bar{y}_{CO_0}) - \bar{\bar{\mathbf{S}}}_{CS} \bar{\bar{\mathbf{S}}}_{LP} (\bar{x}_{MG} - \bar{x}_{MG_0}) \right\|^2_{\bar{\bar{\mathbf{C}}}^{\dagger}_{CO_m}}$$
$$\chi_r^2 = \left\| \bar{x}_{MG} - \bar{x}_{MG_0} \right\|^2_{\bar{\bar{\mathbf{C}}}^{\dagger}_{MG}} \tag{4.2}$$

For Case A, $\chi_r^2$ is equal to 5.645, which implies the self-shielded multi-group cross-sections are perturbed with an RMS of 0.11 standard deviations.

For the second adaption experiment (i.e. – Case B), $\bar{z}_{MG,t}$ is determined using a different stochastic sample with a mean value of zero and a standard deviation of 2.5. The standard deviation was increased so that the nodal power RMS errors is more comparable with the errors of measured LPRM detector readings.

Figure 4-12 plots the prior and posterior error in k-effective for Case B as a function of burnup. Before the adaption, the DC core k-effective error ranges from 1000 pcm at BOC to 2500 pcm at EOC. Like the Case A experiment, the absolute error in the AC core k-effective is below 250 pcm. The nodal power RMS error is given as a function of burnup in Figure 4-13. The DC nodal power RMS error ranges from 4.2% to 5.5% and the AC nodal power error is equal to the 4% noise level in the VC core observables' measurements. In addition to the nominal values of the posterior core observables, the posterior core observables uncertainties have been quantified using Eq. (2.43). The posterior standard deviation in k-

effective is less than 250 pcm, which is a substantial decrease from the 550-600 pcm prior standard deviation. The decrease in the posterior standard deviation for nodal power, APRAT, FLPD, and MFLCPR is of the same order of magnitude as the decrease in the nodal power RMS error. Because the thermal margin uncertainties are highly correlated to the uncertainties in nodal powers, their uncertainties can be significantly reduced even though they cannot be directly measured. The decrease uncertainty in thermal margins can be used to change operational strategies for the current fuel cycle and the design of future fuel cycles to increase fuel utilization, minimize fuel cycle costs, and to support power uprates.

For Case B, the Tikhonov regularization parameter is selected by the L-curve approach. To generate the L-curve, self-shielded multi-group cross-sections are adjusted using fourteen different values of $\alpha^2$ ranging from $10^{-8}$ to $10^4$. In Figure 4-19, the regularization chi-square $\chi_r^2$ is plotted versus the misfit chi-square $\chi_m^2$ for each value of $\alpha^2$. At low values of $\alpha^2$, the cross-section adjustment algorithm focuses on minimizing the misfit chi-square. As $\alpha^2$ increases, the algorithm increasingly constrains the adjusted self-shielded multi-group cross-sections to their prior values, which decreases the value of the regularization chi-square. A knee-type behavior is depicted in the figure where misfit chi-square increases rapidly without any significant change in the regularization chi-square. The optimal value of the regularization parameter is chosen in the knee region where the adjusted core observables (AC) agree with the VC core observables, and the adjusted self-shielded multi-group cross-sections are closely restricted to their prior values. For Case B, $\alpha^2$ is equal to 4.0, and the self-shielded multi-group cross-sections are perturbed with an RMS of 0.163 standard deviations from their prior values.

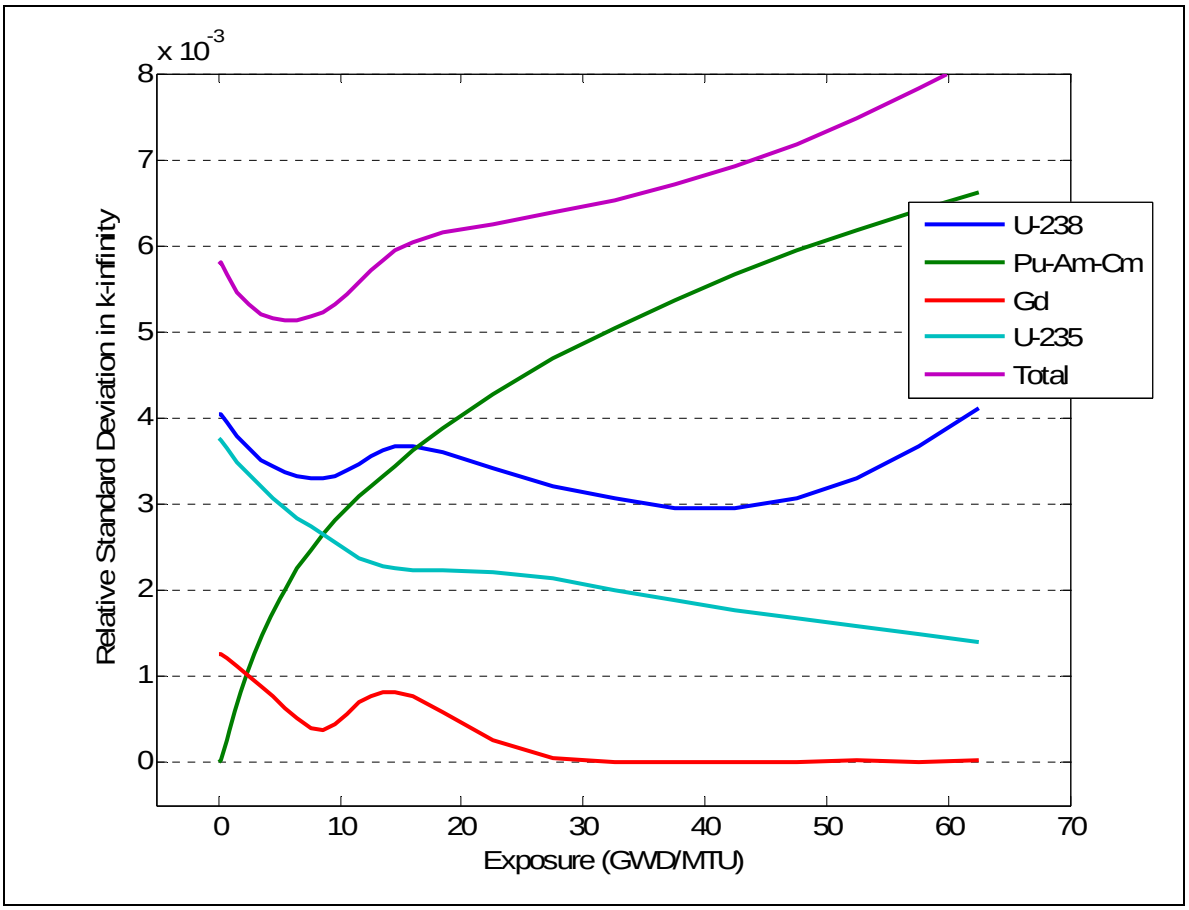


Figure 4-1 Relative standard deviation in lattice k-infinity for a vanished lattice at 80% void fraction.

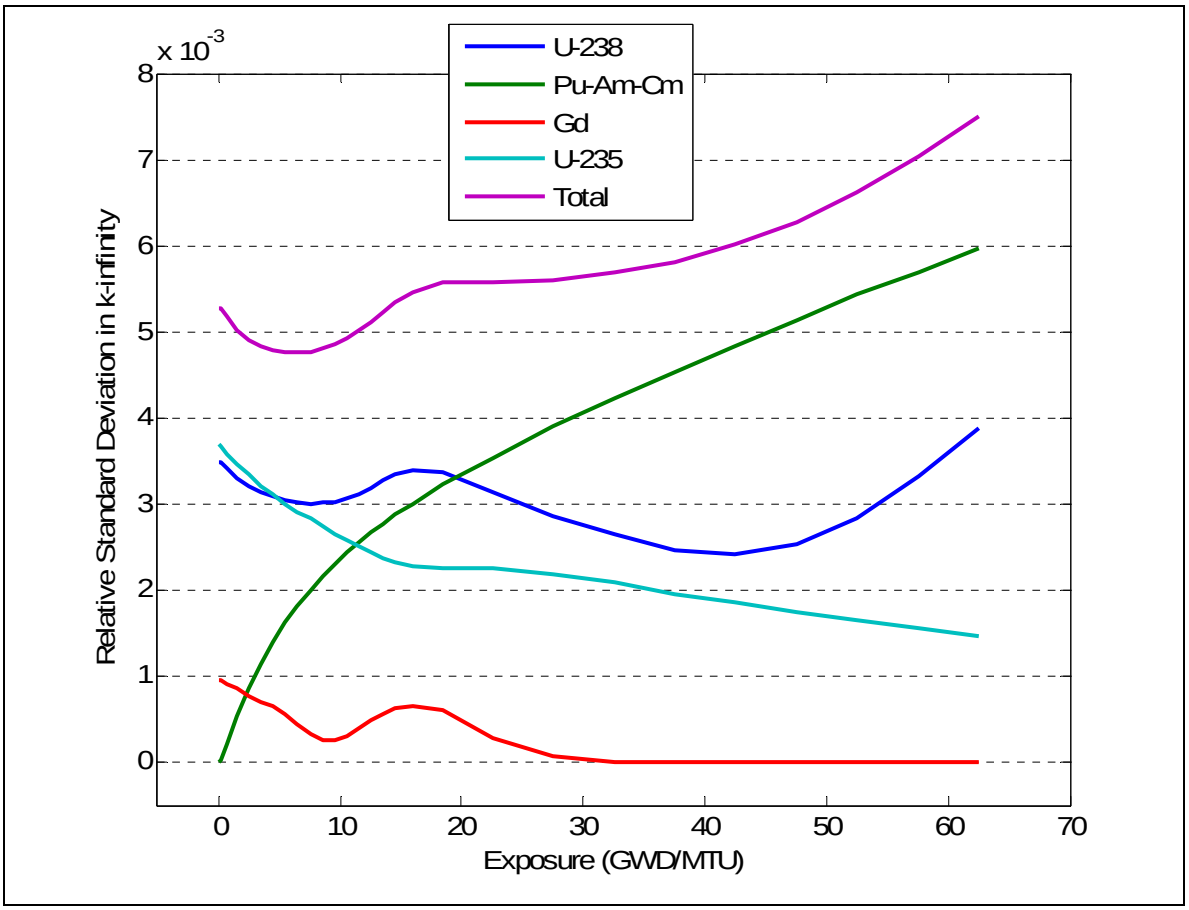


Figure 4-2 Relative standard deviation in lattice k-infinity for a dominant lattice at 40% void fraction.

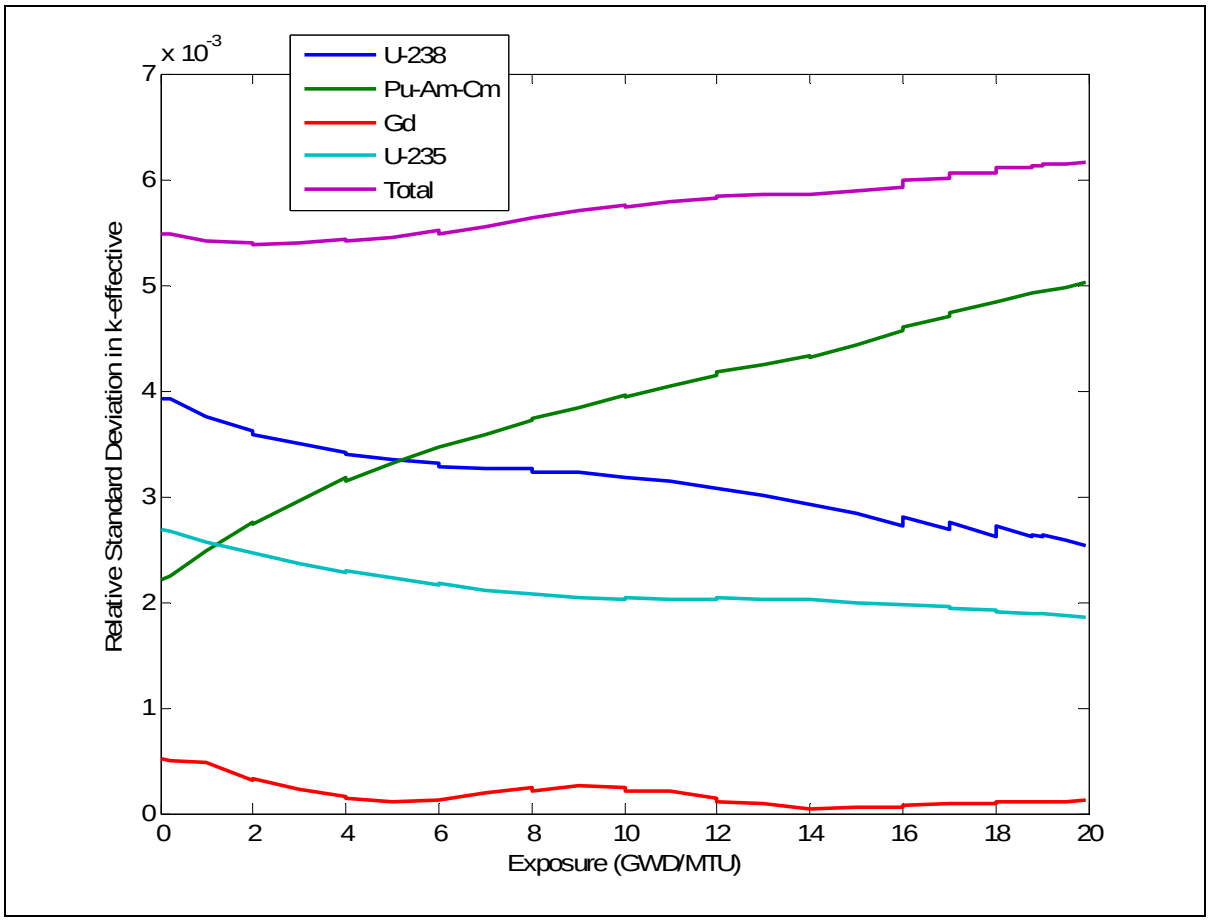


Figure 4-3 Relative standard deviation in core k-effective as a function of burnup.

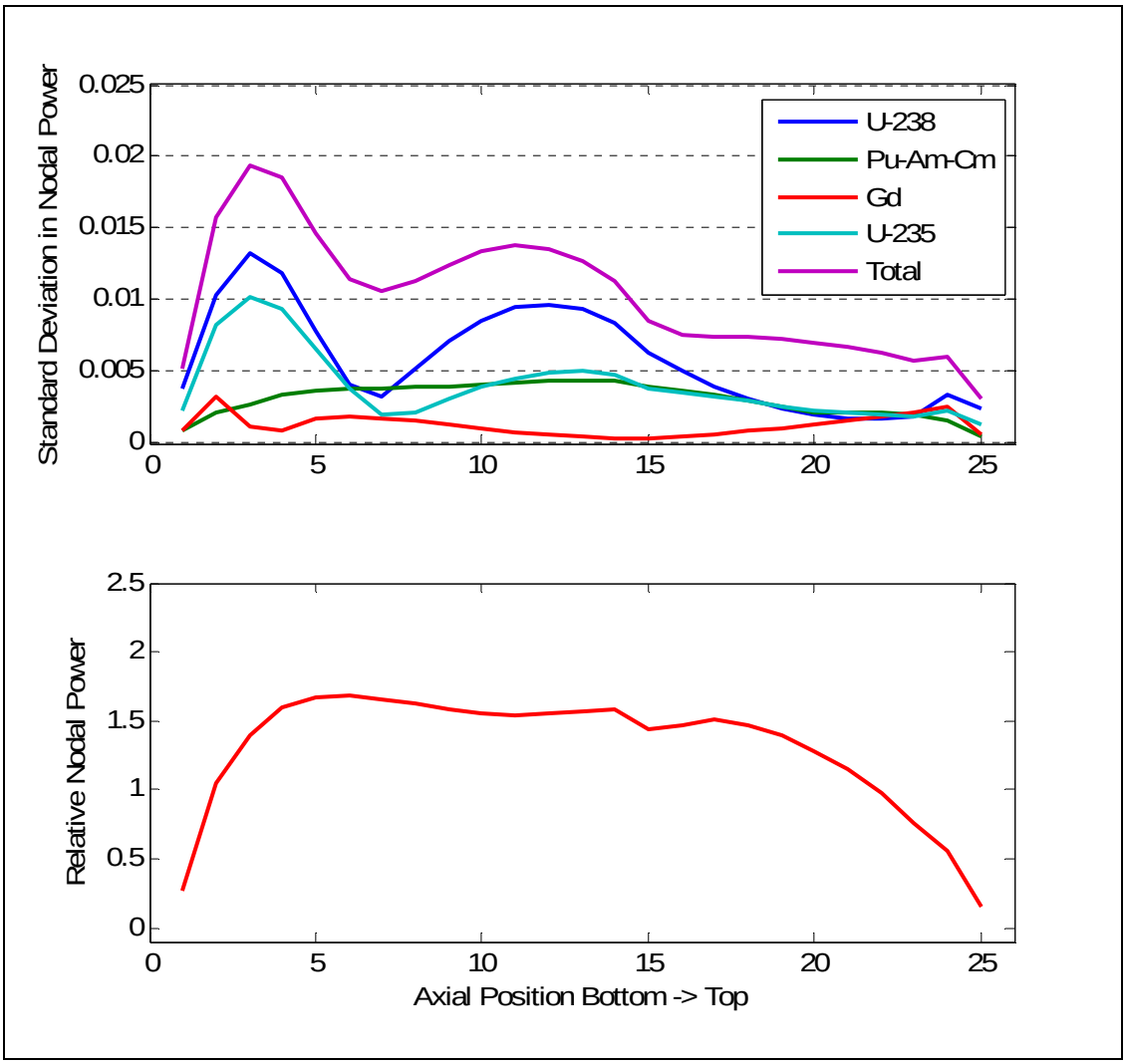


Figure 4-4 Absolute standard deviation in relative nodal power profile for a fresh fuel assembly at BOC.

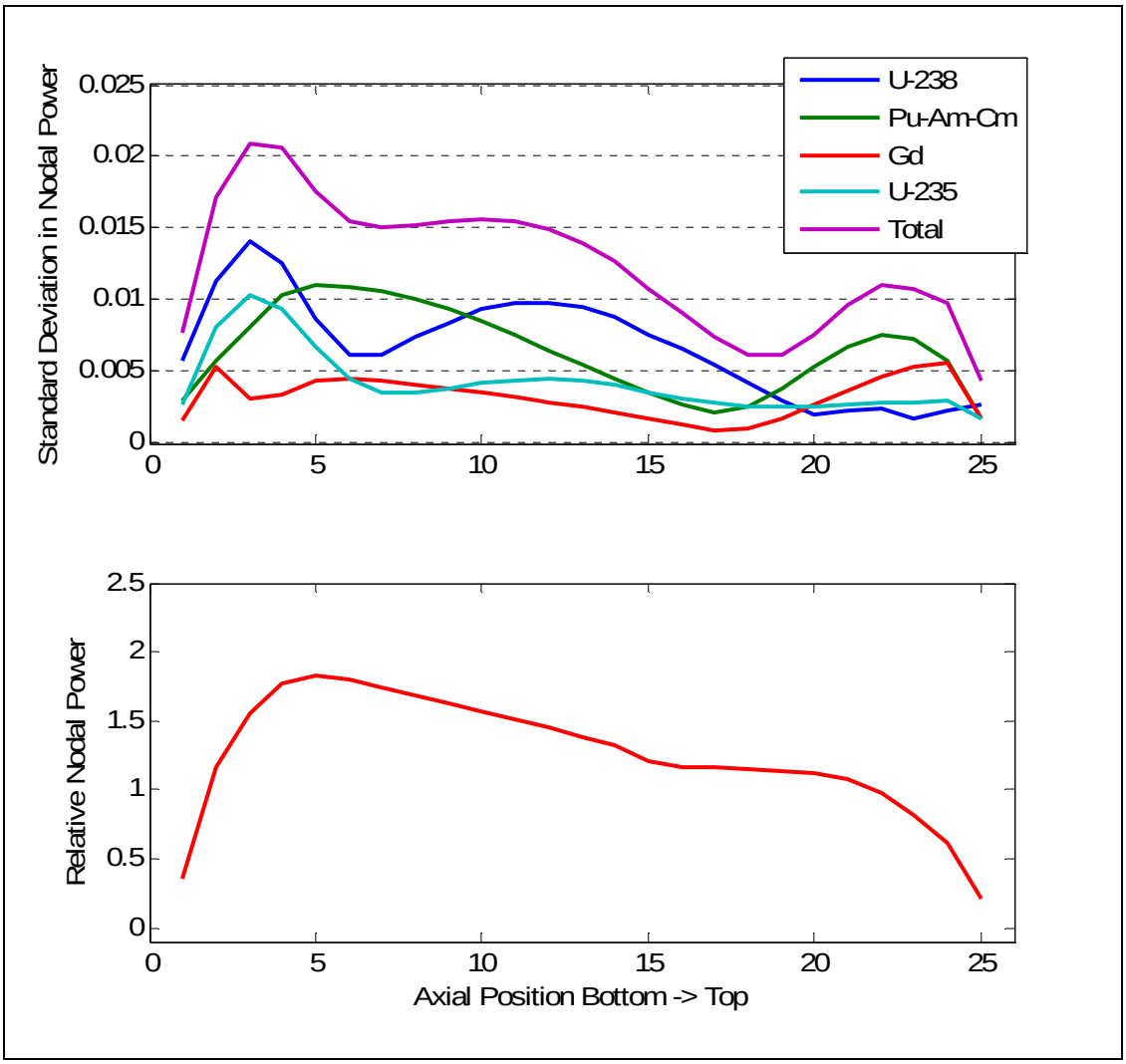


Figure 4-5 Absolute standard deviation in relative nodal power profile for a fresh fuel assembly at MOC.

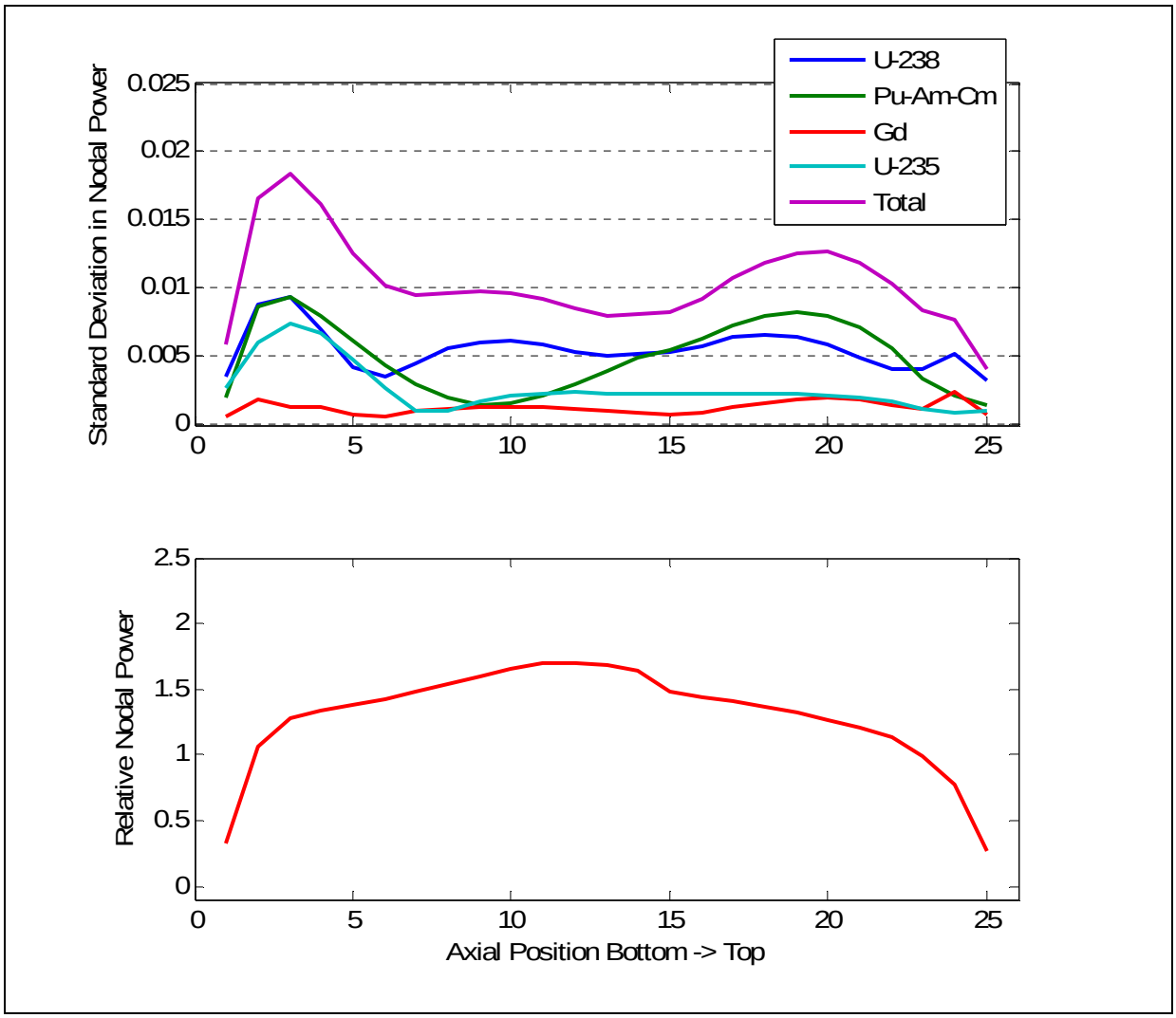


Figure 4-6 Absolute standard deviation in relative nodal power profile for a fresh fuel assembly at EOC.

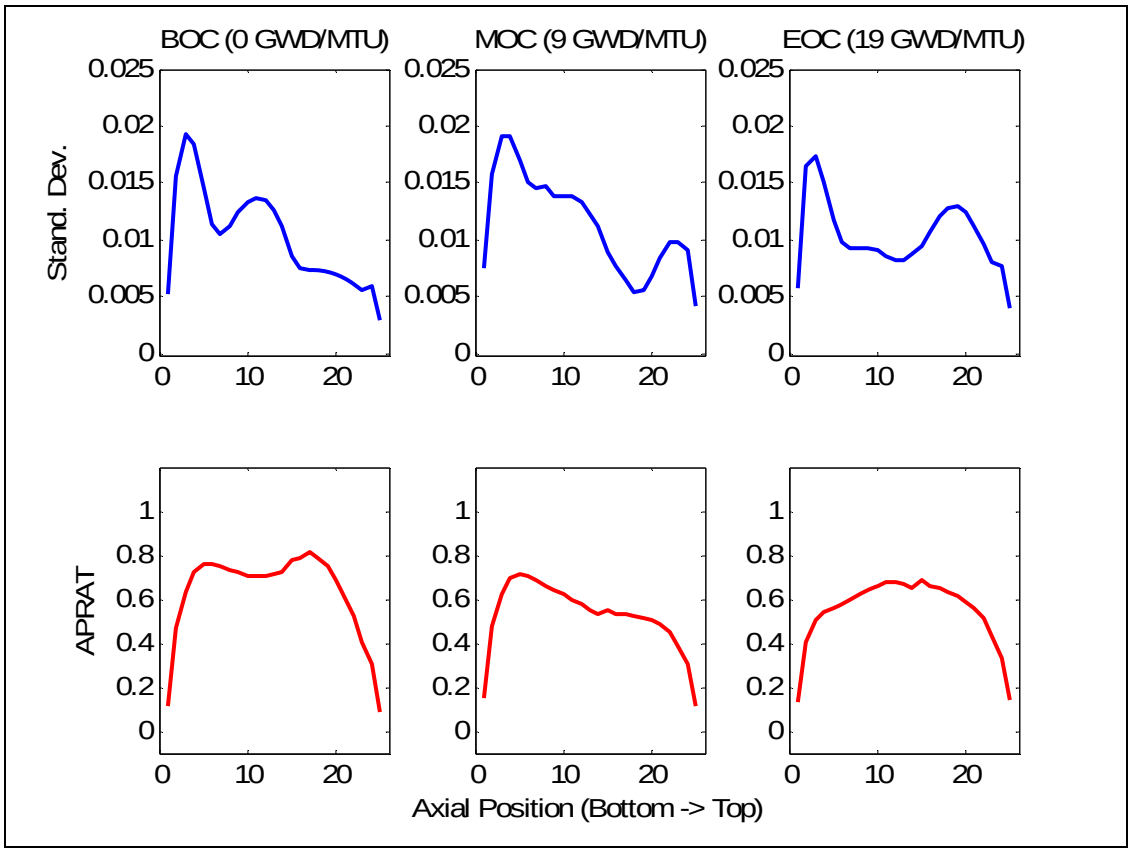


Figure 4-7 Absolute standard deviation in APRAT for a fresh fuel assembly.

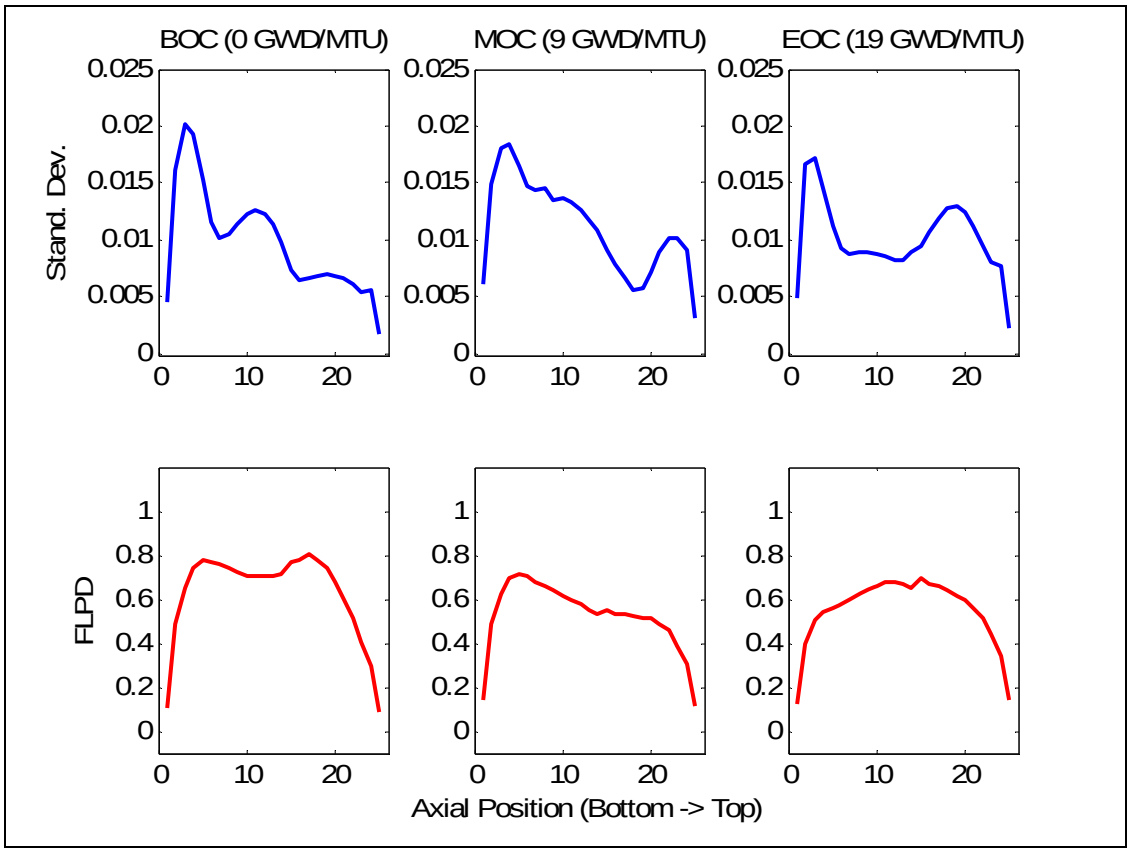


Figure 4-8 Absolute standard deviation in FLPD margin for a fresh fuel assembly.

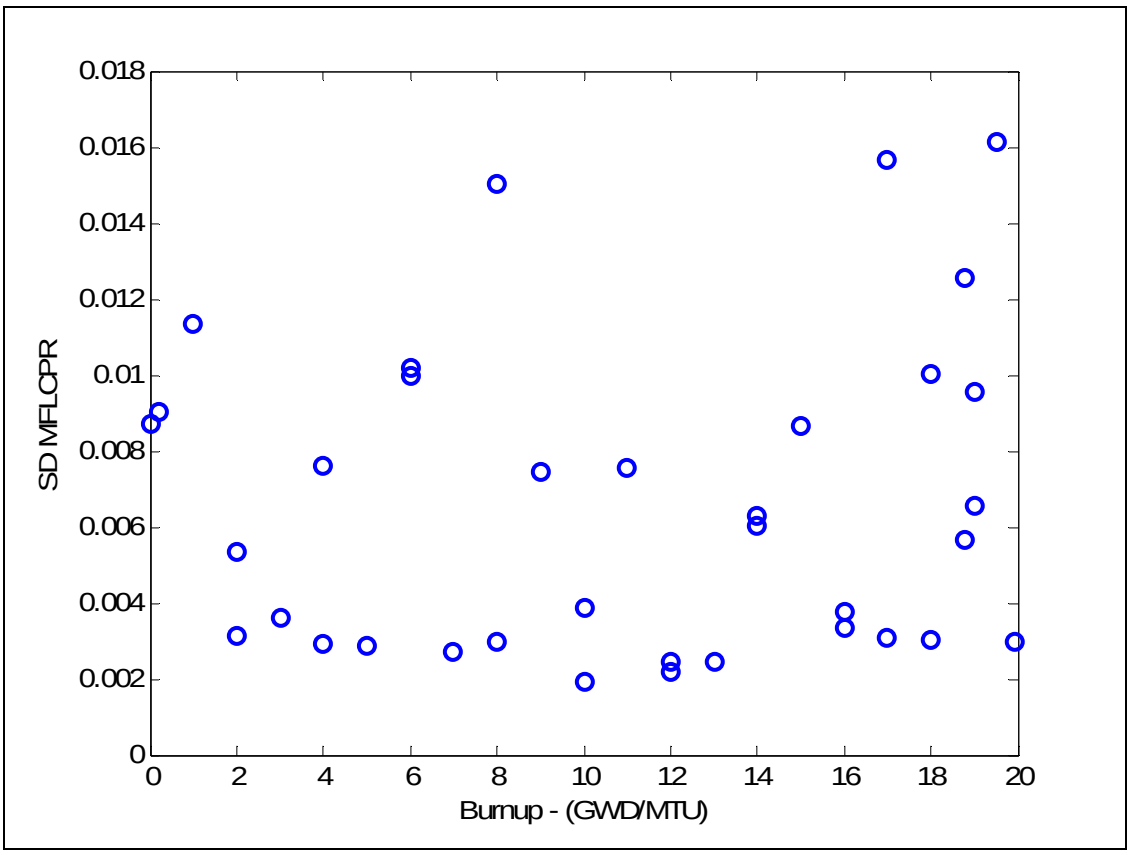


Figure 4-9 Absolute standard deviation in MFLCPR for limiting CPR fuel assembly as a function of burnup.

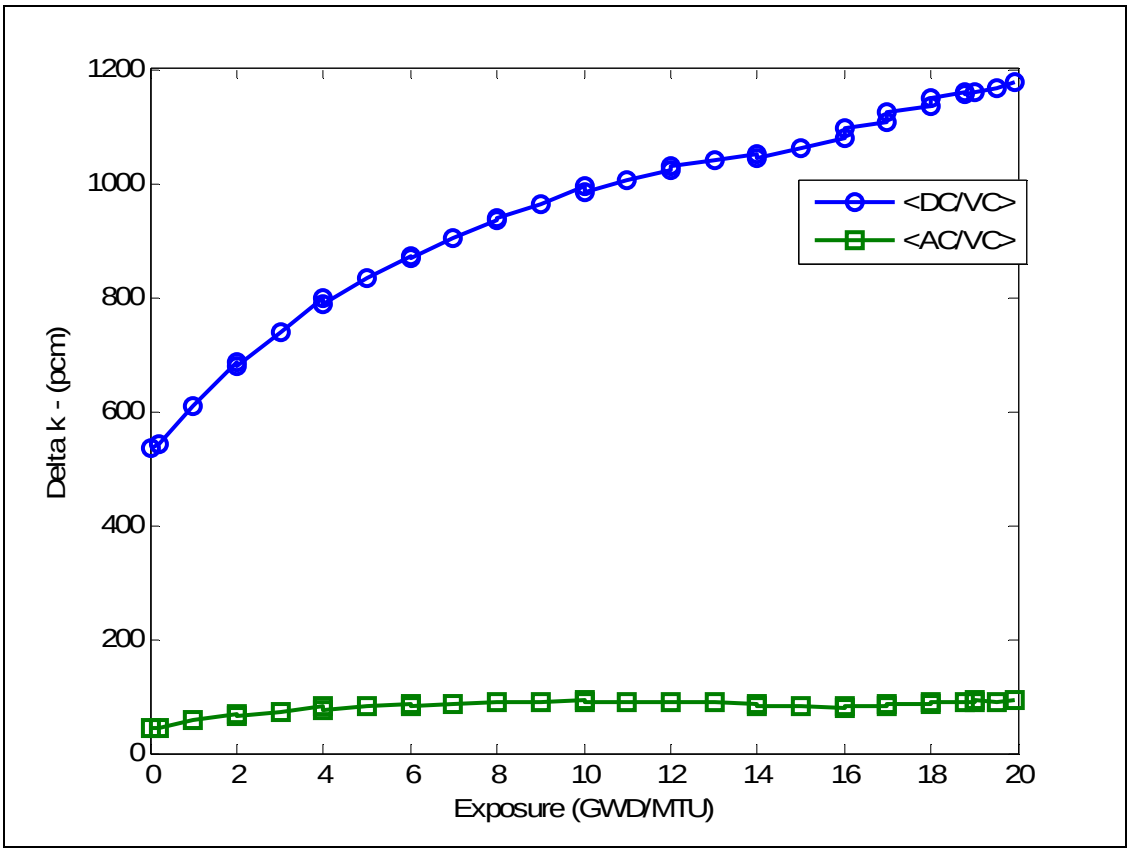


Figure 4-10 Prior and posterior error in core k-effective (Case A).

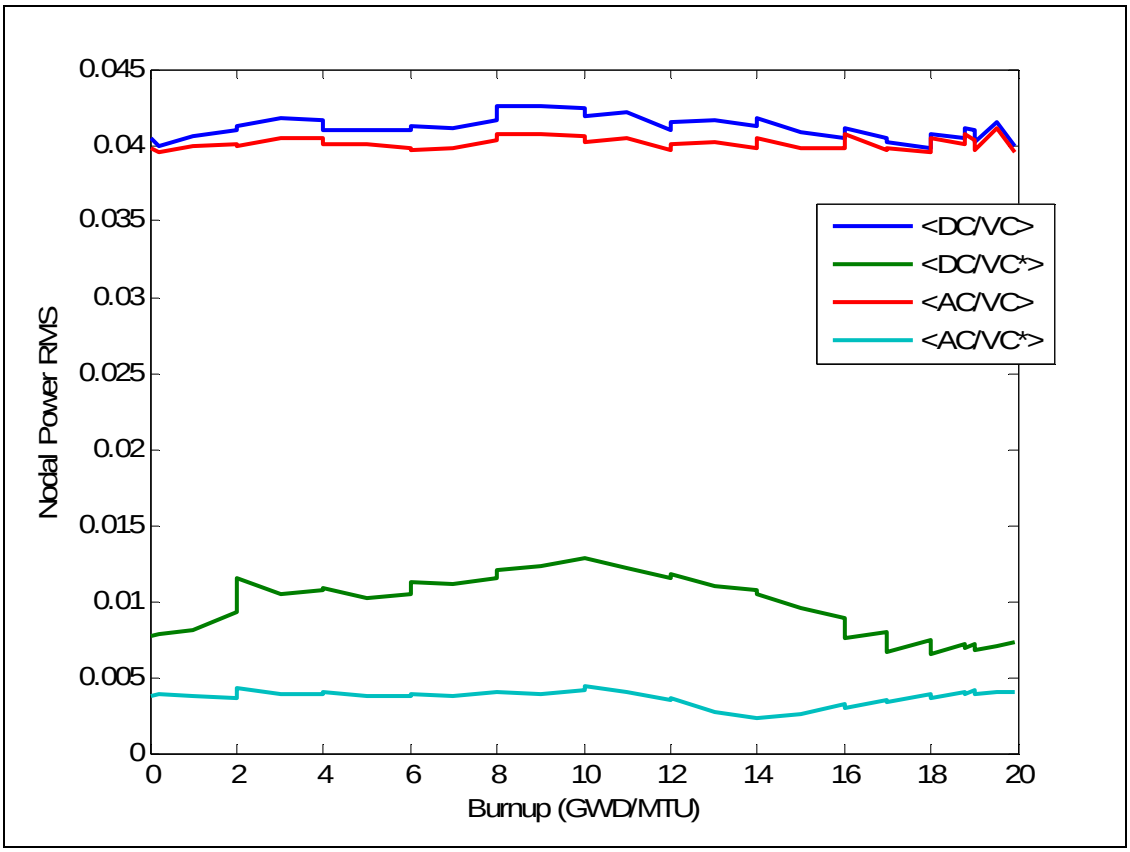


Figure 4-11 Prior and posterior core nodal power RMS error (Case A).

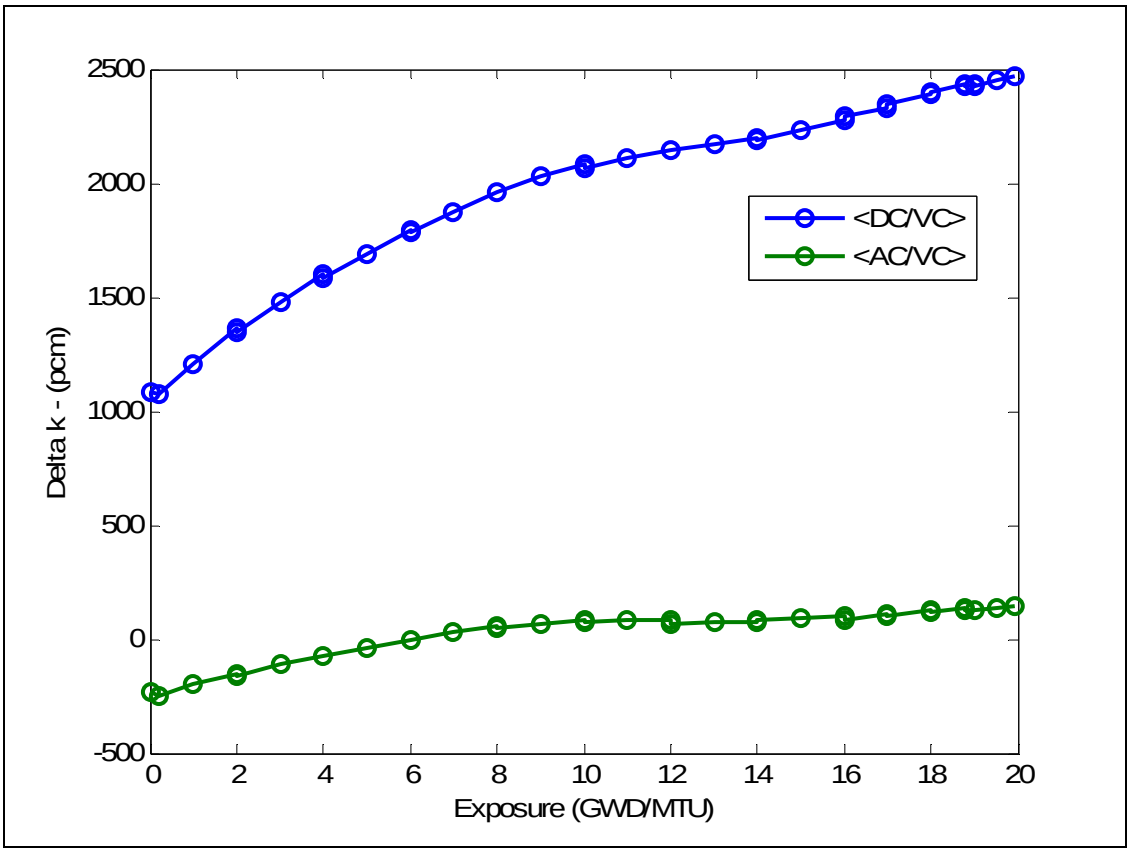


Figure 4-12 Prior and posterior error in core k-effective (Case B).

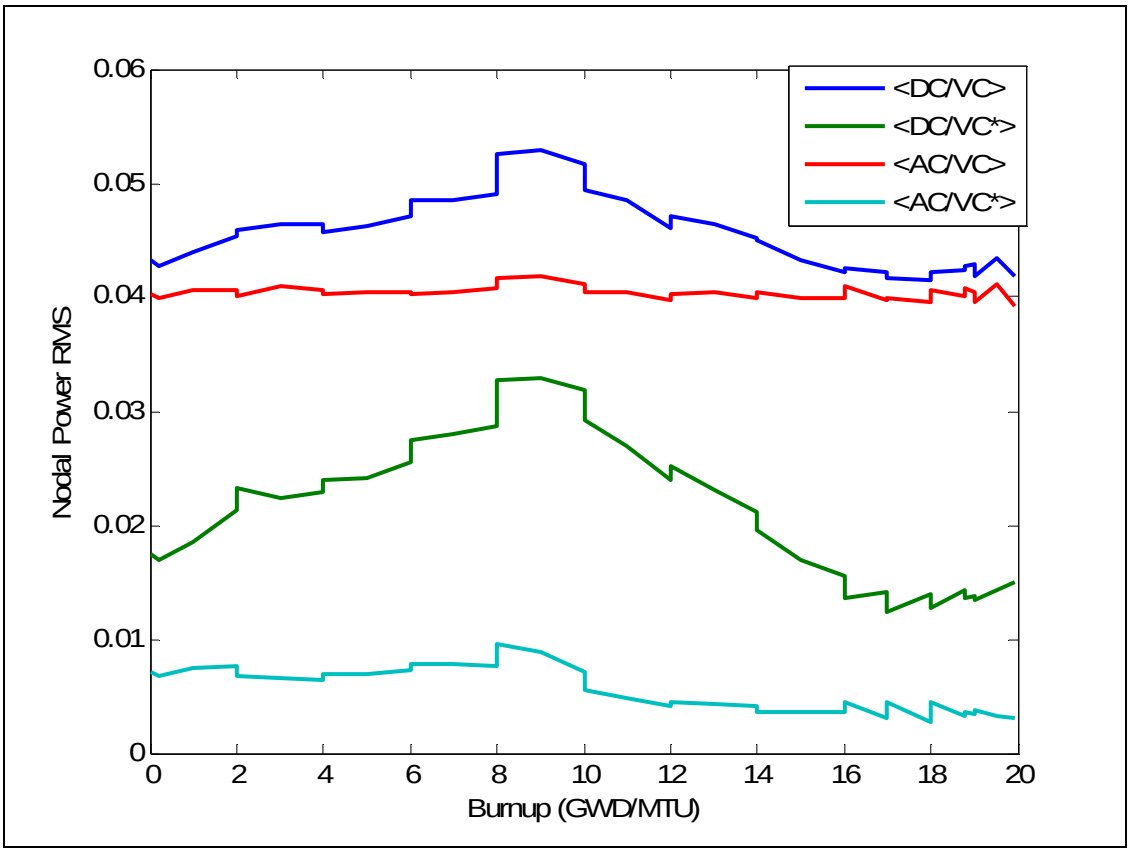


Figure 4-13 Prior and posterior core nodal power RMS error (Case B).

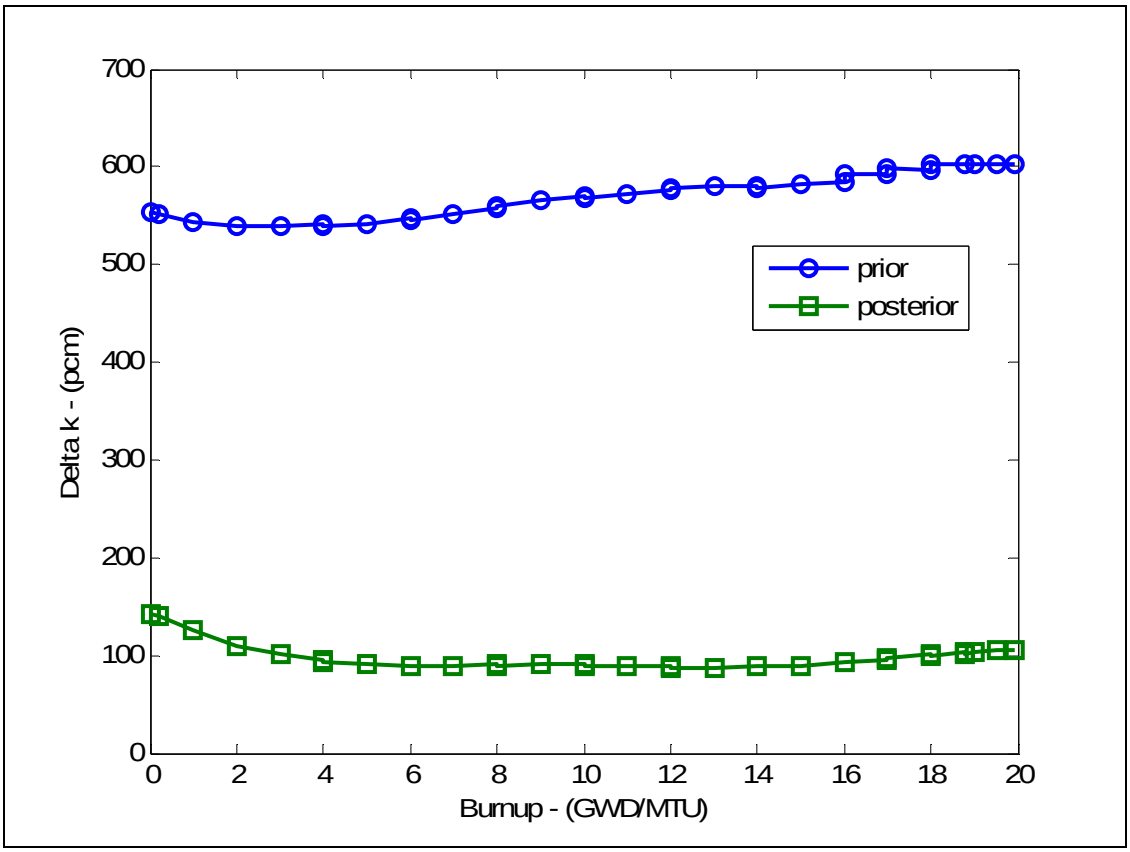


Figure 4-14 Prior and posterior absolute standard deviations in core k-effective (Case B).

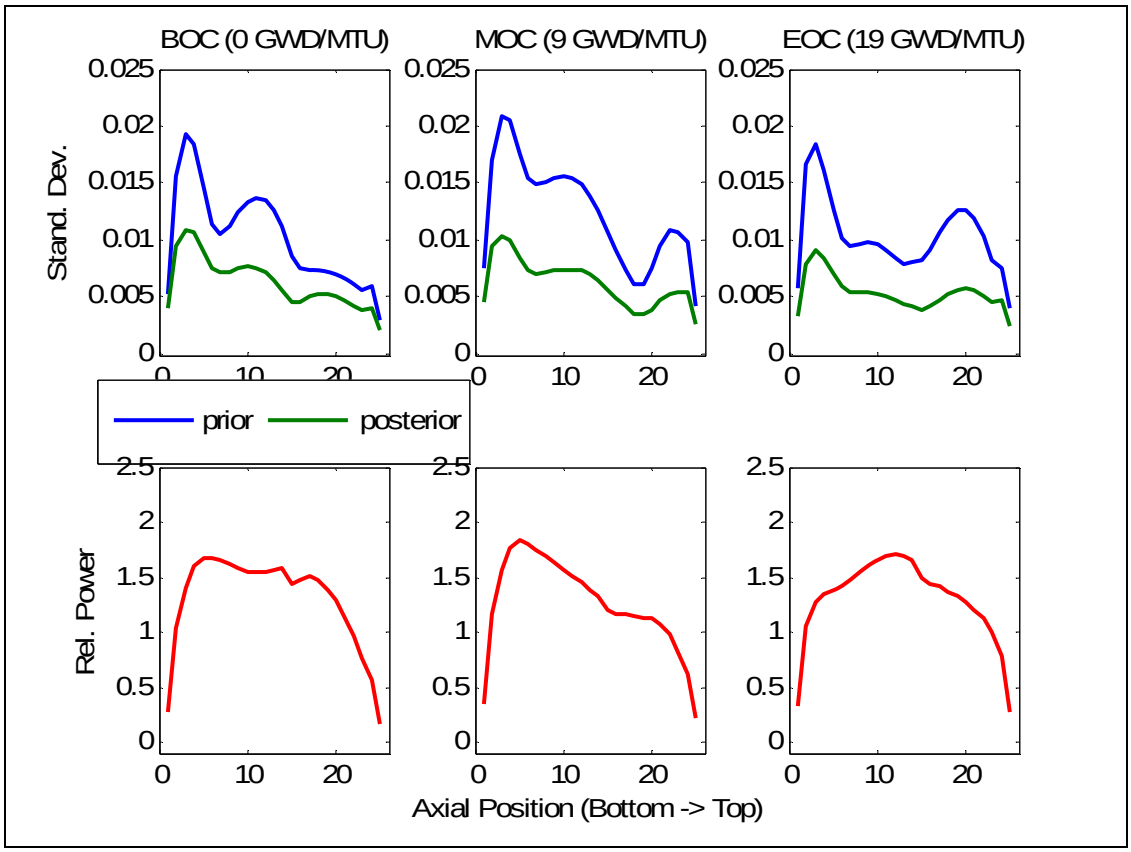


Figure 4-15 Prior and posterior absolute standard deviations in nodal power (Case B).

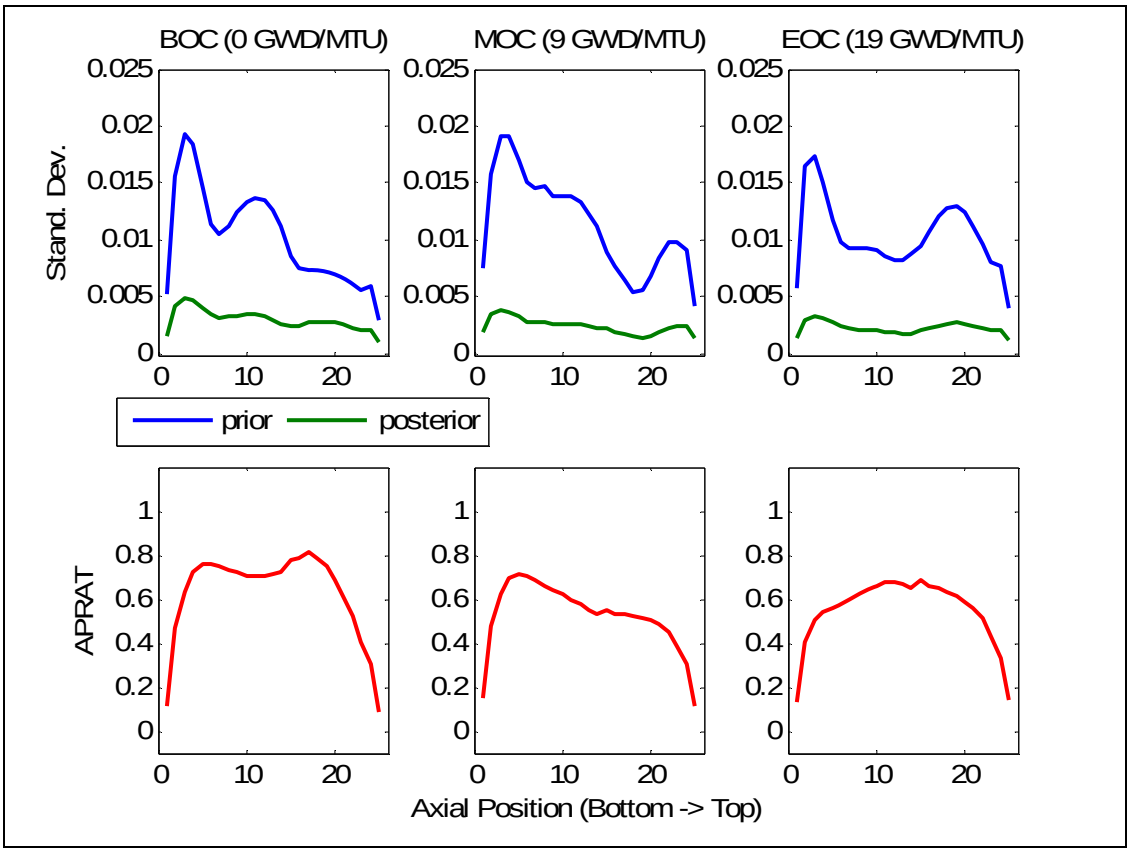


Figure 4-16 Prior and posterior absolute standard deviations in APRAT margin (Case B).

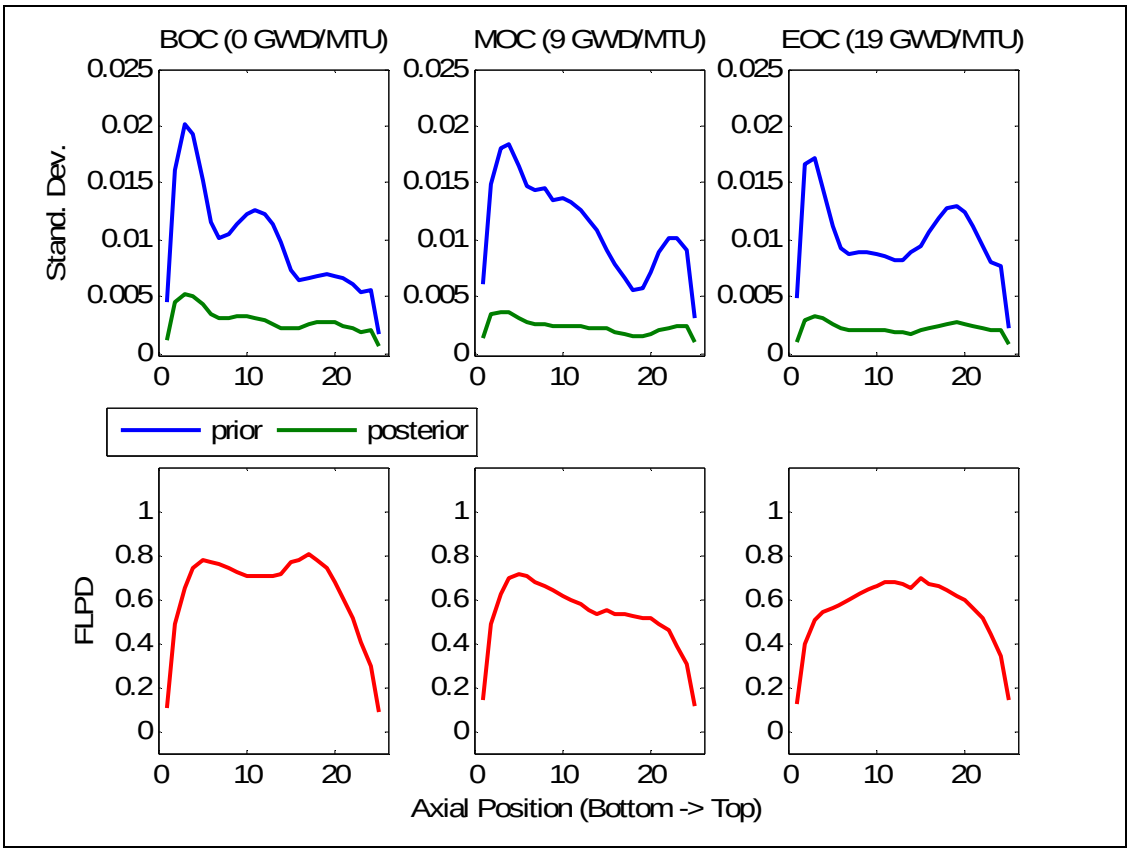


Figure 4-17 Prior and posterior absolute standard deviations in FLPD margin (Case B).

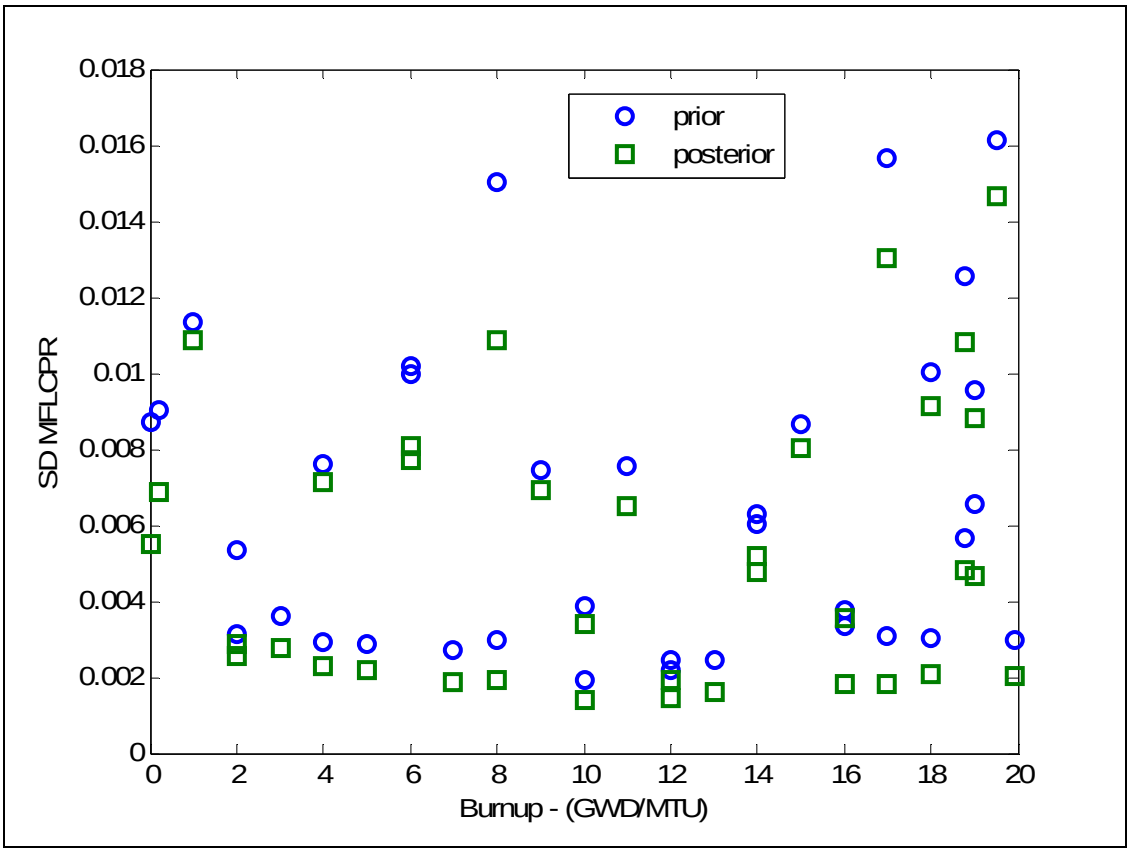


Figure 4-18 Prior and posterior absolute standard deviations in MFLCPR margin (Case B).

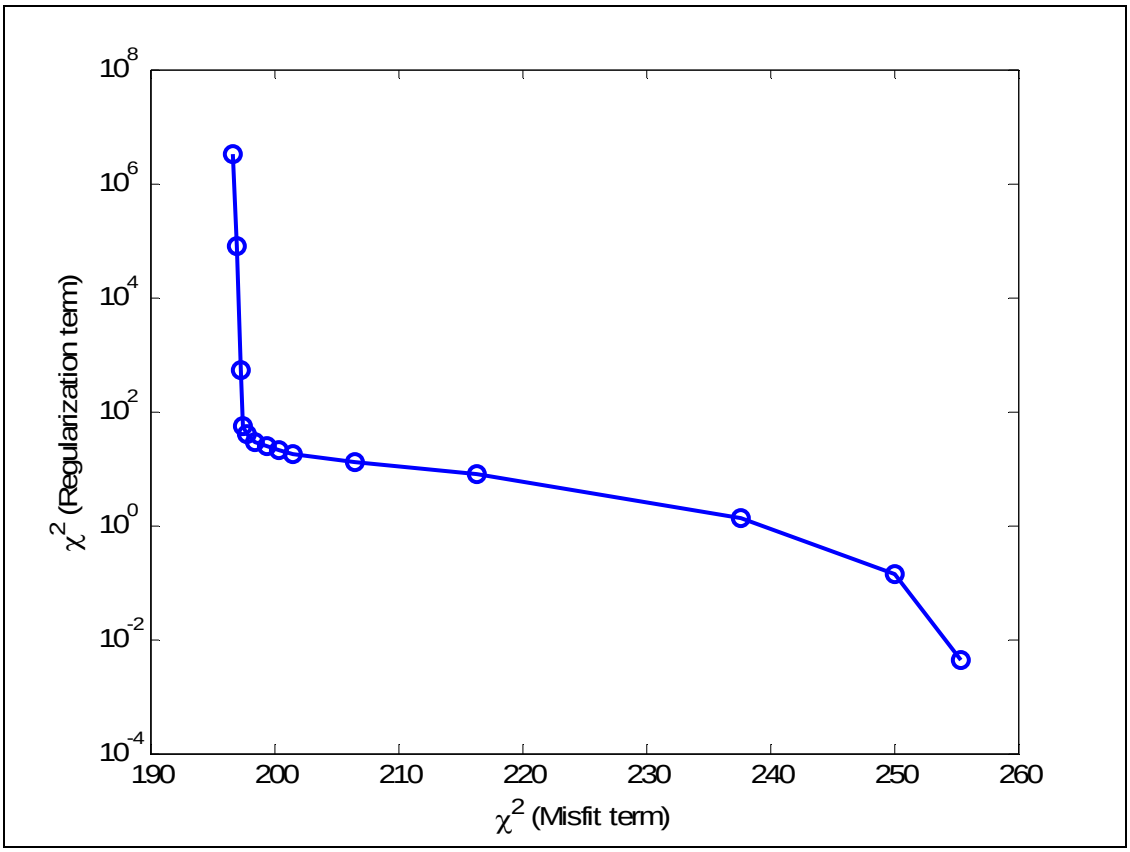


Figure 4-19 L-Curve of Cross-Section Adjustment (Case B).

# 5. Conclusions and Recommendations for Future Work

## 5.1. Conclusions

The goal of this work is to improve the fidelity of BWR computational models by developing the capability to adjust multi-group neutron cross-sections. BWR model predictions of LPRM detector response can disagree with measured LPRM detector readings with discrepancies larger than the noise level of the detector instrumentation. The magnitude of this error is comparable to the model prediction uncertainty due to multi-group cross-section uncertainty. This implies that BWR model fidelity can be enhanced by data adjustment techniques provided that they are computationally efficient, accurate, and robust. The previous work on BWR adaptive core simulation focused on the development of Efficient Subspace Methods (ESM) algorithms. These algorithms allow for fast, accurate, and robust plant adaption based on few-group cross-section adjustment. The use of the ESM algorithms to adjust multi-group cross-sections provides the additional capability to optimize lattice and fuel assembly designs for future fuel cycles.

In order to accurately quantify core observables uncertainty due to multi-group cross-section uncertainty, the multi-group cross-section covariance matrix must account for spatial and energy resonance self-shielding effects. Uncertainties in neutron cross-section resonance parameters impact the uncertainties in the infinitely-dilute multi-group cross-sections. They additionally impact the uncertainty in the resonance correction factors, or self-shielding factors, which correct the infinitely-dilute multi-group cross-sections for resonance and spatial self-shielding effects. The vast amount of resonance parameters and the computational

run-time limit the applicability of forward or adjoint sensitivity and uncertainty analysis techniques for resonance parameter uncertainty propagation. Moreover, the computational run-time needed for the NITAWL resonance treatment model limits the applicability of ESM-based techniques, where the singular value decomposition of the resonance parameter covariance matrix can be used to decrease the number of lattice physics calculations. Because of the multitudes of resonance parameter covariance data and the limiting run-times, a new resonance treatment model was developed for the TRITON lattice physics code. The new resonance treatment model uses an interpolation table of resonance correction factors to quickly and accurately evaluate the self-shielded multi-group cross-sections used in lattice physics calculation. Interpolation tables of resonance correction factors are commonplace among many of the nuclear industry's lattice physics codes. The functionalization of the interpolation tables with respect to fuel temperature and background scattering cross-sections varies among lattice physics codes, depending on the approximations employed in the resonance treatment model. For the TRITON lattice physics code, the NITAWL resonance treatment model is based on the Nordheim Integral Treatment method. In the modified resonance treatment model, the resonance correction factors are functionalized in terms of six system parameters that impact the Nordheim Integral Treatment calculation. Given this new interpolation table approach, the resonance parameter uncertainty analysis needs only to be performed one time for each mesh point in the interpolation table. Accounting for the uncertainty for each resonance correction factor in the interpolation table, the multi-group cross-section covariance matrix now includes the impact of the resonance parameters uncertainty during the resonance and spatial self-shielding calculation. Once the self-shielded

covariance matrix is calculated, ESM-based methods can be used to propagate multi-group cross-section uncertainty through the lattice physics calculation.

The uncertainties in key core attributes have been re-evaluated using the new formulation of the multi-group cross-section covariance matrix based on the ENDFB/6 cross-section covariance data. The uncertainty in k-effective is approximately 0.55% while the uncertainty in nodal power distributions and thermal margins is approximately 1.2%. The uncertainty propagation calculations were performed using Efficient Subspace Methods developed by Abdel-Khalik and Turinsky. Using ESM, approximately $10^4$ lattice physics calculations and $10^3$ core simulation calculations are required for uncertainty propagation based on the singular value decomposition of the self-shielded multi-group cross-section covariance matrix. The number of required calculations was decreased by an order of magnitude by using a GPT-based sensitivity analysis as a scoping tool to remove unnecessary calculations along singular vectors that do not significantly contribute to core attributes' uncertainties.

Numerical experiments were conducted to show the capabilities of the ESM-based multi-group cross-section adjustment algorithm for BWR Adaptive Core Simulation. These experiments reveal that the 4% noise in virtually simulated core observables does not degrade the fidelity and robustness of the cross-section adjustment beyond the scope of useful utility. These results are consistent with the few-group cross-section adjustments in the previous work on BWR ACS. In addition to the developed methods to adjust multi-group cross-sections, the evaluation of posterior covariance matrices within the ESM-based methodology has been rigorously formulated.

## 5.2. Recommendations for Future Work

The first and most important recommendation for future work regards the testing of the proposed cross-section adjustment techniques using real plant data as opposed to simulated plant data. Real plant data poses many challenges that the proposed adjustment techniques do not address. These include the quality of the measured data supplied by the plant and the treatment of systematic measurement errors, such as detector drift, in addition to the random measurement fluctuations that are currently treated.

The second area that needs further attention pertains to the resonance treatment model in TRITON. Resonance correction factors, or self-shielding factors, in the resolved resonance region are functionalized in terms of fuel temperature, Dancoff correction factor, number density of the resonance absorber, and other terms that depend on the potential scattering cross-sections of the isotopes in each fuel pin. Currently, TRITON calculates Dancoff correction factors by assuming an infinite repetitive lattice of identical fuel pins. For strong neighbor effects (e.g. - water holes, control rods, etc.), the Dancoff correction factor can change significantly. Methods to account for neighbor effects vary for many of the nuclear industry's standard lattice physics codes. Further investigation is necessary for implementation in the TRITON lattice physics code. Second, resonance interference effects are not considered in the interpolation table of resonance correction factors in the modified resonance self-shielding model. The CENTRM resonance processing module could be used in a series of benchmark calculations to determine the important resonance interference effects. From these benchmark calculations, the interpolation tables could be modified to

account for resonance interference. It is expected that both of these methods will minimally impact the uncertainty propagation and data adjustment calculations presented in this work.

The third improvement to this work pertains to accounting for the indirect uncertainty contribution due to the uncertainty in the Dancoff correction factor and the background scattering terms used in the resonance correction factor interpolation table. TRITON calculates the Dancoff correction factors using one-group total cross-sections from the standard composition library [52], and the background scattering terms from the potential scattering cross-sections of each isotope in the fuel pin. Accounting for this cross-section dependence, nonzero sensitivity coefficients now exist that reflect changes in self-shielded multi-group cross-sections across different isotopes. For example, a change in the hydrogen multi-group scattering cross-section induces a change in the Dancoff correction factor, which induces a change in the self-shielded multi-group cross-sections for U-238. The eigenvalue decomposition of the self-shielded multi-group cross-section covariance matrix will now have nonzero elements in the eigenvectors which correspond to these nonzero sensitivity coefficients. In addition, the one-group cross-sections on the standard composition library need to be consistently perturbed with the 44-group self-shielded multi-group cross-sections so that the burnup dependent few-group cross-section sensitivity coefficients will be correctly quantified. Since accounting for these effects increases the "denseness" of the self-shielded covariance matrix (i.e – no longer block diagonal), it may be more tractable to use the implicit sensitivity coefficients generated by automatic differentiation tools in the TSUNAMI code package. Automatic differentiation tools may be necessary if TRITON is modified to account for neighbor effects of the Dancoff correction factor.

The fourth improvement to this work pertains to regenerating the sensitivity coefficients of the self-shielded multi-group cross-sections with respect to Reich-Moore resonance parameters using the CENTRM resonance treatment model. CENTRM can calculate resonance correction factors for Reich-Moore cross-section resonance models while NITAWL can only treat Single-Level Breit Wigner (SLBW) or Multi-Level Breit Wigner cross-section resonance models. NITAWL was chosen over CENTRM for two reasons. First, sensitivity coefficients of self-shielded multi-group cross-sections with respect to SLBW resonance parameters could be directly computed by perturbing each resonance parameter one-at-a-time on the master cross-section library. CENTRM uses a different set of point-wise cross-section libraries where the Reich-Moore resonance parameters have been preprocessed into cross-section spectra with approximately ~70,000 energy groups. This preprocessor code was unavailable for this work to generate perturbed point-wise cross-section spectra for each Reich-Moore resonance parameter. Second, benchmark lattice physics calculations were computed using the 238-group cross-section library using both the NITAWL resonance treatment model and the CENTRM resonance treatment model. Comparisons of these calculations revealed similar k-infinity curves as a function of burnup with a k-infinity bias less than 100 pcm. Therefore, it was assumed that the sensitivity coefficients generated based on the NITAWL resonance treatment model would be as accurate as the CENTRM resonance treatment model.

The final recommendation of this work would be the implementation of first-order adjoint capability in the resonance treatment models and lattice physics model. This will allow for the use of the powerful ESM algorithms to calculate low-rank approximations of

each sensitivity matrix. For the resonance treatment model, this will allow for fast and accurate sensitivity coefficient evaluation of the thousands of Reich-Moore parameters used in Reich-Moore resonance treatment models. For the lattice physics model, time-dependent perturbation theory could be used to a) reduce the number of singular vectors of the self-shielded multi-group cross-section covariance matrix that must be evaluated in the lattice physics calculation, and b) evaluate the importance of fission product yield uncertainties to few-group cross-section uncertainty. Higher-order GPT methods could also be used to potentially minimize the number of forward perturbation calculations needed to build the multi-group cross-section interpolation table and the few-group cross-section interpolation table.

# REFERENCES

[1] H. S. Abdel-Khalik, "Adaptive Core Simulation," Ph.D. Dissertation, North Carolina State University (2004).

[2] H. S. Abdel-Khalik, "Inverse Method Applied to Adaptive Core Simulation," M.S. Thesis, North Carolina State University (2002).

[3] P. B. Heming, "Development of ENDF/B System." Proceedings of 3rd Conference on Neutron Cross Sections and Technology, USAEC CONF-71031 (1971).

[4] "ENDF-102 Data Formats and Procedures for the Evaluated Nuclear Data File ENDF-6," BNL-NCS-44945, Rev. 06/05 (ENDF/B-VI), Brookhaven National Laboratory (June 2005).

[5] N. M. Greene and M. E. Dunn, "AMPX-2000: A Modular Code System for Processing ENDF/B Evaluations," NUREG/CR-6659, ORNL/TM-1999/265, DRAFT (September 2001).

[6] R. E. MacFarlane and R. M. Boicourt, "NJOY: A Neutron and Photon Processing System," Transactions of American Nuclear Society, **22**, 720 (1975)

[7] A. N. Tikhonov, Numerical Methods for the Solution of Ill-Posed Problems, Kluwer Academic Publishers (1995).

[8] H. W. Engl and W. Grever, "Using the L-Curve for determining optimal regularization parameters," Numerische Mathematik, **69**, 25 (1994).

[9] M. A. Jessee, H. S. Abdel-Khalik, and P. J. Turinsky, "Evaluation of BWR Core Attributes Uncertainties Due to Multi-Group Cross-Section Uncertainties," Jnt. Intl. Conf. on Mathematics and Computation, and Supercomputing in Nuclear Applications, Monterey, CA (April 2007).

[10] C. M. Briggs, "Multicycle Adaptive Simulation of Boiling Water Reactor Core Simulators," M. S. Thesis, North Carolina State University (2007).

[11] M. Asgari, D. J. Kropaczek, J. J. Tusar, "N-Streaming$^{SM}$ Concept for Boiling Water Reactor Fuel Cycle Design," Transactions of the American Nuclear Society, **92**, 612 (2005).

[12] G. A. Watford, "GE 10x10 Advanced BWR Fuel Design," Advances in Nuclear Fuel Management II Topical Meeting, Myrtle Beach, SC (1997).

[13] Covariance Libraries provided with distribution of: "SCALE: A Modular Code System for Performing Standardized Computer Analyses for Licensing and Evaluation," NUREG/CR-0200, ORNL/NUREG/CSD-2/R6 Version 5.0 (2000).

[14] M. E. Dunn, "PUFF-III: A Code for Processing ENDF Uncertainty Data into Multigroup Covariance Matrices," NUREG/CR-6650, ORNL/TM-1999/235), U.S. Regulatory Commission, Oak Ridge National Laboratory (2006).

[15] D. G. Naberejnev and D. L. Smith, "A Method to Construct Covariance File in ENDF/B Format for Criticality Safety Applications," ANL/NDM-148, June 1999.

[16] M. D. DeHart, "TRITON: A Two Dimensional Depletion Sequence for Characterization of Spent Nuclear Fuel," ORNL/TM-2005/39, part of SCALE Version 5.1 (November 2006).

[17] F. Giust, D. Greiner, and C. Vidal, "BWR Core Monitoring Without LPRM Adaption," Forth ANS International Topical Meeting on Nuclear Plant Instrumentation, Controls and Human-Machine Interface Technologies, Columbus, Ohio (September 2004).

[18] C. M. Kang and R. L. Crowther, "Adaptive Method for Boiling Water Reactor Simulations," Transactions of the American Nuclear Society, **38**, 340 (1981).

[19] D. Delp *et al*. "FLARE: 3-D BWR Simulator," GEAP-4598, General Electric Company (1964).

[20] M. Tsuiki, H. Uematsu, and H. Koibuchi, "On-Line Predictive Calculation of a Boiling Water Reactor Core," Transactions of American Nuclear Society, **38**, 344 (1981).

[21] C. R. Weisbin, E. M. Oblow, J. H. Marable, R. W. Peelle, and J. L. Lucius, "Application of Sensitivity and Uncertainty Methodology to Fast Reactor Integral Experiment Analysis," Nuclear Science and Engineering, **66**, 307-333 (1978).

[22] J. H. Marable, C. R. Weisbin, and G. de Saussure, "Uncertainty in the Breeding Ratio of a Large Liquid-Metal Fast Breeder Reactor: Theory and Results," Nuclear Science and Engineering, **75**, 30 (1980).

[23] J. L. Lucius *et al*. "A Users Manual for the FORSS Sensitivity and Uncertainty Analysis Code System," ORNL/TM-5316 (1981).

[24] H. Mitani and H. Kuroi, "Adjustment of Group Cross Sections by Means of Integral Data, (II)," Journal of Nuclear Science and Technology, **9**(11), 642 (1972).

[25] R. W. Peele, "Uncertainty in the Nuclear Data Used for Reactor Core Calculations," Advances in Nuclear Science and Technology, **14** (1982).

[26] J. B. Dargt, J. W. M. Dekker, H. Gruppelaar, and A. J. Janssen, "Methods of Adjustment and Error Evaluation of Neutron Capture Cross Sections; Application to Fission Product Nuclides," Nuclear Science and Engineering, **62**, 117 (1977).

[27] P. J. Collins and M. J. Lineberry, "The Use of Cross Section Sensitivities in the Analysis of Fast Reactor Integral Parameters," Review of The Theory and Application of Sensitivity and Uncertainty Analysis, Proceedings of a Seminar Workshop, Oak Ridge, Tennessee, ORNL/RSIC-42 (1979).

[28] G. Aliberti, *et al.,* "Nuclear Data Sensitivity, Uncertainty and Target Accuracy Assessment for Future Nuclear Systems," Annals of Nuclear Energy, **33**, (2006).

[29] E. P. Wigner, "Effects of Small Perturbations on Pile Period," CP-3048, Manhattan Project Report (1945).

[30] L. N. Usachev, "Perturbation theory for the breeding ratio and for other number ratios pertaining to various reactor processes," Journal of Nuclear Energy, Parts A/B, **18**, 571 (1964).

[31] B. B. Kadmotzev, "On the importance function in radiative energy transport theory," Doklady Akademii Nauk SSSR, **113**(3) (1957).

[32] A. Gandini, "A generalized perturbation method for bilinear functionals of the real and adjoint neutron fluxes," Journal of Nuclear Energy, **21**, 755 (1967)

[33] G. Pomeraning, "Variation Principle for Eigenvalue Equations," Journal of Mathematical Physics, **8**, 149 (1967).

[34] W. Stacy, Variational Methods in Nuclear Reactor Physics, Academic Press, New York, 1974.

[35] M. L. Williams, "Development of depletion perturbation theory for coupled neutron/nuclide fields," Nuclear Science and Engineering, **70**, 20 (1979).

[36] D. G. Cacuci, Sensitivity and Uncertainty Analysis Theory, Volume 1, CRC Press (2000).

[37] T. Takeda, T. Sano, and T. Kitada, "Generalized Bias Factor Method for Accurate Prediction of Neutronics Characteristics," PHYSOR-2006-ANS Topical Meeting on Reactor Physics, Vancouver, BC, Canada (2006).

[38] Y. Ronen, D. G. Cacuci, and J. J. Wagschal, "Determination and application of generalized bias operators using an inverse perturbation approach," Nuclear Science and Engineering, **77**, 426 (1981).

[39] J. Utke, U. Naumann, *et al*., "OpenAD/F: A Modular, Open-Source Tool for Automatic Differentiation of Fortran Codes," ACM Transactions on Mathematical Software, (2008).

[40] J. E. Horwedel *et al*, "GRESS, A Preprocessor for Sensitivity Studies for Fortran Programs," Proceedings of SIAM Workshop of Automatic Differentiation of Algorithms: Theory, Implementation, and Application, Breckinridge, Colorado (1991).

[41] B. T. Rearden, "TSUNAMI-1D: Control Module for One-Dimensional Cross-Section Sensitivity and Uncertainty Analysis for Criticality," ORNL/TM-2005/39, part of SCALE Version 5.1 (November 2006).

[42] A. Tarantola, Inverse Problem Theory, Methods of Data Fitting and Model Parameter Estimation, Elsevier Science Publishers B. V. (1987).

[43] Y. Ronen, Uncertainty Analysis, CRC Press (1988).

[44] B. M. Ayyub and G. J. Klir, Uncertainty Modeling and Analysis in Engineering and the Sciences, Chapman & Hall/CRC Press (2006).

[45] D. Wiarda and M. E. Dunn, "PUFF-IV: A Code for Processing ENDF Uncertainty Data into Multigroup Covariance Matrices," Informal Report (2006).

[46] Z. Bai, J. Demmel, J. Dongarra, A. Ruhe, and H. van der Vorst, editors., Templates for the Solution of Algebraic Eigenvalue Problems: A Practical Guide, SIAM, Philadelphia (2000).

[47] B.R. Moore, P.J. Turinsky, and A. A. Karve, "FORMOSA-B: A Boiling Water Reactor In-core Fuel Management Optimization Package," Nuclear Technology, **126**, 153 (1999).

[48] B. L. Broadhead, "SCALE5.1 Cross-Section Covariance Libraries," ORNL/TM-2005/39, part of SCALE Version 5.1 (November 2006).

[49] N. M. Greene, L. M. Petrie, and R. M. Westfall, "NITAWL: SCALE System Module for Performing Resonance Shielding and Working Library Production," ORNL/TM-2005/39, part of SCALE Version 5.1 (November 2006).

[50] S. F. Mughabghab, Atlas of Resonance Parameters, Elsevier Publishers (2006).

[51] J. J. Duderstadt and L. J. Hamilton, Nuclear Reactor Analysis, John Wiley and Sons (1976).

[52] M. Edenius and B. H. "CASMO-3: A Fuel Assembly Burnup Program: User's Manual," STUDSVIK/NFA-89/3, Studsvik of America, Inc. (1991).

[53] L. M. Petrie, P. B. Fox, and K. Lucius, “Standard Composition Library,” ORNL/TM-2005/39, part of SCALE Version 5.1 (November 2006).

# APPENDIX

# APPENDIX A: DEVELOPMENT OF ESM DATA ADJUSTMENT SOLUTION

Repeating the main text, the well-posed data adjustment problem (Eq. (2.35)) is given as:

$$\begin{aligned}\tilde{\bar{x}}_{MG} = \min_{\bar{x}_{MG}}\{&[\bar{y}_{CO_m} - \bar{y}_{CO_0} - \bar{\bar{\mathbf{S}}}_{CS}\bar{\bar{\mathbf{S}}}_{LP}(\bar{x}_{MG} - \bar{x}_{MG_0})]^T \bar{\bar{\mathbf{C}}}^{\dagger}_{CO_m}[\bar{y}_{CO_m} - \bar{y}_{CO_0} - \bar{\bar{\mathbf{S}}}_{CS}\bar{\bar{\mathbf{S}}}_{LP}(\bar{x}_{MG} - \bar{x}_{MG_0})] + \\ &\alpha^2(\bar{x}_{MG} - \bar{x}_{MG_0})^T \bar{\bar{\mathbf{C}}}^{\dagger}_{MG}(\bar{x}_{MG} - \bar{x}_{MG_0})\} \\ &subject\ to\ \bar{x}_{MG} - \bar{x}_{MG_0} \in R(\bar{\bar{\mathbf{U}}}_{MG,t})\end{aligned} \tag{A.1}$$

where

| | |
|---|---|
| $\bar{x}_{MG_0}$ | prior self-shielded multi-group cross-sections |
| $\tilde{\bar{x}}_{MG}$ | posterior self-shielded multi-group cross-sections |
| $\bar{\bar{\mathbf{C}}}_{MG}$ | prior self-shielded multi-group cross-sections covariance matrix |
| $\bar{x}_{FG_0}$ | prior lattice-averaged few-group cross-sections |
| $\bar{y}_{CO_m}$ | prior core observables (i.e. - measured observables) |
| $\bar{\bar{\mathbf{C}}}_{CO_m}$ | prior core observables covariance matrix (i.e. - the uncertainty in the measurements of core observables). |
| $\bar{\bar{\mathbf{S}}}_{LP}$ | lattice physics sensitivity matrix |
| $\bar{\bar{\mathbf{S}}}_{CS}$ | core simulator sensitivity matrix |
| $\bar{\bar{\mathbf{U}}}_{MG,t}$ | singular vectors of the self-shielded multi-group cross-sections covariance matrix |
| $\bar{y}_{CO_0}$ | prior core observables as predicted by computational model |
| $n$ | dimension of $\bar{x}_{MG_0}$ (~$10^7$) |
| $m$ | dimension of $\bar{y}_{CO_m}$ (~$10^5$) |

$t$ rank of $\overline{\overline{\mathbf{C}}}_{MG}$ approximated by truncated-SVD

Using the compact SVD of $\overline{\overline{\mathbf{C}}}_{CO_m}$,

$$\begin{aligned}\overline{\overline{\mathbf{C}}}_{CO_m} &= \overline{\overline{\mathbf{U}}}_{CO_m}\overline{\overline{\mathbf{\Sigma}}}_{CO_m}\overline{\overline{\mathbf{U}}}^{T}_{CO_m}\\ \overline{\overline{\mathbf{C}}}^{\dagger}_{CO_m} &= \overline{\overline{\mathbf{U}}}_{CO_m}\overline{\overline{\mathbf{\Sigma}}}^{-1}_{CO_m}\overline{\overline{\mathbf{U}}}^{T}_{CO_m}\end{aligned} \tag{A.2}$$

Eq. (A.1) is rewritten in block matrix form as:

$$\bar{\tilde{x}}_{MG} = \min_{\bar{x}_{MG}}\{\left\| \begin{bmatrix} \overline{\overline{\mathbf{\Sigma}}}^{-1/2}_{CO_m}\overline{\overline{\mathbf{U}}}^{T}_{CO_m}(\bar{y}_{CO_m}-\bar{y}_{CO_0}) \\ 0 \end{bmatrix} - \begin{bmatrix} \overline{\overline{\mathbf{\Sigma}}}^{-1/2}_{CO_m}\overline{\overline{\mathbf{U}}}^{T}_{CO_m}\overline{\mathbf{S}}_{CS}\overline{\mathbf{S}}_{LP} \\ \alpha^2\overline{\overline{\mathbf{\Sigma}}}^{-1/2}_{MG,t}\overline{\overline{\mathbf{U}}}^{T}_{MG,t} \end{bmatrix}(\bar{x}_{MG}-\bar{x}_{MG_0}) \right\|_2^2\} \tag{A.3}$$

$$subject\ to\ \bar{x}_{MG}-\bar{x}_{MG_0} \in R(\overline{\overline{\mathbf{U}}}_{MG,t})$$

Because the self-shielded multi-group cross-section adjustment $\bar{x}_{MG}-\bar{x}_{MG_0}$ is constrained to $R(\overline{\overline{\mathbf{U}}}_{MG,t})$, the following change in variables is introduced:

$$\bar{z}_{MG}-\bar{z}_{MG_0} = \overline{\overline{\mathbf{\Sigma}}}^{-1/2}_{MG,t}\overline{\overline{\mathbf{U}}}^{T}_{MG,t}(\bar{x}_{MG}-\bar{x}_{MG_0}) \tag{A.4}$$

$$\bar{x}_{MG} = \bar{x}_{MG_0} + \overline{\overline{\mathbf{U}}}_{MG,t}\overline{\overline{\mathbf{\Sigma}}}^{1/2}_{MG,t}(\bar{z}_{MG}-\bar{z}_{MG_0}) \tag{A.5}$$

The vector $\bar{z}_{MG_0}$ denotes the prior data adjustment vector, which is always zero. The vector $\bar{z}_{MG_0}$ is only defined for the sake of the following derivation. Using this change in variables, Eq. (A.3) reduces to:

$$\bar{\tilde{z}}_{MG} = \min_{\bar{z}_{MG}} \{ \left\| \begin{bmatrix} \bar{\bar{\Sigma}}_{CO_m}^{-1/2} \bar{\bar{U}}_{CO_m}^{T} (\bar{y}_{CO_m} - \bar{y}_{CO_0}) \\ \alpha \bar{z}_{MG_0} \end{bmatrix} - \begin{bmatrix} \bar{\bar{\Sigma}}_{CO_m}^{-1/2} \bar{\bar{U}}_{CO_m}^{T} \bar{\bar{S}}_{CS} \bar{\bar{S}}_{LP} \\ \alpha \bar{\bar{I}} \end{bmatrix} \bar{z}_{MG} \right\|_2^2 \} \tag{A.6}$$

where $\bar{\tilde{z}}_{MG}$ is the posterior data adjustment vector.

From Section 2.2.3, the following matrices are defined characterizing the action of the sensitivity matrices $\bar{\bar{S}}_{CS}$ and $\bar{\bar{S}}_{LP}$ on the singular vectors of the self-shielded multi-group covariance matrix $\bar{\bar{U}}_{MG,t} \bar{\bar{\Sigma}}_{MG,t}^{1/2}$:

$$\bar{\bar{R}}_{LP,t} = \bar{\bar{S}}_{LP} \bar{\bar{U}}_{MG,t} \bar{\bar{\Sigma}}_{MG,t}^{1/2} \tag{A.7}$$

$$\bar{\bar{R}}_{LP,t} = \bar{\bar{U}}_{LP,t_2} \bar{\bar{\Sigma}}_{LP,t_2} \bar{\bar{\Psi}}_{LP,t_2}^{T} \tag{A.8}$$

$$\bar{\bar{R}}_{CS,t_2} = \bar{\bar{S}}_{CS} \bar{\bar{U}}_{LP,t_2} \bar{\bar{\Sigma}}_{LP,t_2} \tag{A.9}$$

Eqs. (A.7)-(A.9) simplify the matrix $\bar{\bar{\Sigma}}_{CO_m}^{-1/2} \bar{\bar{U}}_{CO_m}^{T} \bar{\bar{S}}_{CS} \bar{\bar{S}}_{LP} \bar{\bar{U}}_{MG,t} \bar{\bar{\Sigma}}_{MG}^{1/2}$ in Eq. (A.6) to the following:

$$
\begin{aligned}
\bar{\bar{\Sigma}}_{CO_m}^{-1/2}\bar{\bar{U}}_{CO_m}^{T}\bar{\bar{S}}_{CS}\bar{\bar{S}}_{LP}\bar{\bar{U}}_{MG,t}\bar{\bar{\Sigma}}_{MG}^{1/2} &= \bar{\bar{\Sigma}}_{CO_m}^{-1/2}\bar{\bar{U}}_{CO_m}^{T}\bar{\bar{S}}_{CS}(\bar{\bar{S}}_{LP}\bar{\bar{U}}_{MG,t}\bar{\bar{\Sigma}}_{MG}^{1/2}) \\
&= \bar{\bar{\Sigma}}_{CO_m}^{-1/2}\bar{\bar{U}}_{CO_m}^{T}\bar{\bar{S}}_{CS}\bar{\bar{R}}_{LP,t} \\
&= \bar{\bar{\Sigma}}_{CO_m}^{-1/2}\bar{\bar{U}}_{CO_m}^{T}\bar{\bar{S}}_{CS}(\bar{\bar{U}}_{LP,t_2}\bar{\bar{\Sigma}}_{LP,t_2}\bar{\bar{\Psi}}_{LP,t_2}^{T}) \\
&= \bar{\bar{\Sigma}}_{CO_m}^{-1/2}\bar{\bar{U}}_{CO_m}^{T}(\bar{\bar{S}}_{CS}\bar{\bar{U}}_{LP,t_2}\bar{\bar{\Sigma}}_{LP,t_2})\bar{\bar{\Psi}}_{LP,t_2}^{T} \\
&= \bar{\bar{\Sigma}}_{CO_m}^{-1/2}\bar{\bar{U}}_{CO_m}^{T}\bar{\bar{R}}_{CS,t_2}\bar{\bar{\Psi}}_{LP,t_2}^{T}
\end{aligned}
\tag{A.10}
$$

Introducing the thin SVD:

$$
\begin{aligned}
\bar{\bar{\Sigma}}_{CO_m}^{-1/2}\bar{\bar{U}}_{CO_m}^{T}\bar{\bar{R}}_{CS,t_2}\bar{\bar{\Psi}}_{LP,t_2}^{T} &= \bar{\bar{U}}\ \bar{\bar{\Sigma}}\ \bar{\bar{V}}^{T} \\
\bar{\bar{U}}\ &is\ n\times t \\
\bar{\bar{\Sigma}}\ &is\ t\times t \\
\bar{\bar{V}}^{T}\ &is\ t\times t
\end{aligned}
\tag{A.11}
$$

the normal equation solution to Eq. (A.6) is written as:

$$
\begin{aligned}
\begin{bmatrix}\bar{\bar{V}}\bar{\bar{\Sigma}}\bar{\bar{U}}^{T} & \alpha\bar{\bar{I}}\end{bmatrix}\begin{bmatrix}\bar{\bar{U}}\ \bar{\bar{\Sigma}}\ \bar{\bar{V}}^{T} \\ \alpha\bar{\bar{I}}\end{bmatrix}\bar{\tilde{z}}_{MG} &= \begin{bmatrix}\bar{\bar{V}}\bar{\bar{\Sigma}}\bar{\bar{U}}^{T} & \alpha\bar{\bar{I}}\end{bmatrix}\begin{bmatrix}\bar{\bar{\Sigma}}_{CO_m}^{-1/2}\bar{\bar{U}}_{CO_m}^{T}(\bar{y}_{CO_m}-\bar{y}_{CO_0}) \\ \alpha\bar{z}_{MG_0}\end{bmatrix} \\
(\bar{\bar{V}}\bar{\bar{\Sigma}}^{2}\bar{\bar{V}}^{T}+\alpha^2\bar{\bar{I}})\bar{\tilde{z}}_{MG} &= RHS \\
(\bar{\bar{V}}\bar{\bar{\Sigma}}^{2}\bar{\bar{V}}^{T}+\alpha^2\bar{\bar{V}}\bar{\bar{V}}^{T})\bar{\tilde{z}}_{MG} &= RHS \\
\bar{\bar{V}}(\bar{\bar{\Sigma}}^{2}+\alpha^2\bar{\bar{I}})\bar{\bar{V}}^{T}\bar{\tilde{z}}_{MG} &= RHS \\
\bar{\tilde{z}}_{MG} = \bar{\bar{V}}(\bar{\bar{\Sigma}}^{2}+\alpha^2\bar{\bar{I}})^{-1}\bar{\bar{V}}^{T}&\begin{bmatrix}\bar{\bar{V}}\bar{\bar{\Sigma}}\bar{\bar{U}}^{T} & \alpha\bar{\bar{I}}\end{bmatrix}\begin{bmatrix}\bar{\bar{\Sigma}}_{CO_m}^{-1/2}\bar{\bar{U}}_{CO_m}^{T}(\bar{y}_{CO_m}-\bar{y}_{CO_0}) \\ \alpha\bar{z}_{MG_0}\end{bmatrix} \\
\bar{\tilde{z}}_{MG} = \bar{\bar{V}}(\bar{\bar{\Sigma}}^{2}+\alpha^2\bar{\bar{I}})^{-1}\bar{\bar{V}}^{T}&\begin{bmatrix}\bar{\bar{V}}\bar{\bar{\Sigma}}\bar{\bar{U}}^{T} & \alpha\bar{\bar{I}}\end{bmatrix}\begin{bmatrix}\bar{\bar{\Sigma}}_{CO_m}^{-1/2}\bar{\bar{U}}_{CO_m}^{T} & 0 \\ 0 & \alpha\bar{\bar{I}}\end{bmatrix}\begin{bmatrix}\bar{y}_{CO_m}-\bar{y}_{CO_0} \\ \bar{z}_{MG_0}\end{bmatrix}
\end{aligned}
\tag{A.12}
$$

Substituting $\bar{z}_{MG_0} = \bar{0}$ into Eq. (A.12), the final expression for $\bar{\tilde{z}}_{MG}$ is given as:

$$\boxed{\begin{aligned}\bar{\tilde{z}}_{MG} &= \bar{\bar{\mathbf{V}}}(\bar{\bar{\mathbf{\Sigma}}}^2 + \alpha^2 \bar{\bar{\mathbf{I}}})^{-1} \bar{\bar{\mathbf{\Sigma}}} \bar{\bar{\mathbf{U}}}^T \bar{\bar{\mathbf{\Sigma}}}_{CO_m}^{-1/2} \bar{\bar{\mathbf{U}}}_{CO_m}^T (\bar{y}_{CO_m} - \bar{y}_{CO_0}) \\ \bar{\tilde{x}}_{MG} &= \bar{x}_{MG_0} + \bar{\bar{\mathbf{U}}}_{MG,t} \bar{\bar{\mathbf{\Sigma}}}_{MG,t}^{1/2} \bar{z}_{MG}\end{aligned}} \tag{A.13}$$

The posterior lattice-averaged few-group cross-sections (i.e. - $\bar{\tilde{x}}_{FG}$) and posterior core observables (i.e. - $\bar{\tilde{y}}_{CO}$) are determined by re-running the lattice physics model and core simulator model:

$$\boxed{\begin{aligned}\bar{\tilde{x}}_{FG} &= \mathbf{\Theta}_{LP}(\bar{\tilde{x}}_{MG}) \\ \bar{\tilde{y}}_{CO} &= \mathbf{\Theta}_{CS}(\mathbf{\Theta}_{LP}(\bar{\tilde{x}}_{MG}))\end{aligned}} \tag{A.14}$$

or by using the sensitivity matrices to determine a first-order approximation:

$$\begin{aligned}\bar{\tilde{x}}_{FG} &\cong \bar{x}_{FG_0} + \bar{\bar{\mathbf{\Theta}}}_{LP}(\bar{\tilde{x}}_{MG} - \bar{x}_{MG_0}) \\ \bar{\tilde{y}}_{CO} &\cong \bar{x}_{FG_0} + \bar{\bar{\mathbf{\Theta}}}_{CS} \bar{\bar{\mathbf{\Theta}}}_{LP}(\bar{\tilde{x}}_{MG} - \bar{x}_{MG_0})\end{aligned} \tag{A.15}$$

Substituting Eqs. (A.5), and (A.7)-(A.9) into Eq. (A.15), the first-order approximation simplifies to:

$$\begin{aligned}\bar{\bar{x}}_{FG} &\cong \bar{x}_{FG_0} + \bar{\bar{\Theta}}_{LP}(\bar{\bar{x}}_{MG} - \bar{x}_{MG_0}) \\ &= \bar{x}_{FG_0} + (\bar{\bar{\Theta}}_{LP}\bar{\bar{\mathbf{U}}}_{SS,t}\bar{\bar{\Sigma}}^{1/2}_{SS,t})(\bar{z}_{MG} - \bar{z}_{MG_0}) \\ &= \bar{x}_{FG_0} + \bar{\bar{\mathbf{R}}}_{LP,t}(\bar{z}_{SS} - \bar{z}_{MG_0}) \\ &= \bar{x}_{FG_0} + \bar{\bar{\mathbf{R}}}_{LP,t}\bar{z}_{MG}\end{aligned} \tag{A.16}$$

$$\begin{aligned}\bar{\tilde{y}}_{CO} &= \bar{x}_{FG_0} + \bar{\bar{\Theta}}_{CS}\bar{\bar{\Theta}}_{LP}(\bar{\bar{x}}_{MG} - \bar{x}_{MG_0}) \\ &= \bar{x}_{FG_0} + \bar{\bar{\Theta}}_{CS}\bar{\bar{\mathbf{R}}}_{LP,t}\bar{z}_{MG} \\ &= \bar{x}_{FG_0} + \bar{\bar{\Theta}}_{CS}(\bar{\bar{\mathbf{U}}}_{LP,t_2}\bar{\bar{\Sigma}}_{LP,t_2}\bar{\bar{\Psi}}^{T}_{LP,t_2})\bar{z}_{MG} \\ &= \bar{x}_{FG_0} + (\bar{\bar{\Theta}}_{CS}\bar{\bar{\mathbf{U}}}_{LP,t_2}\bar{\bar{\Sigma}}_{LP,t_2})\bar{\bar{\Psi}}^{T}_{LP,t_2}\bar{z}_{MG} \\ &= \bar{x}_{FG_0} + \bar{\bar{\mathbf{R}}}_{CS,t_2}\bar{\bar{\Psi}}^{T}_{LP,t_2}\bar{z}_{MG}\end{aligned} \tag{A.17}$$

The posterior data adjustment covariance matrix, denoted $\bar{\bar{\mathbf{C}}}_{\tilde{z}}$, is determined by the sandwich rule. Eq. (A.12) is rewritten as:

$$\bar{\tilde{z}}_{SS} = \begin{bmatrix}\bar{\bar{\mathbf{M}}}_{1,1} & \bar{\bar{\mathbf{M}}}_{1,2}\end{bmatrix}\begin{bmatrix}\bar{y}_{CO_m} - \bar{y}_{CO_0} \\ \bar{z}_{MG_0}\end{bmatrix} \tag{A.18}$$

where matrix $\bar{\bar{\mathbf{M}}}$ is defined as:

$$\bar{\bar{\mathbf{M}}} = \bar{\bar{\mathbf{V}}}(\bar{\bar{\Sigma}}^2 + \alpha^2\bar{\bar{\mathbf{I}}})^{-1}\bar{\bar{\mathbf{V}}}^T\begin{bmatrix}\bar{\bar{\mathbf{V}}}\bar{\bar{\Sigma}}\bar{\bar{\mathbf{U}}}^T & \alpha\bar{\bar{\mathbf{I}}}\end{bmatrix}\begin{bmatrix}\bar{\bar{\Sigma}}^{-1/2}_{CO_m}\bar{\bar{\mathbf{U}}}^T_{CO_m} & 0 \\ 0 & \alpha\bar{\bar{\mathbf{I}}}\end{bmatrix} \tag{A.19}$$

Using the uncertainty propagation method outlined in Section 2.2.1, $\overline{\overline{\mathbf{C}}}_{\tilde{z}}$ is given as:

$$\overline{\overline{\mathbf{C}}}_{\tilde{z}} = \begin{bmatrix} \overline{\overline{\mathbf{M}}}_{1,1} & \overline{\overline{\mathbf{M}}}_{1,2} \end{bmatrix} \begin{bmatrix} \overline{\overline{\mathbf{C}}}_{CO_m} & 0 \\ 0 & \overline{\overline{\mathbf{C}}}_{z} \end{bmatrix} \begin{bmatrix} \overline{\overline{\mathbf{M}}}_{1,1}^{T} \\ \overline{\overline{\mathbf{M}}}_{1,2}^{T} \end{bmatrix} \tag{A.20}$$

where the prior core observables covariance matrix $\overline{\overline{\mathbf{C}}}_{CO_m}$ and the prior data adjustment covariance matrix $\overline{\overline{\mathbf{C}}}_{z}$ are uncorrelated. The prior data adjustment covariance matrix $\overline{\overline{\mathbf{C}}}_{z}$ is the *t* by *t* identity matrix in order to satisfy:

$$\begin{aligned} \overline{z}_{MG} - \overline{z}_{MG_0} &= \overline{\overline{\mathbf{\Sigma}}}_{MG,t}^{-1/2} \overline{\overline{\mathbf{U}}}_{MG,t}^{T} (\overline{x}_{MG} - \overline{x}_{MG_0}) \Rightarrow \\ \overline{\overline{\mathbf{C}}}_{z} &= \overline{\overline{\mathbf{\Sigma}}}_{MG,t}^{-1/2} \overline{\overline{\mathbf{U}}}_{MG,t}^{T} \overline{\overline{\mathbf{C}}}_{MG,t} \overline{\overline{\mathbf{U}}}_{MG,t} \overline{\overline{\mathbf{\Sigma}}}_{MG,t}^{-1/2} \\ &= \overline{\overline{\mathbf{\Sigma}}}_{MG,t}^{-1/2} \overline{\overline{\mathbf{U}}}_{MG,t}^{T} (\overline{\overline{\mathbf{U}}}_{MG,t} \overline{\overline{\mathbf{\Sigma}}}_{MG,t} \overline{\overline{\mathbf{U}}}_{MG,t}^{T}) \overline{\overline{\mathbf{U}}}_{MG,t} \overline{\overline{\mathbf{\Sigma}}}_{MG,t}^{-1/2} \\ &= \overline{\overline{\mathbf{\Sigma}}}_{MG,t}^{-1/2} (\overline{\overline{\mathbf{U}}}_{MG,t}^{T} \overline{\overline{\mathbf{U}}}_{MG,t}) \overline{\overline{\mathbf{\Sigma}}}_{MG,t} (\overline{\overline{\mathbf{U}}}_{MG,t}^{T} \overline{\overline{\mathbf{U}}}_{MG,t}) \overline{\overline{\mathbf{\Sigma}}}_{MG,t}^{-1/2} \\ &= \overline{\overline{\mathbf{\Sigma}}}_{MG,t}^{-1/2} \overline{\overline{\mathbf{\Sigma}}}_{MG,t} \overline{\overline{\mathbf{\Sigma}}}_{MG,t}^{-1/2} \\ &= \overline{\overline{\mathbf{I}}} \end{aligned} \tag{A.21}$$

Substituting Eq. (A.19) and Eq. (A.21) into (A.20) produces the following expression for $\overline{\overline{\mathbf{C}}}_{\tilde{z}}$:

$$\begin{aligned}
\bar{\bar{\mathbf{C}}}_{\tilde{z}} &= \bar{\bar{\mathbf{V}}}(\bar{\bar{\boldsymbol{\Sigma}}}^2 + \alpha^2\bar{\bar{\mathbf{I}}})^{-1}\bar{\bar{\mathbf{V}}}^T\begin{bmatrix}\bar{\bar{\mathbf{V}}}\bar{\bar{\boldsymbol{\Sigma}}}\bar{\bar{\mathbf{U}}}^T & \alpha\bar{\bar{\mathbf{I}}}\end{bmatrix}\left\{\begin{bmatrix}\bar{\bar{\boldsymbol{\Sigma}}}_{CO_m}^{-1/2}\bar{\bar{\mathbf{U}}}_{CO_m}^T & 0\\ 0 & \alpha\bar{\bar{\mathbf{I}}}\end{bmatrix}\begin{bmatrix}\bar{\bar{\mathbf{C}}}_{CO_m} & 0\\ 0 & \bar{\bar{\mathbf{I}}}\end{bmatrix}\right.\\
&\left.\begin{bmatrix}\bar{\bar{\mathbf{U}}}_{CO,m}\bar{\bar{\boldsymbol{\Sigma}}}_{CO,m}^{-1/2} & 0\\ 0 & \alpha\bar{\bar{\mathbf{I}}}\end{bmatrix}\right\}\begin{bmatrix}\bar{\bar{\mathbf{U}}}\bar{\bar{\boldsymbol{\Sigma}}}\bar{\bar{\mathbf{V}}}^T\\ \alpha\bar{\bar{\mathbf{I}}}\end{bmatrix}\bar{\bar{\mathbf{V}}}(\bar{\bar{\boldsymbol{\Sigma}}}^2 + \alpha^2\bar{\bar{\mathbf{I}}})^{-1}\bar{\bar{\mathbf{V}}}^T\\
&= \bar{\bar{\mathbf{V}}}(\bar{\bar{\boldsymbol{\Sigma}}}^2 + \alpha^2\bar{\bar{\mathbf{I}}})^{-1}\bar{\bar{\mathbf{V}}}^T\begin{bmatrix}\bar{\bar{\mathbf{V}}}\bar{\bar{\boldsymbol{\Sigma}}}\bar{\bar{\mathbf{U}}}^T & \alpha\bar{\bar{\mathbf{I}}}\end{bmatrix}\begin{bmatrix}\bar{\bar{\boldsymbol{\Sigma}}}_{CO_m}^{-1/2}\bar{\bar{\mathbf{U}}}_{CO_m}^T\bar{\bar{\mathbf{C}}}_{CO_m}\bar{\bar{\mathbf{U}}}_{CO_m}\bar{\bar{\boldsymbol{\Sigma}}}_{CO_m}^{-1/2} & 0\\ 0 & \alpha^2\bar{\bar{\mathbf{I}}}\end{bmatrix}\\
&\begin{bmatrix}\bar{\bar{\mathbf{U}}}\bar{\bar{\boldsymbol{\Sigma}}}\bar{\bar{\mathbf{V}}}^T\\ \alpha\bar{\bar{\mathbf{I}}}\end{bmatrix}\bar{\bar{\mathbf{V}}}(\bar{\bar{\boldsymbol{\Sigma}}}^2 + \alpha^2\bar{\bar{\mathbf{I}}})^{-1}\bar{\bar{\mathbf{V}}}^T
\end{aligned} \tag{A.22}$$

$$\begin{aligned}
\Rightarrow \bar{\bar{\mathbf{C}}}_{\tilde{z}} &= \bar{\bar{\mathbf{V}}}(\bar{\bar{\boldsymbol{\Sigma}}}^2 + \alpha^2\bar{\bar{\mathbf{I}}})^{-1}\bar{\bar{\mathbf{V}}}^T\left\{\begin{bmatrix}\bar{\bar{\mathbf{V}}}\bar{\bar{\boldsymbol{\Sigma}}}\bar{\bar{\mathbf{U}}}^T & \alpha\bar{\bar{\mathbf{I}}}\end{bmatrix}\begin{bmatrix}\bar{\bar{\mathbf{I}}} & 0\\ 0 & \alpha^2\bar{\bar{\mathbf{I}}}\end{bmatrix}\begin{bmatrix}\bar{\bar{\mathbf{U}}}\bar{\bar{\boldsymbol{\Sigma}}}\bar{\bar{\mathbf{V}}}^T\\ \alpha\bar{\bar{\mathbf{I}}}\end{bmatrix}\right\}\bar{\bar{\mathbf{V}}}(\bar{\bar{\boldsymbol{\Sigma}}}^2 + \alpha^2\bar{\bar{\mathbf{I}}})^{-1}\bar{\bar{\mathbf{V}}}^T\\
&= \bar{\bar{\mathbf{V}}}(\bar{\bar{\boldsymbol{\Sigma}}}^2 + \alpha^2\bar{\bar{\mathbf{I}}})^{-1}\bar{\bar{\mathbf{V}}}^T\left\{\bar{\bar{\mathbf{V}}}\bar{\bar{\boldsymbol{\Sigma}}}\bar{\bar{\mathbf{U}}}^T\bar{\bar{\mathbf{U}}}\bar{\bar{\boldsymbol{\Sigma}}}\bar{\bar{\mathbf{V}}}^T + \alpha^4\bar{\bar{\mathbf{I}}}\right\}\bar{\bar{\mathbf{V}}}(\bar{\bar{\boldsymbol{\Sigma}}}^2 + \alpha^2\bar{\bar{\mathbf{I}}})^{-1}\bar{\bar{\mathbf{V}}}^T\\
&= \bar{\bar{\mathbf{V}}}(\bar{\bar{\boldsymbol{\Sigma}}}^2 + \alpha^2\bar{\bar{\mathbf{I}}})^{-1}\bar{\bar{\mathbf{V}}}^T\left\{\bar{\bar{\mathbf{V}}}\bar{\bar{\boldsymbol{\Sigma}}}^2\bar{\bar{\mathbf{V}}}^T + \alpha^4\bar{\bar{\mathbf{V}}}\bar{\bar{\mathbf{V}}}^T\right\}\bar{\bar{\mathbf{V}}}(\bar{\bar{\boldsymbol{\Sigma}}}^2 + \alpha^2\bar{\bar{\mathbf{I}}})^{-1}\bar{\bar{\mathbf{V}}}^T\\
&= \bar{\bar{\mathbf{V}}}(\bar{\bar{\boldsymbol{\Sigma}}}^2 + \alpha^2\bar{\bar{\mathbf{I}}})^{-1}(\bar{\bar{\mathbf{V}}}^T\bar{\bar{\mathbf{V}}})(\bar{\bar{\boldsymbol{\Sigma}}}^2 + \alpha^4\bar{\bar{\mathbf{I}}})(\bar{\bar{\mathbf{V}}}^T\bar{\bar{\mathbf{V}}})(\bar{\bar{\boldsymbol{\Sigma}}}^2 + \alpha^2\bar{\bar{\mathbf{I}}})^{-1}\bar{\bar{\mathbf{V}}}^T\\
&= \bar{\bar{\mathbf{V}}}(\bar{\bar{\boldsymbol{\Sigma}}}^2 + \alpha^2\bar{\bar{\mathbf{I}}})^{-1}(\bar{\bar{\boldsymbol{\Sigma}}}^2 + \alpha^4\bar{\bar{\mathbf{I}}})(\bar{\bar{\boldsymbol{\Sigma}}}^2 + \alpha^2\bar{\bar{\mathbf{I}}})^{-1}\bar{\bar{\mathbf{V}}}^T\\
&= \bar{\bar{\mathbf{V}}}(\bar{\bar{\boldsymbol{\Sigma}}}^2 + \alpha^2\bar{\bar{\mathbf{I}}})^{-2}(\bar{\bar{\boldsymbol{\Sigma}}}^2 + \alpha^4\bar{\bar{\mathbf{I}}})\bar{\bar{\mathbf{V}}}^T\\
&= \bar{\bar{\mathbf{V}}}\bar{\bar{\boldsymbol{\Sigma}}}_{\tilde{z}}\bar{\bar{\mathbf{V}}}^T
\end{aligned} \tag{A.23}$$

In Eq. (A.23), the singular values of $\bar{\bar{\mathbf{C}}}_{\tilde{z}}$ are defined as:

$$\bar{\bar{\boldsymbol{\Sigma}}}_{\tilde{z}_{i,i}} = \frac{\bar{\bar{\boldsymbol{\Sigma}}}_{i,i}^2 + \alpha^4}{(\bar{\bar{\boldsymbol{\Sigma}}}_{i,i}^2 + \alpha^2)^2} \tag{A.24}$$

As the Tikhonov regularization parameter approaches infinity, the singular values of $\overline{\overline{\mathbf{C}}}_{\tilde{z}}$ approach one, and the posterior data adjustment covariance matrix` equals the identity matrix (i.e. – prior data adjustment covariance matrix). In this case, the self-shielded multi-group cross-sections are not adjusted. Using Eq. (A.5), the posterior self-shielded multi-group cross-section covariance matrix $\overline{\overline{\mathbf{C}}}_{MG,post}$ is given as:

$$\begin{aligned}\overline{\overline{\mathbf{C}}}_{MG,post} &= \overline{\overline{\mathbf{U}}}_{MG,t}\,\overline{\overline{\mathbf{\Sigma}}}^{1/2}_{MG,t}\,\overline{\overline{\mathbf{C}}}_{\tilde{z}}\,\overline{\overline{\mathbf{\Sigma}}}^{1/2}_{MG,t}\,\overline{\overline{\mathbf{U}}}^{T}_{MG,t} \\ &= \overline{\overline{\mathbf{U}}}_{MG,t}\,\overline{\overline{\mathbf{\Sigma}}}^{1/2}_{MG,t}\,\overline{\overline{\mathbf{V}}}\,(\overline{\overline{\mathbf{\Sigma}}}^{2} + \alpha^{2}\overline{\mathbf{I}})^{-2}(\overline{\overline{\mathbf{\Sigma}}}^{2} + \alpha^{4}\overline{\mathbf{I}})\overline{\overline{\mathbf{V}}}^{T}\,\overline{\overline{\mathbf{\Sigma}}}^{1/2}_{MG,t}\,\overline{\overline{\mathbf{U}}}^{T}_{MG,t}\end{aligned} \tag{A.25}$$

The posterior lattice-averaged few-group cross-section covariance matrix $\overline{\overline{\mathbf{C}}}_{FG,post}$ and posterior core observables covariance matrix $\overline{\overline{\mathbf{C}}}_{CO,post}$ are given as:

$$\begin{aligned}\overline{\overline{\mathbf{C}}}_{FG,post} &= \overline{\overline{\mathbf{S}}}_{LP,post}\,\overline{\overline{\mathbf{C}}}_{MG,post}\,\overline{\overline{\mathbf{S}}}^{T}_{LP,post} \\ \overline{\overline{\mathbf{C}}}_{CO,post} &= \overline{\overline{\mathbf{S}}}_{CS,post}\,\overline{\overline{\mathbf{S}}}_{LP,post}\,\overline{\overline{\mathbf{C}}}_{MG,post}\,\overline{\overline{\mathbf{S}}}^{T}_{LP,post}\,\overline{\overline{\mathbf{S}}}^{T}_{CS,post}\end{aligned} \tag{A.26}$$

where the posterior sensitivity matrices (i.e. - $\overline{\overline{\mathbf{S}}}_{CS,post}$ and $\overline{\overline{\mathbf{S}}}_{LP,post}$) are evaluated at the posterior cross-section values. Assuming that the posterior sensitivity matrices are approximately the prior sensitivity matrices, Eq. (A.26) simplifies to the following:

$$
\begin{aligned}
\overline{\overline{\mathbf{C}}}_{FG,post} &\cong \overline{\overline{\mathbf{S}}}_{LP}\,\overline{\overline{\mathbf{C}}}_{MG,post}\,\overline{\overline{\mathbf{S}}}_{LP}^{T} \\
&= (\overline{\overline{\mathbf{S}}}_{LP}\,\overline{\overline{\mathbf{U}}}_{MG,t}\,\overline{\overline{\boldsymbol{\Sigma}}}_{MG,t}^{1/2})\,\overline{\overline{\mathbf{V}}}\,(\overline{\overline{\boldsymbol{\Sigma}}}^{2} + \alpha^{2}\overline{\overline{\mathbf{I}}})^{-2}(\overline{\overline{\boldsymbol{\Sigma}}}^{2} + \alpha^{4}\overline{\overline{\mathbf{I}}})\,\overline{\overline{\mathbf{V}}}^{T}\,(\overline{\overline{\boldsymbol{\Sigma}}}_{MG,t}^{1/2}\,\overline{\overline{\mathbf{U}}}_{MG,t}^{T}\,\overline{\overline{\mathbf{S}}}_{LP}^{T}) \\
&= \overline{\overline{\mathbf{R}}}_{LP,t}\,\overline{\overline{\mathbf{V}}}\,(\overline{\overline{\boldsymbol{\Sigma}}}^{2} + \alpha^{2}\overline{\overline{\mathbf{I}}})^{-2}(\overline{\overline{\boldsymbol{\Sigma}}}^{2} + \alpha^{4}\overline{\overline{\mathbf{I}}})\,\overline{\overline{\mathbf{V}}}^{T}\,\overline{\overline{\mathbf{R}}}_{LP,t}^{T} \\
\overline{\overline{\mathbf{C}}}_{CO,post} &\cong \overline{\overline{\mathbf{S}}}_{CS}\,\overline{\overline{\mathbf{S}}}_{LP}\,\overline{\overline{\mathbf{C}}}_{MG,post}\,\overline{\overline{\mathbf{S}}}_{LP}^{T}\,\overline{\overline{\mathbf{S}}}_{CS}^{T} \\
&= (\overline{\overline{\mathbf{S}}}_{CS}\,\overline{\overline{\mathbf{S}}}_{LP}\,\overline{\overline{\mathbf{U}}}_{MG,t}\,\overline{\overline{\boldsymbol{\Sigma}}}_{MG,t}^{1/2})\,\overline{\overline{\mathbf{V}}}\,(\overline{\overline{\boldsymbol{\Sigma}}}^{2} + \alpha^{2}\overline{\overline{\mathbf{I}}})^{-2}(\overline{\overline{\boldsymbol{\Sigma}}}^{2} + \alpha^{4}\overline{\overline{\mathbf{I}}})\,\overline{\overline{\mathbf{V}}}^{T}\,(\overline{\overline{\boldsymbol{\Sigma}}}_{MG,t}^{1/2}\,\overline{\overline{\mathbf{U}}}_{MG,t}^{T}\,\overline{\overline{\mathbf{S}}}_{LP}^{T}\,\overline{\overline{\mathbf{S}}}_{CS}^{T}) \\
&= \overline{\overline{\mathbf{R}}}_{CS,t_2}\,\overline{\overline{\boldsymbol{\Psi}}}_{LP,t_2}^{T}\,\overline{\overline{\mathbf{V}}}\,(\overline{\overline{\boldsymbol{\Sigma}}}^{2} + \alpha^{2}\overline{\overline{\mathbf{I}}})^{-2}(\overline{\overline{\boldsymbol{\Sigma}}}^{2} + \alpha^{4}\overline{\overline{\mathbf{I}}})\,\overline{\overline{\mathbf{V}}}^{T}\,\overline{\overline{\boldsymbol{\Psi}}}_{LP,t_2}\,\overline{\overline{\mathbf{R}}}_{CS,t_2}^{T}
\end{aligned}
\tag{A.27}
$$